CRANFIELD UNIVERSITY

Weixiang Du

The Design and Development of the Miniaturised Active Thermography for *In-situ* Inspection of Industrial Components

School of Aerospace, Transport and Manufacturing
PhD in Manufacturing

PhD Degree
Academic Year: 2017 - 2021

Primary Supervisor: Dr. Yifan Zhao
Associate Supervisor: Dr. Pavan Addepalli
June 2021

CRANFIELD UNIVERSITY

School of Aerospace, Transport and Manufacturing
PhD in Manufacturing

PhD Degree

Academic Year 2017 - 2021

Weixiang Du

The Design and Development of the Miniaturised Active Thermography for *In-situ* Inspection of Industrial Components

Primary Supervisor: Dr. Yifan Zhao
Associate Supervisor: Dr. Pavan Addepalli
June 2021

This thesis is submitted in partial fulfilment of the requirements for the degree of PhD
(NB. This section can be removed if the award of the degree is based solely on examination of the thesis)

ABSTRACT

Nondestructive testing (NDT) is a common and reliable method for the detection of surface and subsurface defects. However, due to the increasing integration and complexity of industrial components and systems, the problem of mismatching of size and volume between the existing inspection unit and the targeted object has limited the applicability of NDT techniques. Especially for geometrically intricate systems, the deployment of NDT devices for *in-situ* inspection has become a major challenge. Addressing the challenge of inaccessibility and inapplicability, this research proposes a miniaturised active thermography (MAT) system, featured with a small-size and low-cost thermal sensor, and a portable optical heat excitation source. A novel spatial resolution enhancement for a thermogram (SRE4T) system, which includes an infrared (IR) sensor, an XY movement stage and a super-resolution image enhancement method, is also proposed to address the low spatial resolution of the miniaturised sensor without upgrading the sensor. Moreover, dedicated data analysis approaches to evaluate defects are proposed considering the degraded signal quality. Compared with existing non-miniaturised inspection systems, the proposed system is evaluated quantitatively and qualitatively by testing samples with different materials, structures, and a variety of defects. An accessibility test is designed and conducted to evaluate the proposed system's performance to access geometrically intricate space.

The results show that the proposed system can work effectively for the degradation assessment of composite laminates, and also has enhanced accessibility and applicability of deployment for geometrically intricate systems and narrow space targets. It is observed that the data quality for composite materials seems to be more reliable and quantifiable than metal due to the relatively low sample rate of the sensor and the high thermal conductivity of the metal component. The SRE4T system can significantly improve the spatial resolution of miniaturised sensors, although it has not been used for active thermography at the present stage. The current miniaturised IR cameras feature low spatial resolution and low Signal-to-Noise Ratio, which leads to the poor

performance of most of the current data analysis methods on these sensors. We propose an effective analytics framework including data processing, image processing and feature extraction to reduce the influence of noise and enhance the detectability of damage.

Keywords:

In-situ, in-accessible, miniaturised, active thermography, industrial components, imaging enhancement

ACKNOWLEDGEMENTS

During my PhD study, I am deeply grateful to my first supervisor Dr. Yifan Zhao and my second supervisor Dr. Pavan Addepalli for their assistance at every stage of my research project. They gave me invaluable advice, insightful comments and significant help for my work. Their immense knowledge and plentiful experience have encouraged me in all the time of my academic research and daily life. I would also like to thank our ex-director of Manufacturing Professor Raj Roy, who gave me many directions and help at the beginning of my research project. Meanwhile, I would like to thank our director of TES Professor Andrew Starr for his unwavering support and belief in me. I would like to extend my sincere thanks to Dr. Barmak Honarvar Shakibaei Asli, Dr. Adisorn Sirikham, Dr. Haochen Liu and Dr. Lawrence Tinsley for their treasured support which was really influential in shaping my experiment methods and critiquing my results. I would like to thank Samuel Court and Professor John Ahmet Erkoyuncu for the perfect support for our hardware facilities, office environment and the academic atmosphere of our centre. I also would like to thank my classmates Dr. Lichao Yang, Dr. Youdao Wang, Dr. Xiaocai Shan, Dr. Jun Cao and Dr. Kailun Deng, you accompany me through the most beautiful campus time, also let me harvest valuable friendship. I also appreciate the support that I received from my parents, my wife and my little son Leo. Without their support, I cannot had so much wonderful time in Britain.

TABLE OF CONTENTS

LIST OF FIGURES

LIST OF TABLES

LIST OF EQUATIONS

LIST OF ABBREVIATIONS

APST	Absolute Peak Slope Time
APTC	Adaptive Peak Temperature Contrast
BVID	Barely Visible Impact Damage
CFRP	Carbon Fibre Reinforced Polymer
CT	Computerised Tomography
DPT	Dye Penetrant Testing
ECT	Eddy Current Testing
ECPT	Eddy Current Pulsed Thermography
ECLT	Eddy Current Lock-in Thermography
EM	Electromagnetic
ET	Entropy
FMC	Full Matrix Capture
GE	General Electric Company
GFRP	Glass Fibre Reinforced Polymer
HR	High Resolution
IR	Infrared
LR	Low Resolution
LSD	Logarithmic Second Derivative
LSF	Least-Squares Fitting
LT	Lock-in Thermography
LWIR	Long-Wavelength Infrared
MAT	Miniaturised Active Thermography
MPI	Magnetic Particle Inspection
MWIR	Mid-Wavelength Infrared
NC	Normalised Convolution
NDT	Non-Destructive Testing
NETD	Noise Equivalent Temperature Difference
NIQE	Natural Image Quality Evaluator
NLSF	New Least-Squares Fitting
NSI	Nonlinear System Identification
PCA	Principal Component Analysis
PCB	Printed Circuit Board

PSNR	Peak Signal to Noise Ratio
PST	Peak Slope Time
PT	Pulsed Thermography
PTC	Peak Temperature Contrast
ROI	Region of Interest
RT	Radiographic Testing
SANC	Structure-Adaptive Normalised Convolution
SHM	Structure Health Monitoring
SNR	Signal-to-Noise Ratio
SR	Super-Resolution
SRE4T	Spatial Resolution Enhancement for a Thermogram
SSIM	Structural Similarity
TC	Temperature Contrast
TOFD	Time of Flight Diffraction
TSR	Thermal Signal Reconstruction
UAV	Unmanned Aerial Vehicle
UT	Ultrasonic Testing
VT	Vibro-Thermography

LIST OF PUBLICATION

Journal Paper

1. **W. Du**, S. Addepalli, and Y. Zhao, “The Spatial Resolution Enhancement for a Thermogram Enabled by Controlled Sub-pixel Movements,” *IEEE Trans. Instrum. Meas.*, vol. 69, no. 6, pp. 3566-3575, Jun. 2020
2. **W. Du**, H. Liu, Y. Zhao, A. Sirikham, S. Addepalli, and Y. Zhao, “A Miniaturized Active Thermography System to Inspect Composite Laminates,” *IEEE Trans. Ind. Informatics*, vol. 17, no. 5, pp. 3314–3323, 2021
3. A. Sirikham, Y. Zhao, H. Y. Nezhad, **W. Du**, and R. Roy, “Estimation of Damage Thickness in Fiber-Reinforced Composites using Pulsed Thermography,” *IEEE Trans. Ind. Informatics*, vol. 15, no. 1, pp. 445–453, 2019
4. H. Liu, **W. Du**, H. Yazdani Nezhad, A. Starr, and Y. Zhao, “A Dissection and Enhancement Technique for Combined Damage Characterisation in Composite Laminates using Laser-line Scanning Thermography,” *Compos. Struct.*, vol. 271, no. February, p. 114168, Sep. 2021
5. J. Zhou, **W. Du,** Y. Zhao, “Pattern Recognition of Barely Visible Impact Damage in Carbon Composites using Pulsed Thermography”. *IEEE Trans. Ind. Informatics.* (under review)

Conference Paper

1. **W. Du**, Y. Zhao, R. Roy, S. Addepalli, and L. Tinsley, “A review of miniaturised Non-Destructive Testing technologies for in-situ inspections,” *Procedia Manuf.*, vol. 16, pp. 16–23, 2018
   (7th International Conference on Through-life Engineering Services, Cranfield University)
2. **W. Du**, Y. Zhao, and S. Addepalli, “Spatial Resolution Improvement of Digital and Thermographic Imaging Using an Automatic and Controllable Super-resolution Technique,” in *Structural Health Monitoring 2019*, vol. 1, pp. 1311–1318, 2019

(12th International Workshop on Structural Health Monitoring 2019, Stanford University)

3. **W. Du**, H. Liu, A. Sirikham, S. Addepalli, and Y. Zhao, “A miniaturised active thermography system for in-situ inspections,” IFAC-PapersOnLine, vol. 53, no. 3, pp. 66–71, 2020
   (4th IFAC Workshop on Advanced Maintenance Engineering, Services and Technologies 2020, University of Cambridge)

1 INTRODUCTION

1.1 Research Background

'*In-situ*' is a term that is widely used to define the location of sensors as part of the system with the capability to provide functional measurements when the asset is in its natural working environment [1]. Non-destructive testing (NDT) techniques such as ultrasonic testing, x-radiography inspection, eddy current testing and infrared thermography have become an indispensable part of product manufacturing, installation, and maintenance, due to their ability to detect defects and damage non-destructively without causing further damage to the part being inspected [2]. Additionally, their characteristics such as convenience, high efficiency and low cost make them more attractive for the industry to determine the health of the component. However, with the rapid increase of the functionalisation, integration, complexity of industrial products and increasing use of advanced materials into complex systems, the inaccessibility and inapplicability of existing NDT devices have become a bottleneck for *in-situ* inspection of these objects. The deployment of NDT devices in *in-situ* inspection has become a major challenge because of the factors such as heavy weight and the large size of the inspection unit and the complex structure of the targeted objects. It is particularly problematic for the challenging environments, such as systems with geometrically intricate space (e.g. aero-engines [3]), hazardous conditions (e.g. nuclear power generation [4]) in some safety-critical industrial sectors, high-altitude and difficult-to-climb targets (e.g. wind turbine blades [5]), highly constrained and semi-closed environment (e.g. aircraft wing box [6]), where it is frequently impossible to use "off-the-shelf" equipment for *in-situ* testing. Additionally, the serviceability of the components or systems to be inspected has now become a huge challenge, particularly in determining their maintenance requirements as disassembly and inspection can be very time-consuming and expensive. Therefore, the development of lightweight and miniaturised NDT systems is more and more important to inspect multiple materials for degradation assessment of inaccessible areas.

This research focuses on developing a miniaturised active thermography (MAT) system for '*in-situ*' inspection of complex industrial components, that has characteristics such as low-cost, flexible and configurable parameters. The combination of a lightweight/size Infrared (IR) camera with a built-in Lepton sensor and a pulse/laser excitation source system can reduce the cost and weight considerably. However, the detectability of this system will be limited by the low spatial resolution and low signal-to-noise ratio (SNR) of the sensor. Therefore, a novel Spatial Resolution Enhancement for a Thermogram (SRE4T) system is proposed to improve the thermal imaging quality without upgrading the sensor. With such a portable system, defects or damage in components within a complex structure become detectable. Furthermore, it will further facilitate the '*in-situ*' inspection without disassembling the integrated systems which could be costly. It is our profound aspiration that such a system will enhance and equip inspectors with smaller, less bulky systems when they go out for in-field inspections of safety-critical infrastructures, such as pipelines, wind turbine blades etc. It therefore will make a significant economic and social impact.

1.2 Research Motivation

Among the various NDT techniques, visual and optical testing have the characteristics of being intuitive, non-contact and robust. Industrial endoscopes armed with mini fibre optic probes [7] can extend the inspector's sight distance and have the ability to inspect hard-to-reach or inaccessible areas, but they are limited to detect small surface defects and cannot be used for sub-surface inspection. Options such as the Miniature Fiberscope [8], which is a representative endoscope produced by Karl Storz featuring a very small diameter of between 0.35mm and 1.3mm, do exist in the market. Alternate techniques, such as magnetic particle inspection [9], are suitable for the inspection of ferromagnetic materials, but the lift force of the yoke and defect detection rate will be reduced when the volume of the device decreases. The permanent magnet can be made small enough to fit into tight areas, but the lift force is difficult to control. For instance, the RPNSS and RPNSL permanent magnets equipment manufactured by Johnson & Allen Company are relatively small, but the lifting

force is limited to 18kg [10]. Radiographic testing can achieve accurate inspection for sub-surface defects using bulky computerised tomography (CT), such as Versatile Industrial CT Scanner [11]. Although there is evidence that a combination of X-ray machine and film can be used for *in-situ* inspection [12], including the upgraded equipment like DXR250C-W Wireless Digital X-ray Detector produced by GE [13], miniaturisation of radiographic inspection is still a challenge due to the influence of radioactivity and its strict personnel health requirements on the detection environment. Portable and pocket-type ultrasonic testing equipment [14] has become more and more popular. A typical example is the ISONIC utPod produced by Sonotron NDT, which is an ultra-portable, multi-purpose ultrasonic testing instrument and weighs at 400g [15]. However, the mandatory requirement of a coupling agent and the blind regions on the surface, limit its application for thin and complex-shaped workpieces with additional issues coming from cramped and inaccessible spaces [16]. Responding to the increasing demand for miniaturisation, the above features limit the progress and applications of corresponding NDT techniques in the context of *in-situ* inspection.

As a powerful NDT technique, infrared thermography can provide rapid, non-contact, and robust non-invasive detection of both surface and sub-surface defects/damage. However, at present, the existing miniaturised infrared cameras are mostly used in passive thermography, with a few studies investigating its application in active thermographic inspection [17][18][19]. Fuente *et al.* [20] used the reflection of the mirror to integrate the IR camera and laser into the borescope for pipe inspection. Du *et al.* [21] used the super-resolution method to improve the thermal image quality of low-resolution IR cameras. Even for these studies, the volume of integrated equipment available for industrial inspection is still relatively large.

According to the abovementioned reasons, the motivations of this thesis are:

- To improve the accessibility and applicability of the NDT technique for complex object inspection, especially for geometrically intricate systems, such as aero-engine and wing boxes.

- To improve the detection precision through developing the proprietary algorithms, especially for the low-end sensor with a low SNR.
- To save the time and cost of inspection (such as target object disassembly and assembly)

It is expected that a wide range of inspectors and industries can benefit from the outcomes of this research.

1.3 Research Aim and Objectives

The overall scientific aim of this research is to develop a miniaturised active thermography (MAT) system that features low-cost, flexible and configurable characteristics, for '*in-situ*' inspection of industrial components.

The aim of this thesis is achieved through meeting the following objectives:

Objective 1. To search the state-of-the-art miniaturised NDT techniques that are currently available for *in-situ* inspection and identify their main challenges and applications

Objective 2. To design and integrate a miniaturised active thermography system using off-the-shelf sensors and excitation sources for '*in-situ*' application

Objective 3. To collect the data using the miniaturised system and develop approaches to improve the thermal image quality caused by the miniaturised sensor

Objective 4. To develop dedicated data analysis algorithms for this system to detect and visualise the damage

Objective 5. To validate the developed miniaturised technique through testing a variety of materials, types of damages and within a challenging environment, in comparison to the existing active thermography system

1.4 Thesis Structure

The thesis is divided into 7 chapters, the structure of which is illustrated in Figure 1-1. A summary of each chapter is presented below.**Figure 1-1 Thesis structure**

Chapter 1 provides an introduction and a general overview of the miniaturised NDT technique. It also describes the research motivation, aim and objectives.

Chapter 2 shows a critical review of the literature and identified research gaps.

Chapter 3 shows the strategy of research methods to address each objective.

Chapter 4 proposes the sensor selection and a novel Spatial Resolution Enhancement for a Thermogram (SRE4T) technique to enhance the low-resolution thermal images caused by the miniaturised sensor.

Chapter 5 proposes the design and integration of a novel miniaturised active thermography (MAT), with its qualitative and quantitative performance evaluation of a variety of defects in composites.

Chapter 6 presents the system evaluation performed on a group of composite impact damage samples and a metal sample, meanwhile, the accessibility test is designed to verify the performance to access geometrically intricate space.

Chapter 7 concludes the research findings of this PhD project, provides a critical evaluation of the proposed solution, summarises the contribution to knowledge, and presents the future work.

2 LITERATURE REVIEW

This research primarily focuses on creating a low-cost system to perform active thermography inspection. This chapter provides an overview of the literature supporting the development of the MAT system. It is divided into two sections: NDT methods for miniaturisation, and thermography techniques. The purpose of the first section is to discuss and analyse the prospect of different NDT methods for miniaturisation, where four widely used NDTs will be discussed. The purpose of the second section is to present the current state-of-the-art of infrared sensors

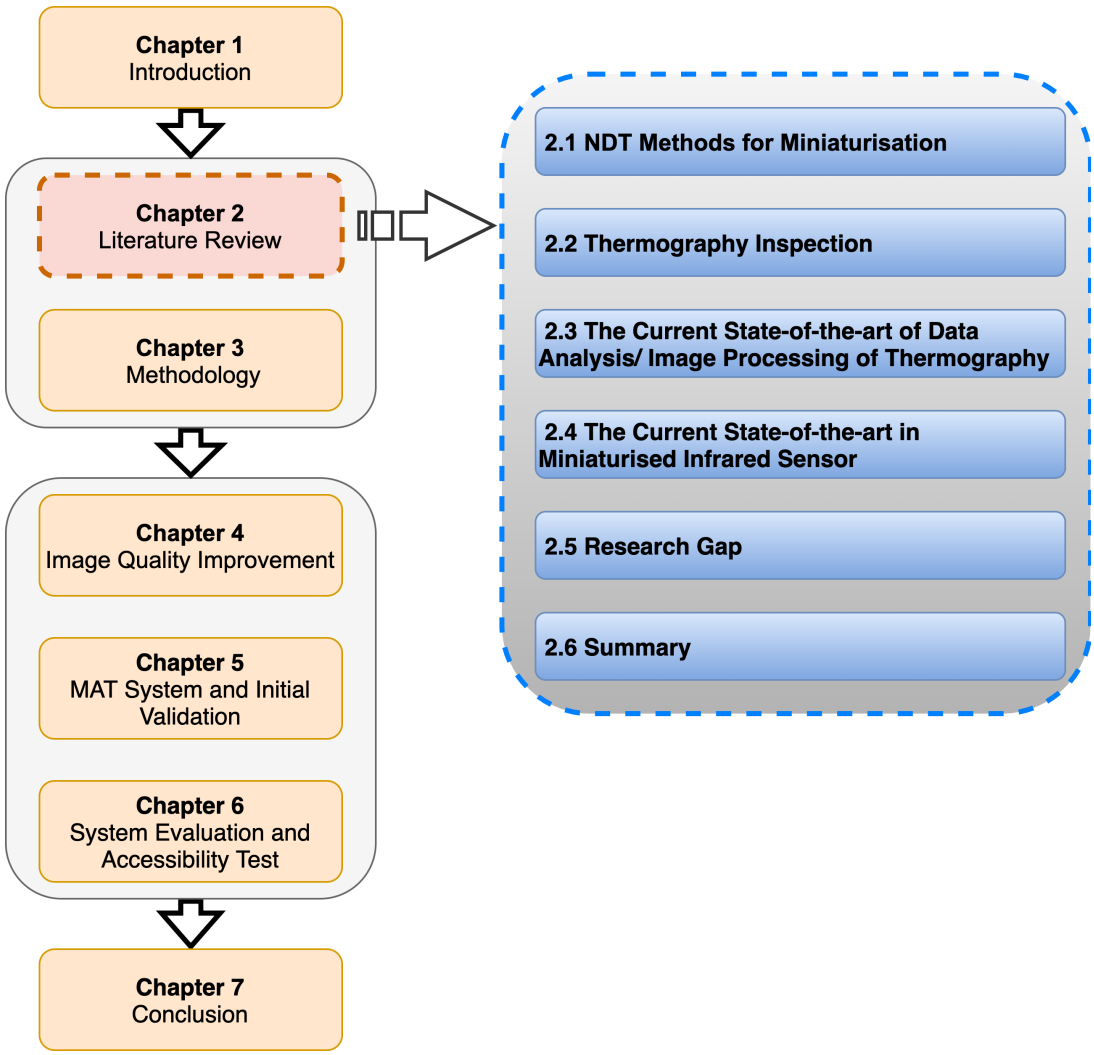

Figure 2-1 The outline of Chapter 2

and excitation sources and support the development of the miniaturised thermography technique. The outline of the chapter is illustrated in Figure 2-1.

2.1 NDT Methods and the prospect for miniaturisation

Although there are many other NDT methods, such as eddy current testing [22], acoustic emissions/EMATs [23], 3-D imaging/part of visual inspection [24] and phased array/full matrix capture (FMC) [25], which have attracted more and more investigation, this section presents four widely used NDTs, particularly for the *in-situ* inspection.

2.1.1 Magnetic Particle Inspection (MPI)

Magnetic particle inspection is one of the conventional inspection methods and is one of the oldest and most mature NDT technologies. It is widely used in the surface and near-surface detection of ferromagnetic components in various industries [26][27]. When the ferromagnetic material is magnetized, due to the discontinuity, the magnetic field lines are locally distorted, causing leakage in the magnetic field, and the magnetic marks appear under the action of the magnetic powder, showing the position, shape, and size of discontinuities. Figure 2-2 illustrates the principle and deployment example of this technique.

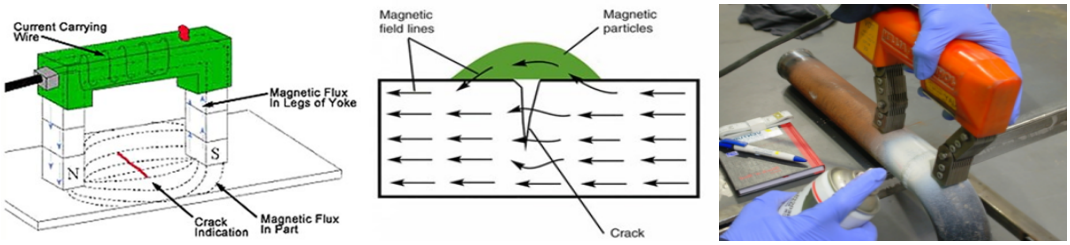

(a) (b) (c)

Figure 2-2 The schematic of Magnetic Particle Inspection: (a) shows that the magnetic field lines are formed between north and south poles when Legs of Yoke touch with the ferromagnetic material under power condition.; (b) is a schematic illustrating that the magnetic powder is piled up at the defect area. (c) *In-situ* inspection using Magnetic Particle Inspection technique.

MPI employs either electromagnets or permanent magnets. The former generally uses electrical current to produce the magnetic field, lifting power, therefore, can be controlled easily through controlling the current. However, it cannot be used in underwater environments or explosive environments [28]. The permanent magnet can be made small enough to fit into tight areas where the electromagnet based one might not be able to because the permanent magnet has no requirement of a power source or a battery [29]. However, a limitation of the permanent magnet is that it is difficult to remove the magnets from the component being inspected after the inspection. The rapid development and innovation have promoted a number of global magnetic particle equipment manufacturers, such as Italian CGM, German Karl Deutsch, US Magnaflux, French Srem, and British Johnson & Allen. Recent development includes the pulse technology for magnetic testing and demagnetisation of steel components proposed by Peter Hirsch of Germany [30] and cross and additional orthogonal magnetic coils application in components of large dimensions technology proposed by Rainer Link and Nathanael Riess of Germany [31]. The new frequency conversion and non-contact magnetisation technology proposed by Michitaka Hori and Arihito Kasahara of Japan enable non-contact stereo composite magnetisation for workpieces [32]. The improvement of magnetic particle detection technology gradually adapts to the increasingly complex detection environment, but the miniaturisation degree of magnetic particle testing equipment has not changed significantly. Taking US MAGNAFLUX as an example, its magnetic particle

(a) (b) (c)

Figure 2-3 Examples of magnetic particle detector (a) Y-7 (Electromagnet) produced by MAGNAFLUX; (b) YM-5 (Permanent magnets) produced by MAGNAFLUX; (c) RPNSS&RPNSL Permanent Magnets equipment manufactured by Johnson & Allen Company.

detector Y-7 (see Figure 2-3(a)) is the most advanced high-strength electromagnets based device at present [33]. Solid-state controls allow the operator to use Alternating Current magnetic fields for surface indications or Direct Current magnetic fields for sub-surface indications to meet all inspection needs, but this kind of equipment is still kept in the combination of traditional power supply and magnetic yoke. YM-5 (see Figure 2-3(b)) is a representative product of permanent magnets produced by the company [34]. It can find sub-surface indications during magnetic particle testing with no power supply. It also features with 40-pound dead-weight lift strength. The enhancement of the lifting force increases the degree of magnetisation of the object being inspected, which in turn increases the detection rate. Although it is optimised in the design of the overall equipment, the output of large lifting force still affects the optimisation of the equipment volume. Due to the permanent magnet, the control is not very convenient. Similar products also include RPNSS and RPNSL permanent magnets equipment manufactured by Johnson & Allen Company (see Figure 2-3(c)) [10]. These two products are relatively small, with the smallest pole gap of 37mm and the cross-section of 20mm x 25mm, but the lifting force is only 18kg. So according to the current state-of-the-art, the degree of miniaturisation of magnetic particle testing is relatively low.

2.1.2 Ultrasonic Testing

Ultrasonic testing (UT) uses special equipment to send high-frequency sound waves to penetrate materials and then uses ultrasound sensors to receive these

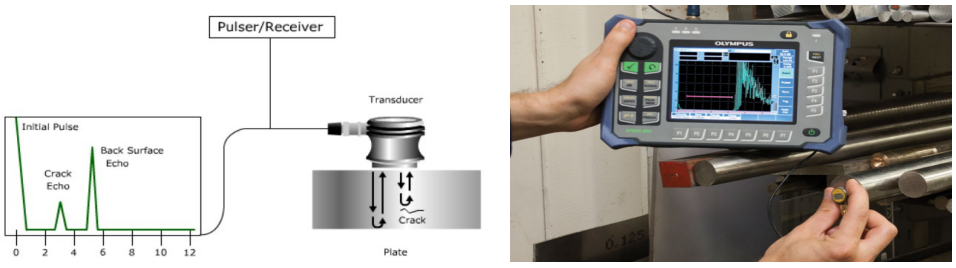

(a) (b)

Figure 2-4 (a) The schematic of Ultrasonic Testing (b) *In-situ* inspection using Ultrasonic Inspection technique.

sound waves. According to how the high-frequency sound waves are returned to the recording equipment, the determinations about material conditions and discontinuities can be made [35]. It is commonly used to inspect and evaluate the

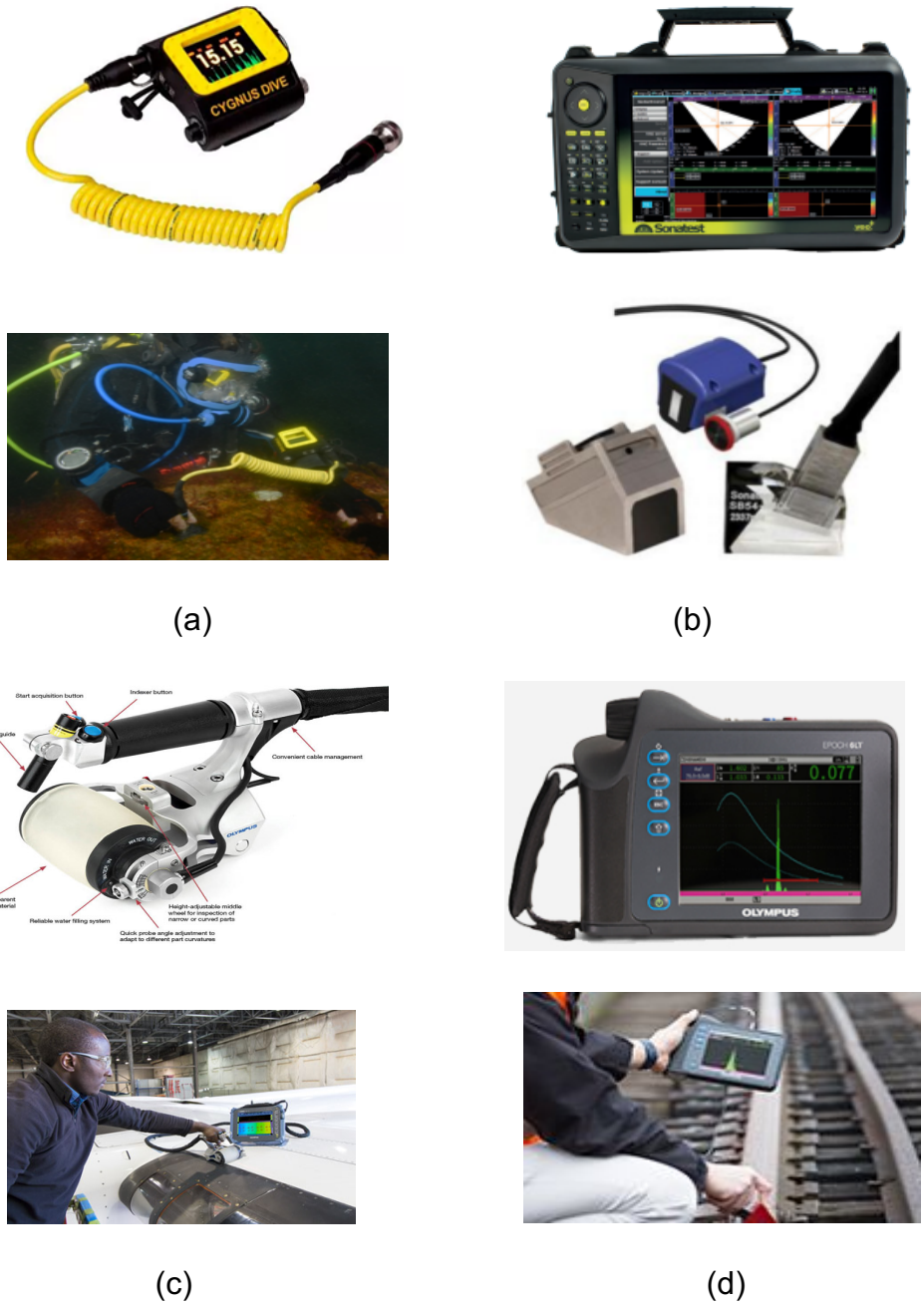

(a) (b)

(c) (d)

Figure 2-5 Examples of miniaturised UT devices (a) Cygnus Dive Wrist-Mountable underwater thickness gauge; (b) Sonatest's VEO+ Smart Portable Phased Array Solution device; (c) RollerFORM Scanner produced by Olympus; (d) Olympus's EPOCH® 6LT Portable Flaw Detector.

specific applications of macroscopic flaw detection [36], geometrical characteristics measurement [37], characterisation of changes in mechanical structure and mechanical properties of the test piece [38][39]. The principle and deployment example of this technique is demonstrated in Figure 2-4 [40]. With the increasing level of electronics, computer and software technology, digital ultrasonic testing instruments are being put into largely use. High-precision, effective control and judgment capabilities reduce human error and enhance the reliability and stability of detection. It promotes the automation and intelligent development of ultrasonic testing and evaluation.

UT is widely used and is generally divided into Ultrasonic Thickness Gauges and Ultrasonic Flaw detectors according to the function division [41][42]. Cygnus Dive Wrist-Mountable Underwater Thickness Gauge (see Figure 2-5(a)) can measure through coatings up to 20 mm thick in 300 meters depth water. Originally developed by Cygnus instruments Company, and has an accuracy is ±0.1 mm [43]. VEO+ is produced by Sonatest (see Figure 2-5(b)) combines with phased array probes. It can display S, L, A, B, C, TOFD Scan and integrate real-time imaging and 3D scanning, which enables a device to have both UT and ultrasonic Time-of-flight-Diffraction detection capabilities [44]. Although miniaturisation has not been achieved yet, it is already going forward in the process of functional intensification. For another product EPOCH® 6LT portable flaw detector (see Figure 2-5(d)) also produced by Olympus, the weight is just 1.95 pounds (890 g) with a grip-oriented weight distribution for one-handed operation [45]. The RollerFORM Scanner (see Figure 2-5(c)) uses a phased array wheel probe and zero-degree ultrasonic beams for manufacturing and maintenance inspections [46]. Common applications include delamination sizing and porosity quantification in the composite core material, as well as wall-loss monitoring in aluminium panels. The compact and lightweight improve the detection functions and efficiency. However, there is a factor that restricts the development of ultrasound miniaturisation, which is the use of a coupling agent. The traditional ultrasonic detection process requires the participation of the coupling agent, which requires the probe close to the surface of the object to be inspected during the inspection process. This is mainly to remove any attenuation caused by gaps between the

detector and the material surface, which brings inconvenience to detect the narrow area. The non-contact ultrasonic transducer methods that have been successfully developed and put into use include the laser ultrasonic method [47], the air coupling method [48], the electrostatic coupling method [49], and the electromagnetic sound method [50]. The Non-Contact Air Coupled Ultrasonic Testing technology invented by Japan Probe has largely changed the coupling agent and the contact restriction conditions [51]. Due to the use of a combination of mobile handheld devices, embedded processors, digital signal processors and Field Programmable Gate Array, ultrasonic testing instruments are gradually being developed towards low power consumption and miniaturisation, easier to carry and use.

2.1.3 Radiographic Testing

When a variety of electromagnetic (EM) spectral waves pass through a material, rays between the wavelengths of 0.01 to 10nm penetrate the material identifying its internal structure. These rays, generally are termed radiographic rays or X-Rays [52]. Rays can penetrate the material that the naked eye cannot see. When X-rays or r-rays irradiate the film, like ordinary light, it can make the silver halide in the film emulsion layer produce a latent image because of the different density of the material to the radiation. Since the absorption coefficient is different, the intensity of the radiation irradiated to the film will produce differences. The defects can be detected based on the difference between the darkness of the film after

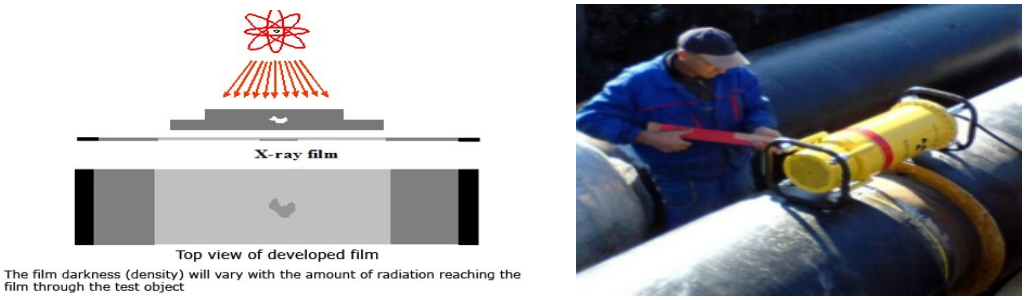

(a) (b)

Figure 2-6 (a) The schematic of Radiographic Testing (icon is top view) (b) *In-situ* inspection using Radiographic Inspection technique.

treatment in the darkroom [53]. The ray detection has high accuracy, and it can clearly display the position and contour of defects. However, because of its inherent radioactivity, the requirements for the personnel and detection environment are extremely strict to ensure safety. Therefore, most ray detection

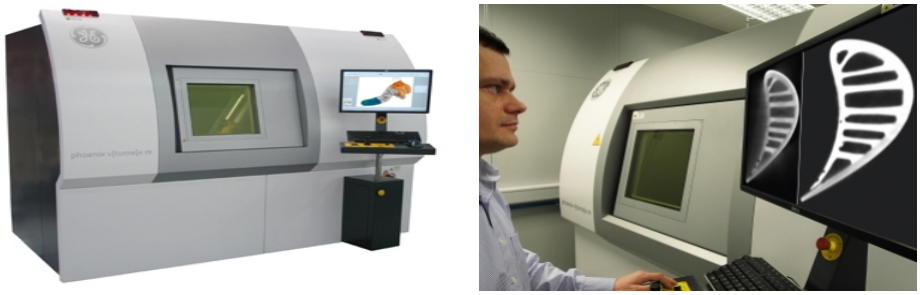

(a)

(b)

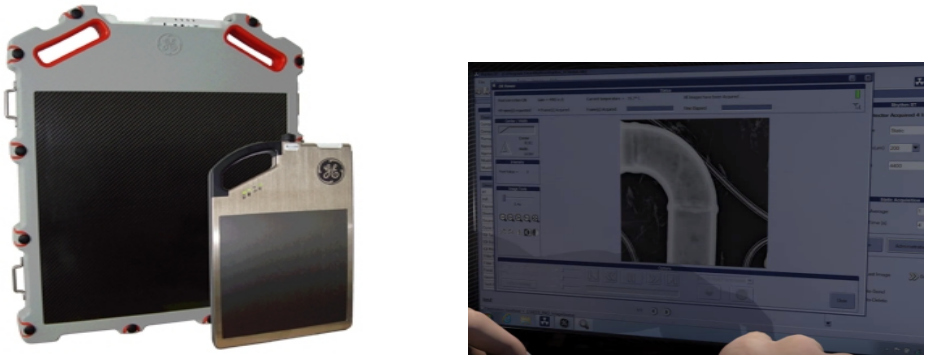

(c)

Figure 2-7 (a) Versatile Industrial CT Scanner; (b) Portble X-ray device and X-ray film; (c) DXR250C-W/DXR250U-W Wireless Digital X-ray Detector produced by GE.

technique requires the testing process undertaken in a confined space. Figure 2-6 demonstrates the principle and deployment example of this technique [54]. Meanwhile, with the development of digital radiography, digital X-ray sensors are used instead of traditional radiographic film. Less radiation is required to produce an image of similar contrast to conventional radiography. The environment of inspection will be changed as well [55].

X-ray detection and Gamma rays (γ-ray) detection are most used in *in-situ* inspections. The X-ray inspection time is short, but the penetrating ability is weak. It is not suitable for the inspection of a thick-scale workpiece. Such as XXQ-3005 produced by RSTAR, when the maximum voltage is 300 kV, the maximum thickness of penetrability is 50mm for A3 steel [56]. The portable γ-ray device is small and portable, but it has a long projection time and is not easy to control. Versatile Industrial CT Scanner (see Figure 2-7(a)) has been widely used in laboratories [57]. These devices generally have features such as high accuracy, high resolution, and high precision 3D metrology, but they are bulky and unsuitable for portable and *in-situ* inspection. Traditional *in-situ* X-ray inspections use a combination of X-ray machines and film (see Figure 2-7(b)). GE developed a product called DXR250C-W/DXR250U-W Wireless Digital X-ray Detector (see Figure 2-7(c)), which is an upgraded equipment for *in-situ* inspection [13]. In a sense, it replaces the X-ray films used in traditional ray detection and integrates portable, wireless and robust features through on-site X-ray photographing, and direct wireless transmission to the computer terminal. The DXR250C-W8”×8” detector weighs 3.5 kg (7lb) with a thickness of only 25 mm (0.98”), and ideal for inaccessible places where portability is mostly needed. Although such devices still do not have the characteristics of miniaturisation, the cutting-edge sense of technology and convenient design concept is the vane of future ray detection miniaturisation.

2.1.4 Infrared Thermography Testing

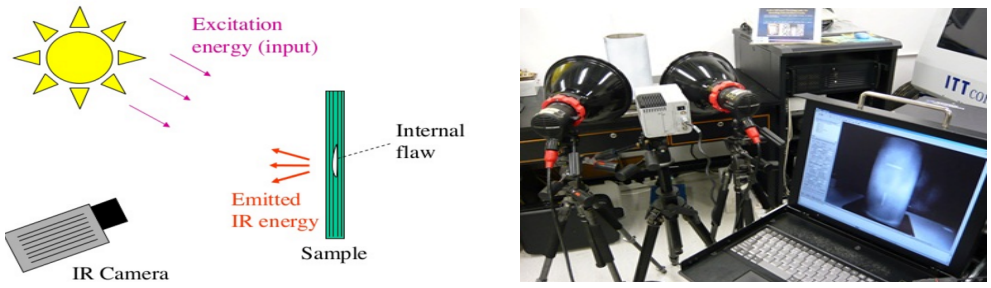

(a) (b)

Figure 2-8 (a) The schematic of active thermography testing (b) using pulsed thermography technique in the lab.

Infrared thermography technology is divided into passive (without external excitation) and active (with external excitation) modes [58]. Passive infrared thermography is a detection method based on the relationship between the surface temperature of an object and the intensity of infrared thermal radiation energy generated by the object. Based on the types of excitations, the active infrared thermography can be divided into Pulsed thermography, Lock-in thermography, Vibro-thermography, Eddy current thermography and Laser spot thermography [59]–[62]. Pulsed thermography is a well-established form of active thermography technique. The working principle of this technique is as follows (see Figure 2-8): the surface temperature of the component is increased briefly with the help of a uniform optical excitation source (e.g., flash pulse or hot gun). An IR camera or radiometer controlled by a computer (PC) records the response of the surface temperature due to the thermal excitation over a known period [63]. In a homogeneous material, the transient heat flow from the surface into the component will be uninterrupted. As soon as a thermal discontinuity appears, there is a break in the transient heat flow characteristics which shows on the surface as a hot or a cold spot indicating the presence of a foreign body in the bulk of the material. The inspection result is normally displayed in the form of an infrared image which is also referred to as the thermogram.

2.2 Thermography Inspection

Thermography inspection in terms of NDT is inspecting, analysing, and evaluating the hidden defects inside the object from the information of thermal images. Thermal images can be acquired from an infrared camera, while the abnormally hot or cold spots on the surface of an object can be observed on it. Thermographic cameras (infrared radiometer) regularly detect radiation in the wavelengths of the electromagnetic spectrum between 3 μm to 5 μm (mid-wave infrared bands) or 8 μm to 14 μm (long-wave infrared bands) [64] and generate images of the radiation, called “thermograms” [65].

For active thermography, the excitation sources usually can be divided into three categories: optical, mechanical and induction excitation [66] (see Figure 2-9). Additionally, hot or cold gas/liquids as a heat source has been revamped recently [67][68]. Both flash and laser belong to optical excitation, while ultrasonic belongs to mechanical excitation [69], and Eddy current is a typical representative of induction excitation [70].

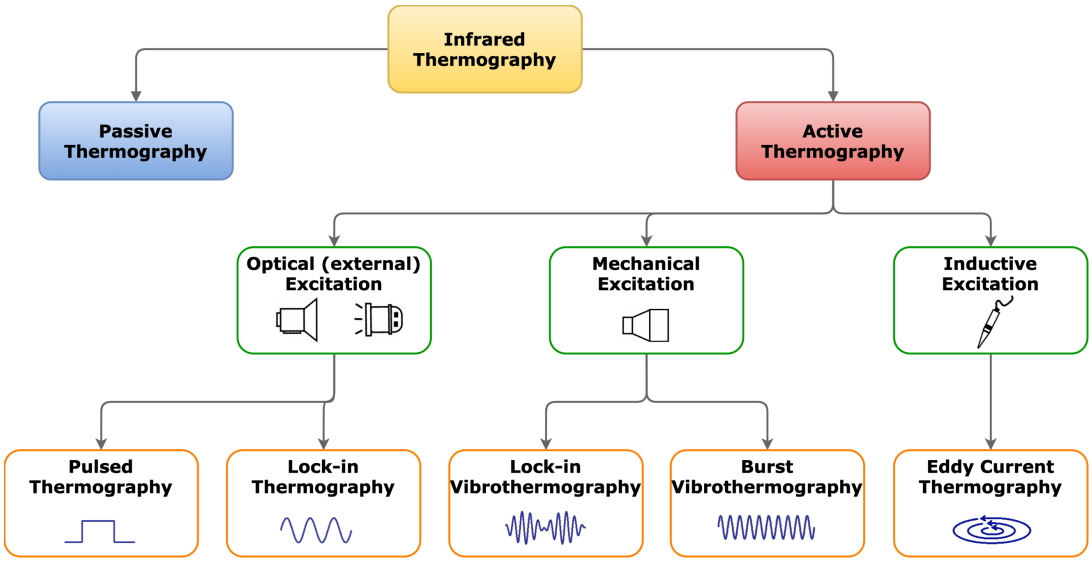

Figure 2-9 The classification of thermography excitation sources.

2.2.1 Pulsed Thermography

Figure 2-10 shows a typical set-up of pulsed thermography [71]. In pulsed thermography (high power short pulse), a Dirac heat pulse is ideally a transient waveform used to excite the specimen. According to the different thermal properties of the defects and materials, the duration of the heat pulse may vary from a few milliseconds to several milliseconds (approximately 2 - 15 ms). The flash lamps are normally used to be the excitation source. Another technique that does not need a high power of stimulation, which is long pulse thermography [72]. It is similar to pulsed thermography, but the duration of heat pulse is longer from a few seconds to several minutes (e.g., 9 seconds [73]). The halogen lamps are normally used to be the excitation source. The temperature on the surface of an object is generally recorded by an infrared camera. After the surface of the specimen is heated by excitation sources, the thermal propagates from the surface through the specimen and the cooling process is then diagnosed.

Pulsed thermography is more suitable for examining thin layers with shallow defects whilst long pulse thermography is more suitable for investigating a low

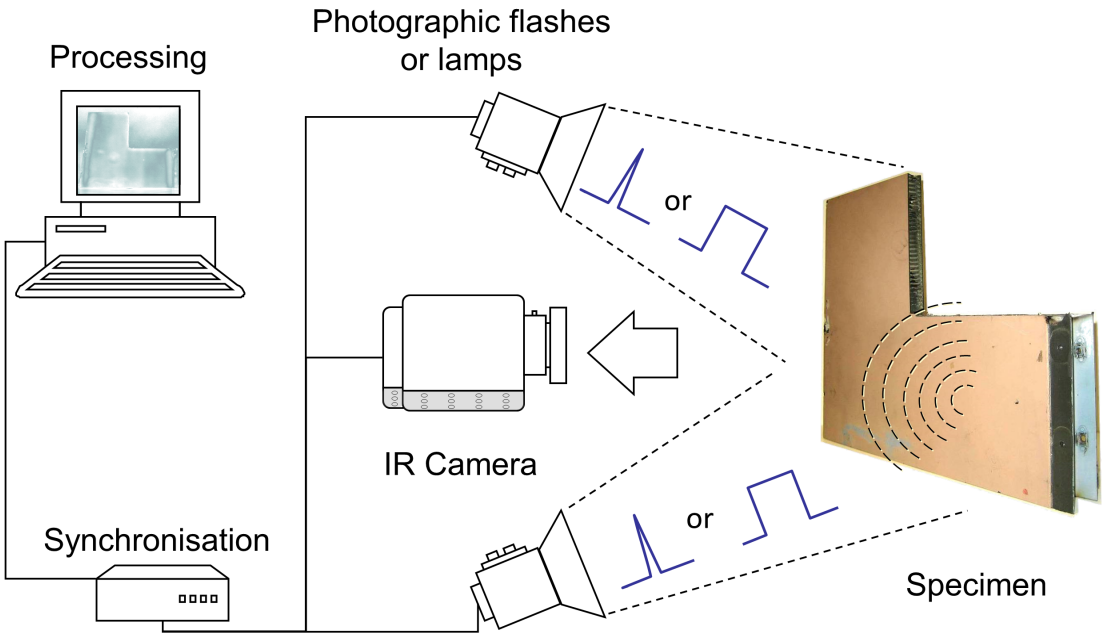

Figure 2-10 A typical set-up of pulsed thermography

conductivity material with a large structure that can be evaluated and imaged in a single shot [74].

2.2.2 Lock-in Thermography

Lock-in thermography is a periodic excitation method. It is also known as modulated thermography [64], [75], [76], [77]. Sinusoidal waves are typically used as a modulated periodic source, and the common excitation sources are halogen lamps or LED lamps. The periodic thermal wave from the excitation source propagates through the air and heat on the surface of the specimen. The heat propagates into the material and is blocked by the internal defect, which produces the change of the amplitude and phase of the response signal at the surface of the specimen. Internal defects can be evaluated from the phase shift and the amplitude of the measured signal. The typical set-up of lock-in thermography is shown in Figure 2-11 [78].

The lock-in thermography is suitable for analysing materials that have low thermal diffusivity and large surfaces. However, this approach is in general slower than other approaches such as pulsed thermography.

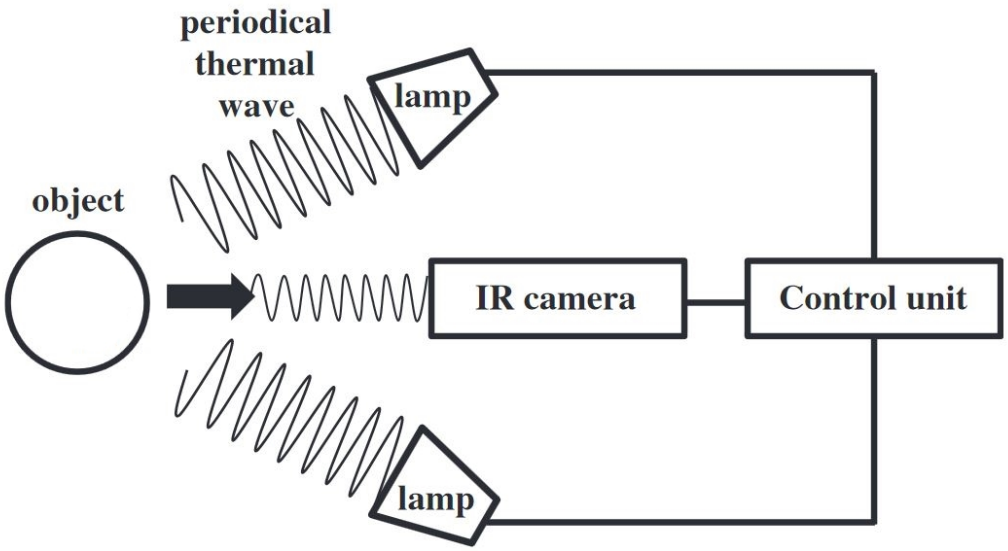

Figure 2-11 A typical set-up of lock-in thermography

2.2.3 Ultrasound Thermography

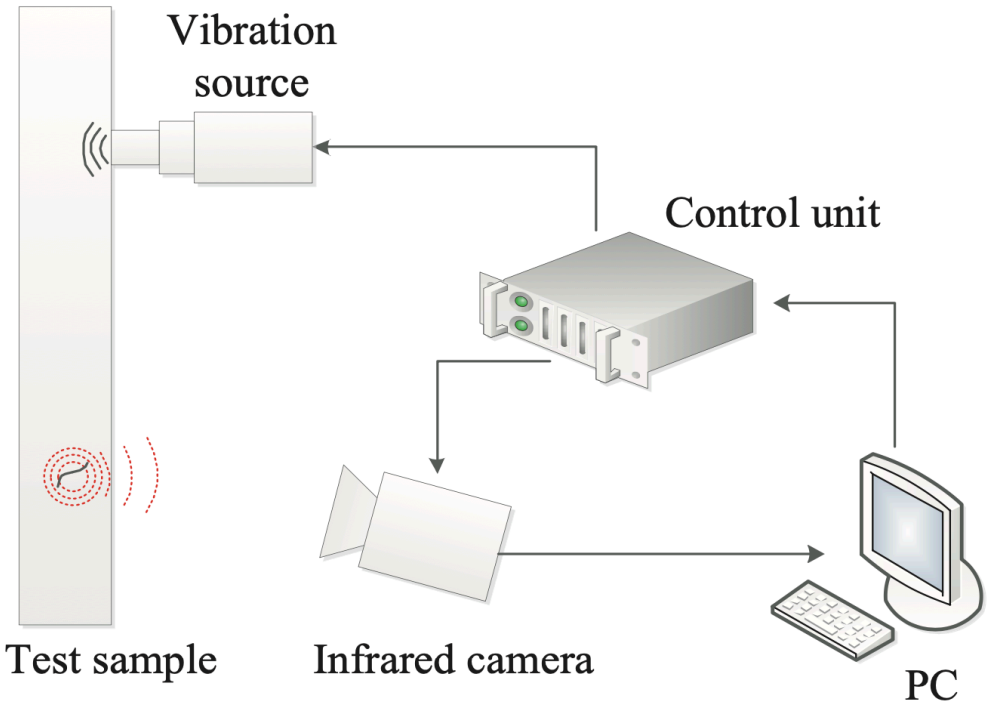

Figure 2-12 A typical set-up of ultrasound thermography

Ultrasound thermography is also well known as Vibro-Thermography (VT) [79] or thermosonic [80]. The typical set-up of ultrasound thermography is shown in Figure 2-12 [81]. The specimen is stimulated internally by a mechanical excitation source. Normally, an ultrasound wave, frequency between 15 kHz to 40 kHz, is applied to the specimen by using a transducer, which is connected to the specimen. Usually, coupling material, inserted between the transducer and the specimen, is used to avoid damage to the specimen and correct misalignment [75] [77],. The mechanical energy is transmitted into the specimen, is converted to thermal energy and spread surround inside the material in the form of a heatwave, then dissipates through the internal defect and travels to the specimen's surface and is detected by an infrared camera.

2.2.4 Eddy Current Thermography

Eddy current thermography (ECT) is induction thermography which compounds the advantages of eddy current testing and thermography. Based on the stimulation method, it can be divided into two main configurations: pulsed

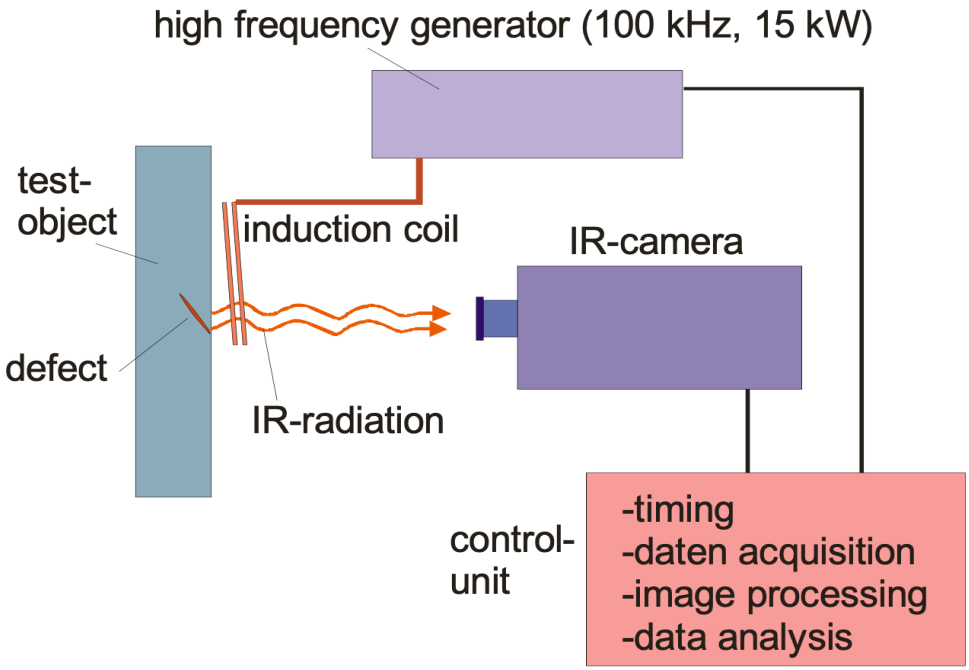

Figure 2-13 A typical set-up of eddy current thermography

approach (eddy current pulsed thermography, ECPT) and lock-in approach (eddy current lock-in thermography, ECLT) [82]. The basic configuration of eddy current thermography is shown in Figure 2-13 [83]. The sample is heated by eddy currents induced by electric currents in the coil produced from the induction heating unit. Then, the heat resistance in the conductive sample is generated. The change of the induced eddy current flow is used to detect defects through monitoring the temperature distribution on the sample's surface which is captured by an IR camera and recorded in a PC [84].

2.2.5 Comparison of Thermography

Each thermographic inspection method has advantages and limitations. Table 2-1 compares the capability of inspection between optical thermography, ultrasound thermography and eddy current thermography. From the table, it is found that all methods can detect voids subsurface defects with various types of excitation waveform (e.g. pulsed and lock-in), while optical thermography and eddy current thermography can also detect delamination defects. When considering the method of excitation, only optical thermography and eddy current

Table 2-1 The comparison of capability of different kind of thermography

Capability of Inspection	Optical Thermography	Ultrasound Thermography	Eddy Current Thermography
Contactless of excitation source	√		√
Various excitation waveform	√	√	√
Suitable for voids subsurface defect	√	√	√
Suitable for delamination defect	√		√
Suitable for surface-breaking cracks			√
Suitable for non-conductive materials	√	√	

thermography are non-contact methods. In terms of the capability of the application for non-conductive materials between optical thermography and eddy current thermography, it is found that optical thermography is more suitable than eddy current thermography. Pulsed thermography is selected because this technique offers the most rapid inspection, and also is proven as a high-performance technique to quantify subsurface defect size and depths. Laser thermography is selected because the laser has advantages in energy density, intensity, accuracy, and ease in modulation, the other key point is that it can be miniaturised.

2.3 The Current State-of-the-art of Data Analysis/Image Processing of Thermography

In the past few years, many methods of data analysis and image processing in thermography have been presented. In the early period, the temperature contrast method (TC) [85] was mainly used for defect detection purposes. There are four common temperature contrast techniques including absolute contrast, running contrast, normalised contrast, and standard contrast. The basic definition of temperature contrast is the “Absolute Temperature Contrast”, which measures the dissimilarity in temperature between a faulty region and a non-faulty region. The Peak Temperature Contrast method (PTC) [85] calculated the thermal

contrast between the defective/damaged region and an adjacent sound or non-defective region, and the frame where the maximum contrast between the sound and defective areas is chosen. The Adaptive Peak Temperature Contrast (APTC) method can improve the overall contrast between defective areas and sound areas in comparison with PTC, particularly for an ROI with multiple defects.

The temperature decay on the surface by time was normally used to analyse the defect. Most defect depth measurement methods relied on the relationship between defect depth and the temperature deviation time. Various methods evaluate the defect depth from the thermal contrast or the peak time of the first or the second derivative of the temperature decay curve. The peak slope time (PST) method [86] is corresponding to the peak time of the first derivative of temperature contrast. Defect depth can be estimated by the time at the peak slope. Zeng et al. [87] proposed a defect depth measurement based on the analysis of a theoretical one-dimensional solution of pulsed thermography [88], called the Absolute Peak Slope Time (APST) method. It was developed from the concept of the PST method. PST method needs a reference point to estimate defect depth, but the APST method does not need a reference point. The logarithmic second derivative (LSD) method [89] uses the peak time of the second derivative of temperature decay in the logarithmic scale to determine defect depth. However, finding the peak time with the second derivative method is quite sensitive to noise. Shepard [90] proposed a Thermal Signal Reconstruction (TSR) method to reduce temporal noise using a high order polynomial model to fit the raw temperature decay curve. Sun [91], [92] proposed a defect depth prediction based on a least-squares fitting method (LSF). Commonly, the curve fitting methods, including the least-squares fitting method, are not sensitive to noise. This method applies a theoretical heat transfer model to fit the temperature decay curve at each point on the surface. Based on the LSF method, the New Least-squares Fitting (NLSF) method was proposed by Sirikham [93], which has higher accuracy on defect depth estimation than the LSF method.

The Savitzky-Golay filter [94] is a digital smoothing filter, which can increase the SNR of the low resolution and reduce temporal noise. The 1st and 2nd TSR derivatives of the filtered IR images can further reduce noise and enhance the true defect.

2.4 The Current State-of-the-art in Miniaturised Infrared Sensor

The miniaturisation development of active thermography needs to consider the selection of IR cameras and the excitation source. Current portable IR cameras include FLIR ONE (see Figure 2-14(a)), Seek Compact from SEEK Thermal (see Figure 2-14(b)), and Therm-App TH (see Figure 2-14(c)) [95]–[97]. All these IR cameras benefit from the appearance of miniaturised infrared sensors. The Lepton series produced by FLIR is one of the most miniaturised infrared sensors. Lepton 3 (see Figure 2-14(d)) features with a size of 11.8 x 12.7 x 7.2 mm, a weight of only 0.9 grams, an array format of 160 x 120, a pixel size of 12 μm, and an acquisition frame rate of 8.8Hz [98]. Cranfield University has been developing an NDT device that combines an infrared camera with an endoscope, which offers visible-spectrum and infrared views to detect the inside diameter of the tube and other narrow openings space that are hard to access [99]. Active thermography uses a variety of thermal excitation sources, such as flash/pulse, lock-in, ultrasonic and laser. Another challenge of its miniaturisation is the selection of a portable and effective heating source, integration with the current existing miniaturised infrared sensors, as well as associated software development [100][101].

(a) (b)

(c) (d)

Figure 2-14 (a) FLIR One Infrared Thermography Camera; (b) Seek Compact IR Thermography Camera; (c) Therm-App TH IR Thermography Camera (d) Lepton 3 IR sensor.

2.5 Research Gap

Through the detailed review of the literature focussing on miniature NDT systems, several widely used NDT techniques were reviewed, particularly on the state-of-the-art of their miniaturisation. The feasibility and prospect to apply them to '*in-situ*' inspection have also been discussed. In comparison, the review identified that active thermography has a great prospect of miniaturisation for '*in-situ*' inspection of complex components and systems. A flexible combination of thermal excitation source and infrared sensor can create more opportunities and more possibilities for scientific inquiry and industrial inspections. Meanwhile, with the development of the 5G era, edge computing has become the trend of future development, especially in the industrial inspection stage [52]. More computing power and real-time data processing capability of inspection devices are expected to increase inspection efficiency and save time. Moreover, the miniaturised sensors have the characteristics of low resolution and low signal-to-noise ratio (SNR), resulting in a noisy dataset as these sensors easily suffer the influence and restriction of various external environments (such as temperature and spatial resolution). The development of the miniaturised NDT system, the relevant algorithms and the damage evaluation methods dedicated to miniaturised devices is thus necessary. To sum up, the research gaps include:

1. There are very limited researches on the development of the miniaturised NDT technique for in-situ inspection of industrial components.

2. Lack of algorithms and damage evaluation methods dedicated to miniaturised devices.

3. The existing methods are mainly suitable for offline analysis, lack of data processing methods for real-time processing on edge computing devices.

2.6 Summary

This chapter reviews a number of widely used NDT techniques, particularly on the state-of-the-art of their miniaturisation. The feasibility and prospect to apply them on the *in-situ* inspection have also been discussed. The review draws the following conclusions:

1) Due to its own detection characteristics, the miniaturised design of magnetic particle detection will reduce the lifting force at the time of its detection, which will affect the detection rate of its defects and affect the detection results. Therefore, with the current level of technology, magnetic particle testing will have to undergo major changes and may not be miniaturised over the next decade.

2) Portable and pocket-type ultrasonic testing equipment have become more and more popular. Meanwhile, ultrasonic testing is widely used due to its versatility, high level of functional integration and intelligence. If the coupling technology can be more mature, the development of its miniaturisation will be just around the corner.

3) Due to the influence of radioactivity and its strict requirements on the detection environment, the miniaturisation of radiographic inspection is a challenge although some efforts have been made. It is envisaged that the miniaturisation of this technology will continue to reform over the next decade where nano-CT will be further developed.

4) The excitation source and the infrared sensor in the active thermography system can be individually designed and explored in miniaturisation. According to the existing excitation sources and the development of micro-sensors, the development of infrared thermography miniaturisation is promising.

3 RESEARCH METHODOLOGY

3.1 Introduction

This chapter mainly describes the research methodology. The overview of the research approach is shown in Section 3.2. The research methods that follow each objective will be described in Section 3.3. Section 3.4 summarises the chapter. The outline of this chapter is illustrated in Figure 3-1.

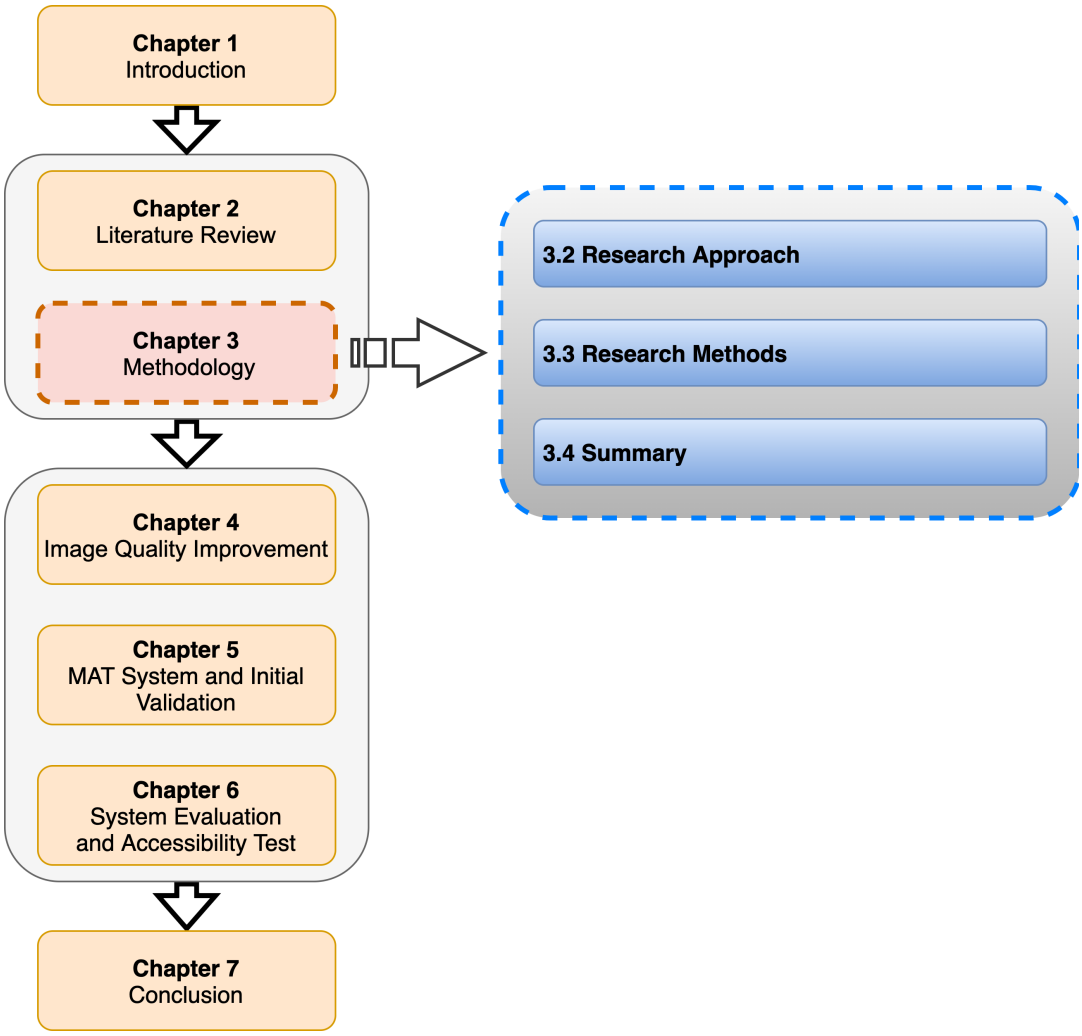

Figure 3-1 The outline of Chapter 3

3.2 Research Approach

As illustrated in Figure 3-2, there are three phases in this research: literature review, MAT system development, and evaluation.

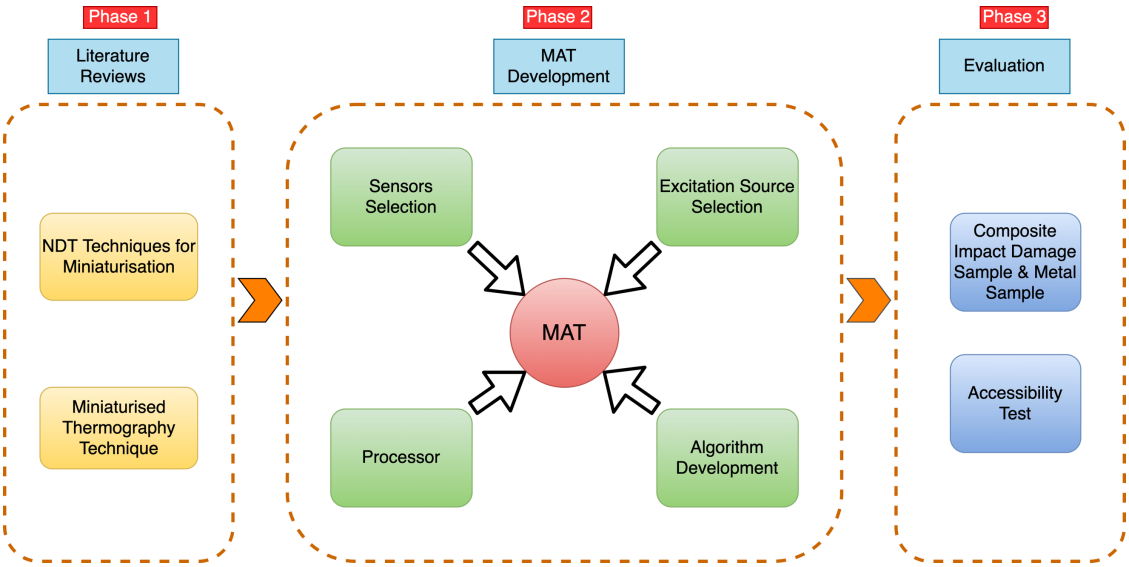

Figure 3-2 Research approach diagram.

The first phase is the literature review, which consists of two parts, the NDT technique for miniaturisation, and miniaturised thermography. It reviews a number of widely used NDT techniques, particularly on the state-of-the-art of their miniaturisation, and discusses the feasibility and prospect to apply them on the *in-situ* inspection scenario, to provide support for developing the MAT system.

The second phase is the process of the MAT system development. It contains the sensor and excitation source selection, processor selection, and algorithm development. It will be subdivided into two steps. The first step is to select the IR sensor and develop a novel imaging approach associated with a dedicated algorithm to improve the thermal image spatial resolution of the miniaturised sensor without upgrading the sensor. The second step is to develop the MAT system hardware set up and the dedicated algorithm to characterise damage.

The third phase is the process of evaluation. A set of composite impact damage samples will be used to verify the performance of the MAT system compared with

other high-resolution IR cameras. An accessibility test will be designed and conducted to evaluate the proposed system's performance to access geometrically intricate spaces.

3.3 Research Methods

3.3.1 Search the state-of-the-art miniaturised NDT techniques

It critically reviews the literature on miniaturised NDT devices, understands the frontier technology of NDT miniaturisation, identifies research gaps, and summarises it in the form of a paper.

3.3.2 Sensor selection and miniaturised active thermography system integration

According to the current sensor technology, FLIR Lepton (see Figure 3-3) was found as one of the smallest long-wavelength commercial infrared (IR) camera sensors in the market. Compared with other IR cameras commonly used in active thermography, such as FLIR SC7600 [102], FLIR A655sc [103], Lepton has a much smaller size (similar to the UK's 5 pence coin). Even if it is embedded into a breakout board, the size is just similar to the UK's 10 pence coin, as shown in Figure 3-3. As shown in Table 3-1, SC7600 has 4 times higher spatial resolution than the Lepton but is much bulky and weighs at almost 5000g in comparison with the 1g weight of Lepton. The cost of SC7600 is a hundred times higher than Lepton. SC7600 has a better specification on Noise Equivalent Temperature Difference (NETD) and frame rate primarily due to the expensive quantum core detectors combined with a cooling system achieving high levels of sensitivity [104]. Considering the fact that Lepton, which is an uncooled microbolometer based sensor, has the max. sample rate of 8.7 Hz, this research only tests its performance on composites that have relatively low thermal conductivity.

The lepton sensor will be fixed on a Dev Kit that comes with a breakout board and provides the socket for the sensor, which will be controlled by an edge computing processor. Raw images of damage features will be visualised through

an external screen. Then the two excitation sources will be tested, including flash pulse and laser. Finally, the study will integrate the IR sensor and excitation sources with a processor to capture, store, and process the data, and visualise by a mini touch screen.

Figure 3-3 Comparison of the FLIR lepton with FLIR ONE, SC7600 and A655sc

Table 3-1 Specification of the IR cameras

Model	FLIR SC7600	FLIR A655sc	FLIR Lepton
Waveband	Mid-Wave	Long-Wave	Long-Wave
Cooling Mode	Cooled	Uncooled	Uncooled
Spectral Ranges	3-5.1 μm	7.5-14 μm	8-14 μm
Pixel Resolution	640 x 512	640 x 480	160 x 120
Pixel Pitch	15 μm	17 μm	12 μm
NETD	<20 mK	<30 mK	<50 mK
Full Frame Rate	100 Hz	50 Hz	8.7 Hz
Accuracy	±1°C or ±1%	±2°C or ±2%	±5°C or ±5%
Size (mm) (L×W×H)	403×130×168	216×73×75	12.7×11.5×7.14
Weight	4950 g	920 g	0.91 g

3.3.3 Collect the data using the miniaturised system and find the approaches to improve the image quality

Addressing the limitation of low spatial resolution of the selected IR sensor, the super-resolution (SR) method will be used by synthesising multiple low-resolution images with sub-pixel movements into a high-resolution image. The technique will contribute to the improvement of the measurement accuracy of thermographic inspection and the reduction of uncertainty of defect/damage

detection. The dedicated image enhancement method for the proposed MAT system includes the experimental setup, image reconstruction, and performance evaluation.

3.3.4 Develop dedicated algorithms for the MAT system to detect and visualise the damage

Many algorithms for damage detection have been developed so far, but none of them is dedicated to a miniaturisation system. The signal-to-noise ratio (SNR) of the miniaturisation system is lower than existing systems, therefore, data pre-processing becomes important to achieve acceptable levels of detectability. Appropriate algorithms for damage detection and depth measurement will be identified and implemented to cope with this challenge. Potential approaches include principal component analysis (PCA), thermographic signal reconstruction (TSR), absolute peak slope time (APST), nonlinear system identification (NSI), least-squares fitting (LSF).

3.3.5 Evaluation of the proposed system.

Two different types of samples will be used to validate the MAT system: 1) Barely visible impact damage (BVID) samples, which will be used to qualitatively verify the performance of the MAT system. 2) Artificial samples with various sizes and depths of defect, which will be used to quantitatively evaluate the performance of the MAT system. Meanwhile, an accessibility test will be designed and conducted to evaluate the proposed system's performance to access geometrically intricate spaces.

3.4 Summary

The chapter describes the research methodology. The research approach consists of three phases: literature review, MAT system development, and evaluation. The research approach is performed to achieve the five research objectives. The novelty of this research is highlighted by three studies: thermal imaging enhancement method development, MAT system hardware set up and initial validation, system evaluation and accessibility test, which are described in Chapter 4, Chapter 5, and Chapter 6, respectively.

4 IMAGE QUALITY IMPROVEMENT

4.1 Introduction

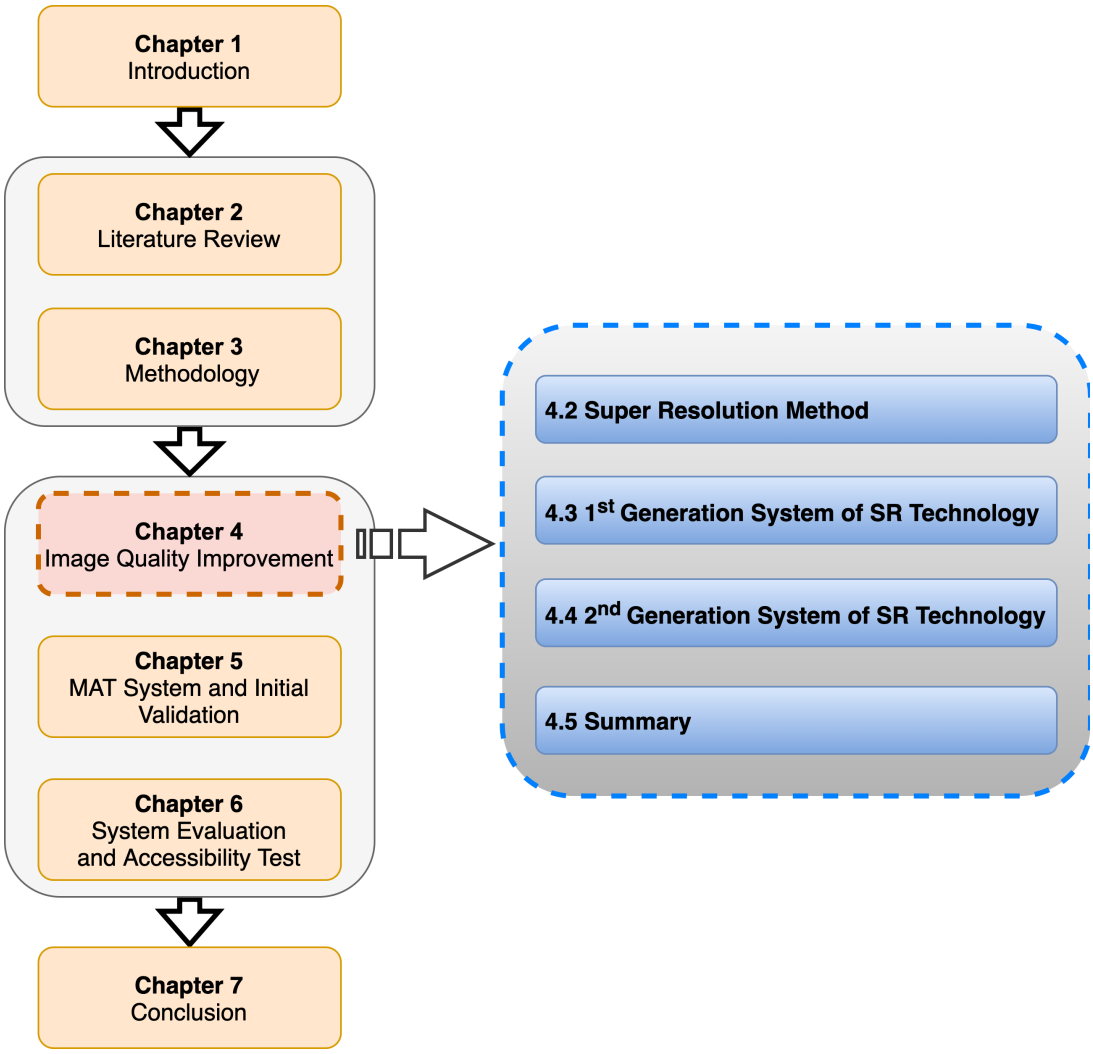

Figure 4-1 The outline of Chapter 4

This chapter introduced the Super Resolution (SR) method to improve the imaging resolution of the miniaturised sensor, through the comparison and analysis of several typical infrared thermal sensors. Further to propose a novel Spatial Resolution Enhancement for a Thermogram (SRE4T) system to significantly improve the spatial resolution without upgrading the sensor, and to maximise and guarantee the performance of resolution improvement benefiting

from accurately controlled sub-pixel movements. The Outline of the chapter is illustrated in Figure 4-1.

4.2 Super Resolution Method

4.2.1 Background

In comparison with other NDT methods such as X-ray and ultrasound, thermography has a relatively low spatial resolution (typically 640 × 480 pixels). Although some latest thermal imaging technologies have achieved higher temporal resolution [105], the spatial resolution is still the major limiting factor and bottleneck for industrial applications of thermography [106] mainly due to the refinement needed for the improved anomaly feature extraction. A high-end IR camera with a high spatial resolution is usually costly which is driven by the use of quantum detectors [107], e.g. mercury cadmium telluride, indium antimonide. Additionally, the maximum spatial resolution may be unachievable when a high sample rate has to be used for materials such as metals and alloys as they have a high thermal conductivity. Furthermore, even with the same spatial resolution, the boundary of objects or discontinuity in thermal images is not as sharp as that of digital images. This is related to their imaging principles[108]–[110]: the digital imaging system normally acquires images using CCD/CMOS sensors, which is based on the difference in the intensity of light in the range of 0.4-0.7μm reflected by the surface of the observed target, with high contrast and improved resolution. Infrared thermal imaging technology is based on receiving radiant energy with longer wavelengths in the range of 3-12μm. Due to the influence of atmospheric conditions, the minimum resolvable temperature difference between the object and the background together with the measured distance, the target is easily submerged in the dark background, which leads to the blurring effect of the acquired thermal image. It must be noted that the overall resolution is dependent on the wavelength of the electromagnetic spectrum; x-ray images show sharp boundaries, the visible spectrum shows a good level of the boundary with IR, especially the long-wave shows blurriness to the edges. Further, the existing low-cost IR cameras usually have disadvantages such as low contrast, edge blurring, large noise, low clarity, and poor ability, which make it difficult to define the

boundary and accurately measure the shape of the targets. There is a strong demand to improve the quality of thermal images without upgrading the hardware in the context of NDT and surveillance systems.

4.2.2 State-of-the-art

There are a few studies reported to improve the quality of thermal images, which are largely based on single-image enhancement or super-resolution (SR). Super-resolution is based on the idea that a combination of a sequence of low-resolution images of a scene with subpixel motion can generate a high-resolution image or image sequence. The key of SR is to capture multiple sub-pixel low-resolution (LR) images at pre-defined locations for the same scene and rebuild the high-resolution (HR) images by integrating these images and restoring the missing signals in one pixel, which greatly improves the image quality. In the category of single image enhancement, Holland and Renshaw [111] proposed a physics-based method that used the basic principles of the physics of thermal diffusion to improve the spatial resolution of the thermogram. Another attempt was done by Ashiba et al. [112] who presented a new approach based on contrast limited adaptive histogram equalisation to improve the infrared images. In the category of SR, Alam et al. [113] proposed a gradient-based registration algorithm to estimate the shifts between the acquired thermal images and then used a weighted nearest-neighbour approach for placing the frames onto a uniform grid to form a final high resolution (HR) image. The quality of the produced HR image relies on how well the sub-pixel motions are uniformly distributed. However, the shifts were caused by the vibrations from the platform on which the camera was mounted, which is uncontrollable and random. For example, commercial tool FLIR UltraMax™ [114], Sadi and Crastes [115] used an uncooled microbolometer array to produce an HR thermal imaging by taking advantage of the relative motion between the camera and the object to produce information redundancy. Kaczmarek and Borwanski [116] used time series of thermograms to reconstruct a thermal image with improved spatial resolution. Mwangi *et al.* [117] proposed a fusion of active thermography and visible imagery data, capable of producing higher-resolution thermograms based on the physical boundaries in the visible

spectrum. The sharpness of the thermogram was improved based on the additional information obtained from the digital image. Collectively, SR-based approaches usually produce better results than the single image enhancement methods because they increase the entropy of the images through benefiting from the true measurements of multiple images. Single image enhancement methods either improve the visualisation while no extra information is introduced, or apply the physics knowledge to reduce the blurring but the model to be applied is quite subjective.

4.3 The First Generation System of the Proposed Super Resolution Technology (Manual System)

According to our best knowledge, most of the existing SR-based approaches to improve the quality of thermal images focus on how to reconstruct the HR image based on the captured low resolution (LR) images, where the movements are natural and uncontrollable, and therefore, the image quality is not guaranteed. Very few studies investigate how to produce the LR images to achieve the best performance of resolution improvement.

A novel Spatial Resolution Enhancement for a Thermogram (SRE4T) system is proposed as the first-generation system to significantly improve the spatial resolution without upgrading the sensor. This research was the first to propose a methodology to maximise and guarantee the performance of resolution improvement benefiting from accurately controlled sub-pixel movements. A high-resolution thermal image is reconstructed by fusing a sequence of low-resolution images with sub-pixel movements. To achieve the best image quality, instead of benefiting from the natural movements of existing studies, a manual XY stage is used to produce a sequence of controlled sub-pixel movements. This technique contributed to the improvement of the measurement accuracy of thermographic inspection and the reduction of uncertainty of defect/damage detection. The process of the system operation included the experimental setup, image reconstruction and performance evaluation. The performance of the proposed technique was tested on both high-end and low-end thermal imagers. Both visual

and quantitative results successfully demonstrated considerable improvement of the overall quality of the thermal images.

4.3.1 Algorithm

There are two main stages to fuse the captured low-resolution raw images (LR) into a high resolution (HR) image: the image registration and the image reconstruction. Image registration aims at the estimation of motion parameters between the LR images, while image reconstruction aims at combining the registered LR image to reconstruct an HR image by using the estimated motion parameters. It should be noted that the image registration step can be skipped if the motions are perfectly controlled. For this study, this step was still implemented since the motion was controlled manually and has limited accuracy.

4.3.1.1 Image Registration

Image registration methods can be operated either in the spatial-domain or the frequency-domain. Frequency-domain methods are usually limited to global motion models, whereas spatial-domain methods usually allow more general motion models. In this research, the method developed by Keren et al. [118] was employed to estimate the shifts (both horizontal and vertical shifts) and rotations among the LR images due to its fine performance to tackle the global motion.

The relation between the horizontal shift a, the vertical shift b, and the rotation angle θ between the LR images f and g can be written as

$$g(x,y) = f(x\cos(\theta) - y\sin(\theta) + a, y\cos(\theta) + x\sin(\theta) + b). \quad (4\text{-}1)$$

Expanding $\sin(\theta)$ and $\cos(\theta)$ to the first two terms in their Taylors series expansion gives the following equation

$$g(x,y) \approx f(x + a - y\theta - x\theta^2/2\,, y + b + x\theta - y\theta^2/2). \quad (4\text{-}2)$$

Expanding f to the first term in its Taylors series gives the first-order equation

$$g(x,y) \approx f(x,y) + (a - y\theta - x\,\theta^2/2)\frac{\partial f}{\partial x} + (b + x\theta - y\,\theta^2/2)\frac{\partial f}{\partial y}. \quad (4\text{-}3)$$

The error between g and f after translation by a and b and rotation by θ, expressed as E, can thus be approximated by

$$E(a,b,\theta) = \sum \left[f(x,y) + (a - y\theta - x\,\theta^2/2)\frac{\partial f}{\partial x} + (b + x\theta - y\,\theta^2/2)\frac{\partial f}{\partial y} - g(x,y) \right]^2, \quad (4\text{-}4)$$

where the summation is over the overlapping area of f and g.

The minimum of $E(a,b,\theta)$ can be obtained by computing its derivatives with respect to a, b and θ and setting them to zero.

The difference between g and f warped by (a,b,θ) will be minimised by solving the following equation for $a, b,$ and θ:

$$\begin{aligned} \left[\sum \left(\frac{\partial f}{\partial x}\right)^2\right] a + \left[\sum \frac{\partial f}{\partial x}\frac{\partial f}{\partial y}\right] b + \left[\sum R\frac{\partial f}{\partial x}\right] \theta &= \sum \frac{\partial f}{\partial x}(f-g) \\ \left[\sum \frac{\partial f}{\partial x}\frac{\partial f}{\partial y}\right] a + \left[\sum \left(\frac{\partial f}{\partial y}\right)^2\right] b + \left[\sum R\frac{\partial f}{\partial y}\right] \theta &= \sum \frac{\partial f}{\partial y}(f-g) \quad (4\text{-}5) \\ \left[\sum R\frac{\partial f}{\partial x}\right] a + \left[\sum R\frac{\partial f}{\partial y}\right] b + \left[\sum R^2\right] \theta &= \sum R(f-g) \end{aligned}$$

where $\mathrm{R} = x\frac{\partial f}{\partial y} - y\frac{\partial f}{\partial x}$.

By solving this set of linear equations, the motion parameters $a, b,$ and θ can then be computed.

4.3.1.2 Image Reconstruction

Pham et al. [119] proposed the so-called structure-adaptive normalised convolution (SANC) reconstruction method for the fusion of irregularly sampled data obtained from the different LR images. The method is based on the normalised convolution (NC) method [120], which approximates the local signal from projections onto a set of polynomials basis functions. Employing the polynomials basis functions in the NC makes it equal to a local Taylor series

expansion. Considering a local neighbourhood centred at $s_0 = \{x_0, y_0\}$, the intensity value at position $s = \{x, y\}$ in the HR image is estimated using a polynomial expansion written as

$$\hat{f}(s, s_0) = P_0(s_0) + P_1(s_0)x + P_2(s_0)y + P_3(s_0)x^2 + P_4(s_0)xy + P_5(s_0)y^2 + \cdots, \tag{4-6}$$

where

$$x = \alpha\cos(\theta)(a + x_0) - \alpha \sin(\theta)\,(b + y_0) \tag{4-7}$$

$$y = \alpha sin(\theta)(a + x_0) + \alpha \cos(\theta)\,(b + y_0). \tag{4-8}$$

$P(s_0) = [P_0 P_1 \ldots P_m]^T(s_0)$ are the projection coefficients onto their entire polynomial basis functions at s_0.

A structure-adaptive applicability function is used in NC to localise a polynomial approximation, which gives different weights to all data points in a neighbourhood in the image. In addition, signal certainty is introduced in NC to ensure each input signal owing its certainty value and reduce the impact of outliers caused by missing samples or erroneous registration.

4.3.2 Experiments

To capture a sequence of raw thermal images with subpixel shifts in both x and y directions, an experimental setup is introduced and illustrated by Figures 4-2(a) and (b). A thermal camera is mounted on a high accuracy x-y translation stage with a resolution of ±1 μm. An infrared blackbody calibrator (OMEGA BB702), as illustrated in Figure 4-2(c), is used as the observed object. The 2.5-inch (63.5 mm) diameter target plate has an emissivity of 0.95 and can be set to a range of temperatures between ambient +32°C to 215°C. To ensure the observed object has the same temperature distribution during the data acquisition of multiple images, the temperature of the calibrator was fixed at 38°C with the room reflected temperature recorded at 22°C and a relative humidity value of 55%.

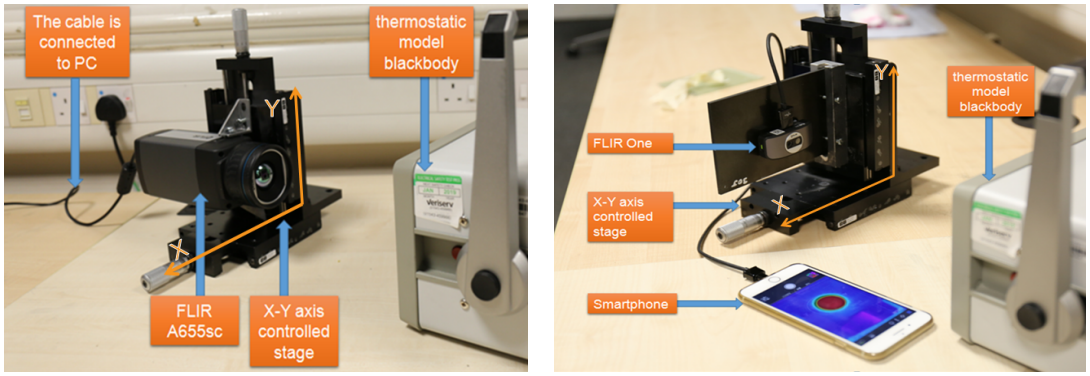

Figure 4-2 Experiment setup. (a) The experiment setup for FLIR A655sc; (b) the experiment set up for FLIR ONE; (c) The infrared blackbody calibrator (OMEGA BB702); (d) The FLIR A655sc and FLIR ONE cameras.

There are two potential motion modes: one is that the object moves and the camera is fixed, and the other is that the object is fixed while the camera moves. Both modes can introduce a global sub-pixel motion, which is key to increase the resolution of static objects. In this research, the second mode is employed. The main reason for this setup was due to the heavyweight of the blackbody calibrator and the relatively low weight of the cameras (as seen in Figure 4-2).

To create the sub-pixel movements required for the super-resolution technique, for each data capture, the translation stage moves a step of $1/a$ pixel either on x or y direction, where a $(a > 1)$ is the scale factor to achieve the movement. Assuming the object position in the thermal image on the first data capture as the reference, denoted as (x_0, y_0), the camera is moved to ensure that the following positions of the object on the thermal image are achieved:

$$\begin{cases} (x_0, y_0), \left(x_0 + \frac{1}{a}, y_0\right), \ldots, \left(x_0 + \frac{a-1}{a}, y_0\right), \\ \left(x_0, y_0 + \frac{1}{a}\right), \left(x_0 + \frac{1}{a}, y_0 + \frac{1}{a}\right), \ldots, \left(x_0 + \frac{a-1}{a}, y_0 + \frac{1}{a}\right), \\ \left(x_0, y_0 + \frac{a-1}{a}\right), \left(x_0 + \frac{1}{a}, y_0 + \frac{a-1}{a}\right), \ldots, \left(x_0 + \frac{a-1}{a}, y_0 + \frac{a-1}{a}\right) \end{cases} \vdots \quad (4\text{-}9)$$

It can be inferred from Eq. (4-1) that the total number of images to be captured is a^2.

The movement step of the translation stage depends on the intrinsic parameters of the camera and the distance from the camera to the object surface. This research uses a simple calibration process to achieve a parameter α, which indicates the required millimetre movement of the stage in the x or y direction to achieve a representative shift of one-pixel in thermal images. In this study, one thermal image was captured along the x-direction of the stage which represents a shift of 1 mm. The shift of the calibrator on the thermal images is now measured and denoted as m pixels. Then α is written as

$$\alpha = 1/m. \quad (4\text{-}10)$$

This step can then be repeated for the y-direction. To simplify the process, the same value of α for both the x and y directions.

In this study, two thermal cameras have been tested, as shown in Figure 4-2(d). The FLIR A655sc, a high-end IR camera with a resolution of 640 × 480 pixels, was used to demonstrate the proof of concept. Quantitative evaluation of the performance is conducted by this camera as it can offer a high-resolution reference image. Resolution enhancement of this camera could lead to the improvement of detection accuracy and reliability. A low-end miniature IR camera, the FLIR ONE with a resolution of 160 × 120 pixels, was then used to validate the proposed technique for a miniaturised sensor where the imaging quality is compromised for portability. This case study aims to explore the potential of SRE4T in in-situ inspection scenarios. The key parameters of the two

cameras are shown in Table 4-1. Both cameras have a similar spectral range but have a significant difference in spatial resolution, size and weight.

The distance between the camera and the calibrator surface was adjusted to ensure a good field of view of the calibrator. For the FLIR A655sc, the distance was set as 300 mm and the estimated α is 20 μm. Considering the minimal step of the stage (1 μm), 20 movements should be conducted in each direction to achieve one-pixel movement in images. Therefore, theoretically, the maximal achievable scale factor of resolution for this setting is 20. For the FLIR ONE, the distance was set as 140 mm to ensure a similar field of view (the FLIR ONE has a wider angle of view) as the FLIR A655sc and the estimated α is 40 μm. The maximal achievable scale factor of resolution in the latter case is 40. It should be

Table 4-1 Specification of the tested two cameras

Specification	FLIR A655sc	FLIR one
Spectral range	7.5 – 14.0 μm	8 – 14 μm
Resolution	640 x 480	160 x 120
Focus	24.6 mm - Infinity	150 mm - Infinity
Pixel size	17 μm	12 μm
Frame rate	50 Hz	8.7Hz
Accuracy	±2°C or ±2% of Reading	±3°C or ±5% of Reading Percent of the difference between ambient and scene temperature.
Measurement temperature	–40°C to 150°C	-20°C - 120°C
Operating temperature	-15°C to 50°C	0°C – 35°C
Size	216 × 73 × 75 mm	65x29x18mm
Weight	900g	32g

noted that the achievable maximal scale factor depends on the working distance, focus, stage step and camera specifications.

4.3.3 Performance Evaluation

This section presents the approach to quantify the resolution improvement of the proposed system. The peak signal to noise ratio (PSNR) between the super-resolved image and the original HR image is one of the most commonly used objective fidelity criteria for evaluating image quality. It can be calculated as

$$PSNR = 10\log_{10}(\frac{L^2}{MSE}), \tag{4-11}$$

where L is the maximum fluctuation in the image. The higher the PSNR, the better the improvement is. If the image is represented by 8-bit grayscale, the value of L will be 255. MSE represents the mean-square-error between the super-resolved image $\hat{X}(i,j)$ and the original HR image $X(i,j)$. It can be calculated as

$$MSE = \frac{1}{W\times H}\sum_{i=1}^{W}\sum_{j=1}^{H}\left[\hat{X}(i,j) - X(i,j)\right]^2, \tag{4-12}$$

where W and H denote the width and height of the image.

Entropy is another quantitative measure used to assess image quality when the error images for different image resolution enhancement techniques are very close to each other and it is very difficult to make a firm assessment. The entropy of a negative error image, denoted by ET, can be calculated as

$$ET = -\sum_{k=1}^{L} P\,(r_k) log_2 P(r_k), \tag{4-13}$$

where $P(r_k)$ is the probability of an intensity value r_k. The lower the ET, the better the improvement is [121].

To complement the quantitative analysis, the structural similarity (SSIM) [122] image quality measure has also been applied. The SSIM index evaluates the visual effect of three characteristics of an image: luminance, contrast, and

structure. It is based on the computation of these three components and is an inner product of them. It is defined as

$$SSIM = \frac{(2\mu_{\hat{X}}\mu_X + C_1)(2\sigma_{\hat{X}}\sigma_X + C_2)}{(\mu_{\hat{X}}^2 + \mu_X^2 + C_1)(\sigma_{\hat{X}}^2 + \sigma_X^2 + C_2)}, \quad (4\text{-}14)$$

where $\mu_{\hat{X}}, \mu_X$ are the local means for the images $\hat{X}$ and X, respectively; $\sigma_{\hat{X}}, \sigma_X$ are corresponding standard deviations; and C_1, C_2 are two constants used to avoid the instability. The higher the SSIM, the better the improvement is.

To evaluate the performance of resolution improvement qualitatively and quantitatively, three experiments were conducted.

Experiment 1: The FLIR A655sc was used and α was chosen as 20 μm. Three groups of data were collected aiming to achieve the scale factor of 2, 3, and 4 respectively. The resolution of the produced HR images is now at 1280 × 960, 1920 × 1440, and 2560 × 1920 pixels respectively. Visual comparison (qualitative evaluation) was conducted between the produced HR images and the raw images with a resolution of 640 × 480 pixels. No quantitative evaluation was conducted for this experiment due to the lack of a reference image.

Experiment 2: The FLIR ONE was used and α was chosen as 40 μm. Three groups of data were collected to achieve the scale factor of 2, 3, and 4 respectively. The resolution of the produced HR images is 320 × 240, 480 × 360, and 640 × 480 pixels respectively. A visual comparison was conducted between the produced HR images and the raw images with a resolution of 160 × 120 pixels. No quantitative evaluation was conducted for this experiment due to the lack of a reference image.

Experiment 3: The FLIR A655sc was used and α was chosen as $20a$ μm, where a is the scale factor. The captured raw images $IMR_i (i = 1,2, \dots, a^2)$ with a resolution of 640 × 480 pixels were downsized to $640/a$ by $480/a$, denoted by $IML_i (i = 1,2, \dots, a^2)$. The SR technique was then applied to these LR images to reconstruct an HR image with a resolution of 640 × 480 pixels, denoted by IMH. IMR_i now becomes the reference HR image, which allows a quantitative

evaluation on the similarity between IMH and IMR_i. Three criteria were calculated to represent the quality improvement and can be written as

$$\text{m\_PSNR} = \max_i PSNR(IMR_i, IMH), \tag{4-15}$$

$$\text{m\_SSIM} = \max_i SSIM(IMR_i, IMH), \tag{4-16}$$

and

$$\text{m\_ET} = \min_i ET(IMR_i, IMH). \tag{4-17}$$

Three scale factors of 2, 3, and 4 were tested.

4.3.4 Results and Discussion

Experiment 1

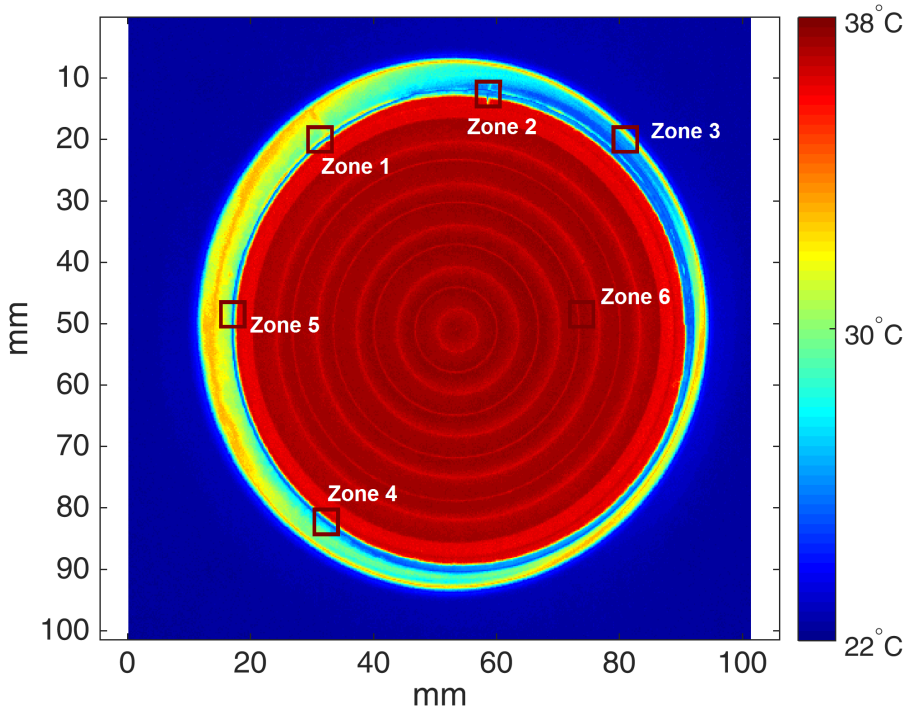

Figure 4-3 A representative thermal image of the blackbody calibrator acquired using FLIR A655sc, where the temperature was set as 38 °C and the room temperature is 22 °C. The regions of interest for resolution improvement are highlighted by rectangles.

Figure 4-3 shows a snapshot of the captured thermal image using FLIR A655sc with a spatial resolution of 640 × 480 pixels. As seen in Figure 4-2(c), the blackbody calibrator is an off-the-shelf unit with a ridged hot plate. The ridges are

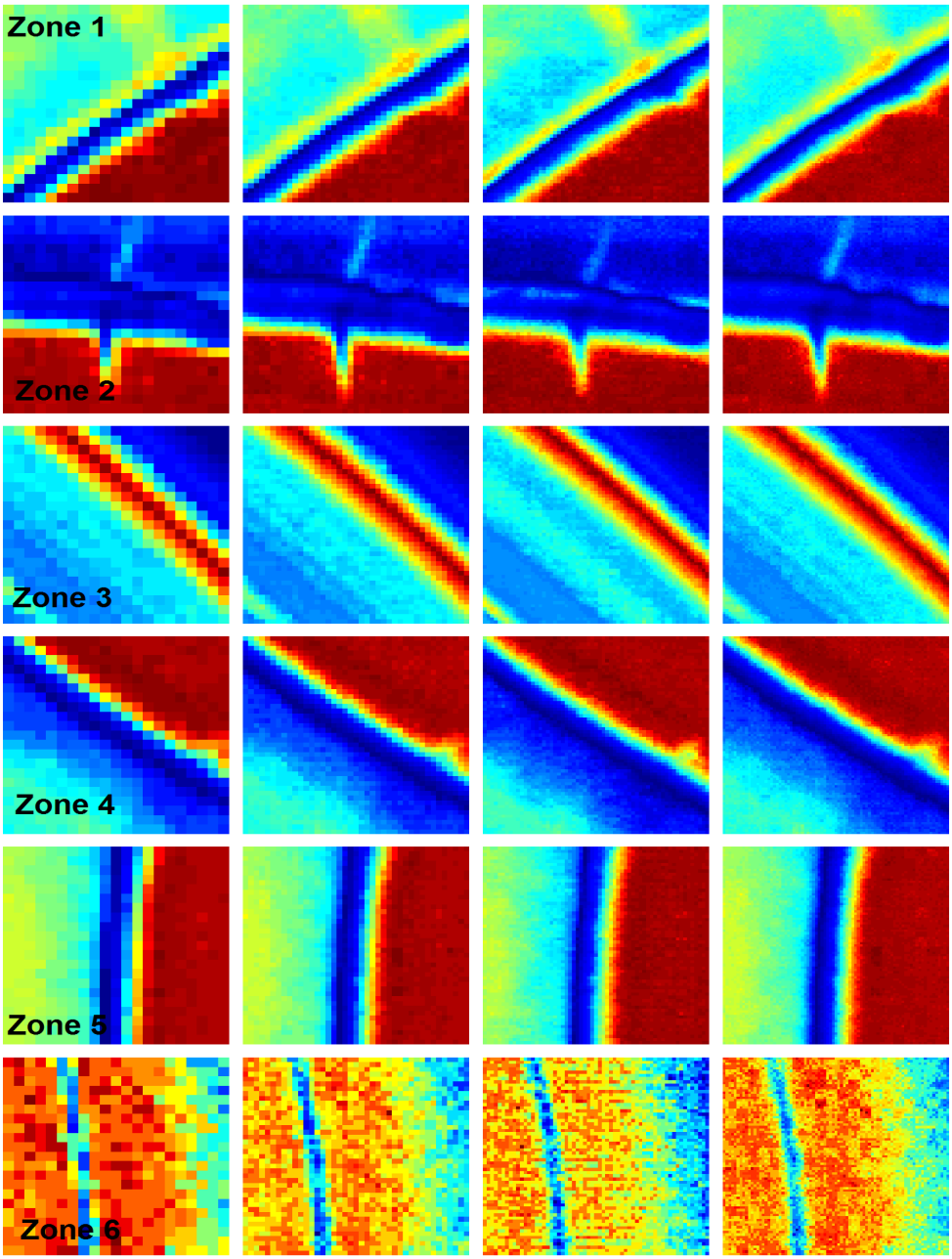

(a) raw image (b) 2x (c) 3x (d) 4x

Figure 4-4 Comparison of super-resolved high-resolution image for passive thermography using FLIR A655sc. The selected regions are highlighted in Figure 4-3 from Zone 1 to 6 respectively. It should be noted that the colormap could be different with Figure 4-3 for better visualisation.

clearly seen in Figure 4-3. In typical calibration measurements, having a flat hot plate may not be efficient as the data may be influenced by the angle of measurement and often needs to be compared with multiple sources. Having concentric ridges allows the global average of the temperature and provides a more accurate measure of the temperature.

A total number of 4, 9, and 16 images with this resolution were captured for the scale factor of 2, 3, and 4 respectively. To better demonstrate the details of improvement, six regions of interest with the size of 20 × 20 pixels, as highlighted in Figure 4-3, are compared between the raw image and super-resolved images in Figure 4-4. Zones 1-5 show the performance on high contrast areas while Zone 6 shows the performance on a relatively low contrast area. It can be clearly observed that the proposed SRE4T technique significantly improved the sharpness of both high and low contrast boundaries and is evidenced by reduced

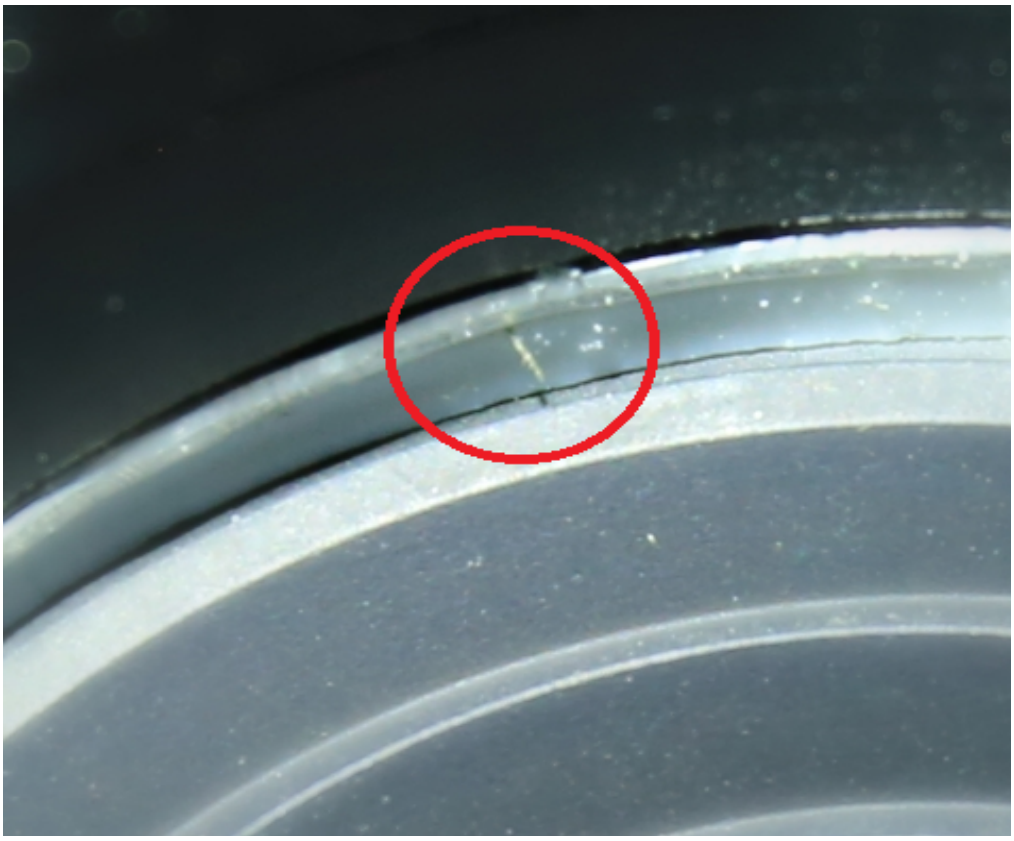

Figure 4-5 A snapshot of the observed 'v' shape feature (red circled) shown in Zone 2.

pixelation and improved sharpness of the image. With the increment of the scale factor, more and more details have been recovered in the HR images. The selected zones also include different directions of the boundary, including 0º (Zone 2), 45º (Zone 1, 3 and 4), 90º (Zone 5 and 6). Results demonstrate that this system can improve spatial resolution in all observed directions. In Zone 2, the 'v' shape feature is presented in a much clearer manner using the scale factor 4, in comparison with the raw captured image. Figure 4-5 shows a digital image of Zone 2, where the small feature can be clearly observed. This level of improvement is unlikely to be achieved using the traditional interpolation-based approach.

To explore more details of improvement, a vertical cross-section in the middle of the image for Zone 2 and a horizontal cross-section for Zone 5 are shown in

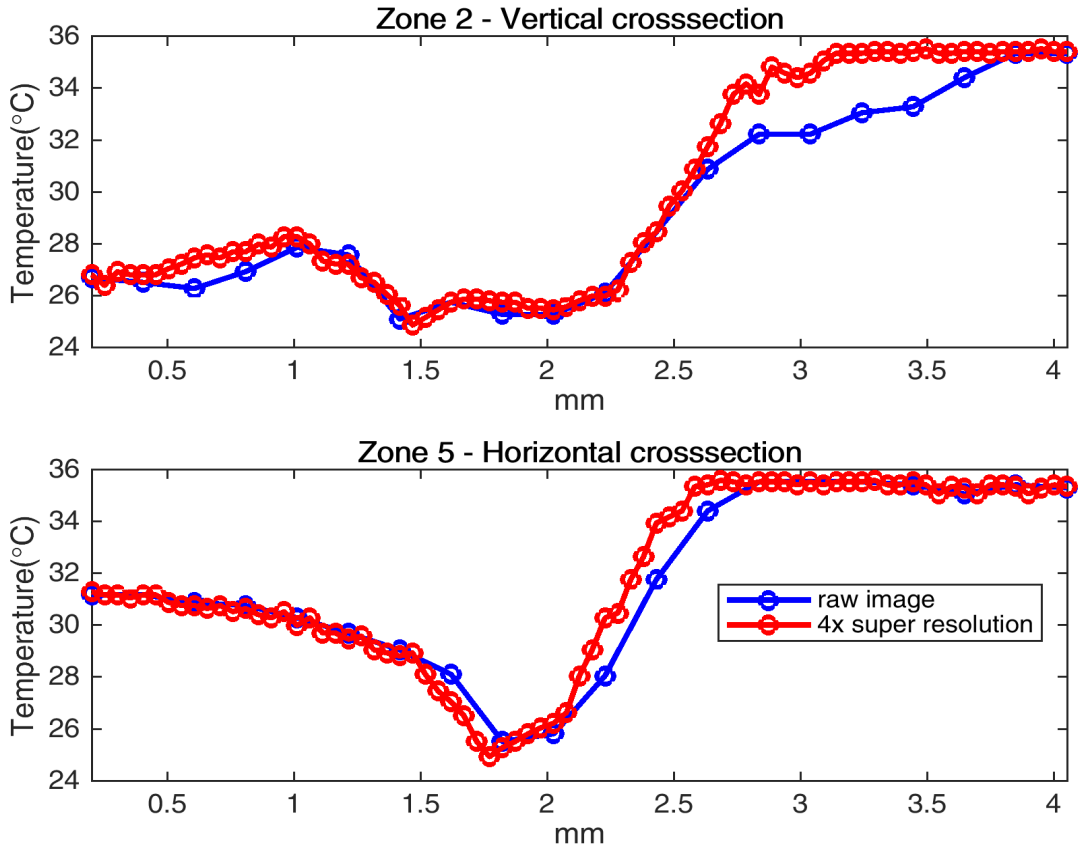

Figure 4-6 1D plots comparison between the raw LR image and the 4x super resolution image using FLIR A655sc.

Figure 4-6 to compare the difference between the raw image (denoted by the blue curve) and the HR image (denoted by the red curve) with the scale factor 4. It can be observed that the red curve has a higher slope than the blue curve between the region of 2-3 mm along the x-axis. This observation suggests that the produced HR image is a better representation of the ground truth, where the black body has a sharp temperature change in that region.

It should be noted that the performance of the introduced technique highly depends on the accuracy of the motions. Figure 4-7 plots the comparison between the estimated motions (blue dots) using the employed image registration method and the ideal motions (red dots) for the three scale factors. The absolute errors of both directions are shown in Table 4-2. It suggests that a) the error is

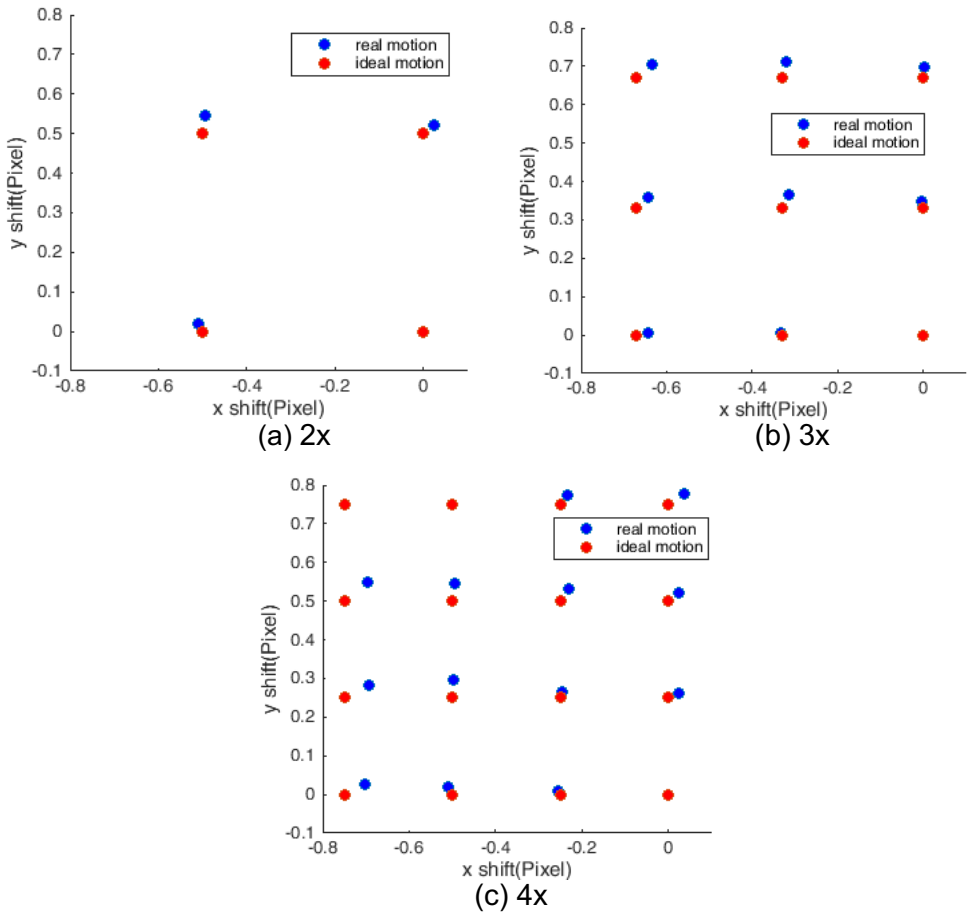

Figure 4-7 Measured motion in x and y directions for the thermal image using FLIR A655sc when the IR camera moves (blue dots), where the ideal motion parameters are also plotted (red dots).

Table 4-2 Absolute errors of motions for FLIR A655sc

Scale factor	X axis (pixel)	Y axis (pixel)
2	0.0099±0.0097	0.0215±0.0191
3	0.0127±0.0123	0.0220±0.0159
4	0.0240±0.0207	0.0294±0.0172

smaller than 0.03 pixels for both directions; b) the error in the y-axis is higher than that in the x-axis which may be due to the stage layout or the fact that α was calibrated in the x-direction only; and c) the error increases following the

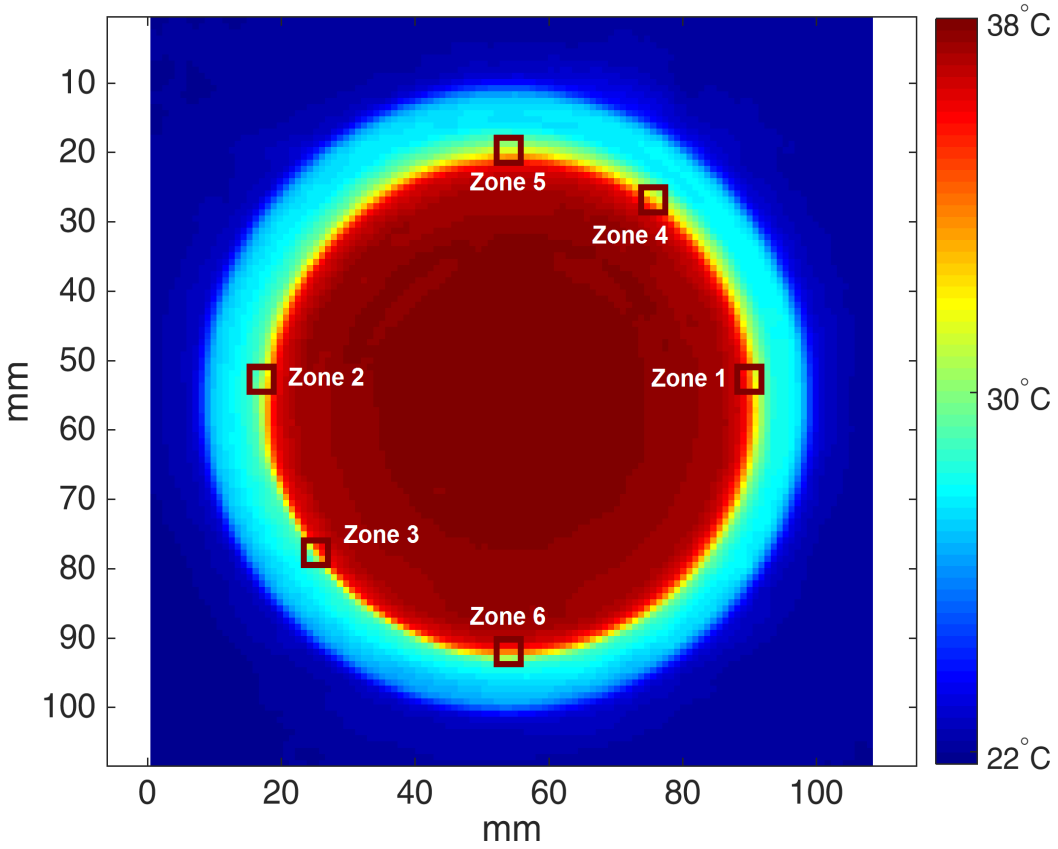

Figure 4-8 A representative thermal image of the blackbody calibrator acquired using FLIR ONE, where the temperature was set as 38oC and the room temperature is 22 oC. The regions of interest for resolution improvement are highlighted by rectangles.

increment of the scale factor, which is potentially caused by human error due to the reduced movement step of the stage. The observation c) also indicates that the maximum scale factor maybe not be achievable due to the increased error of motion following the increment of the scale factor.

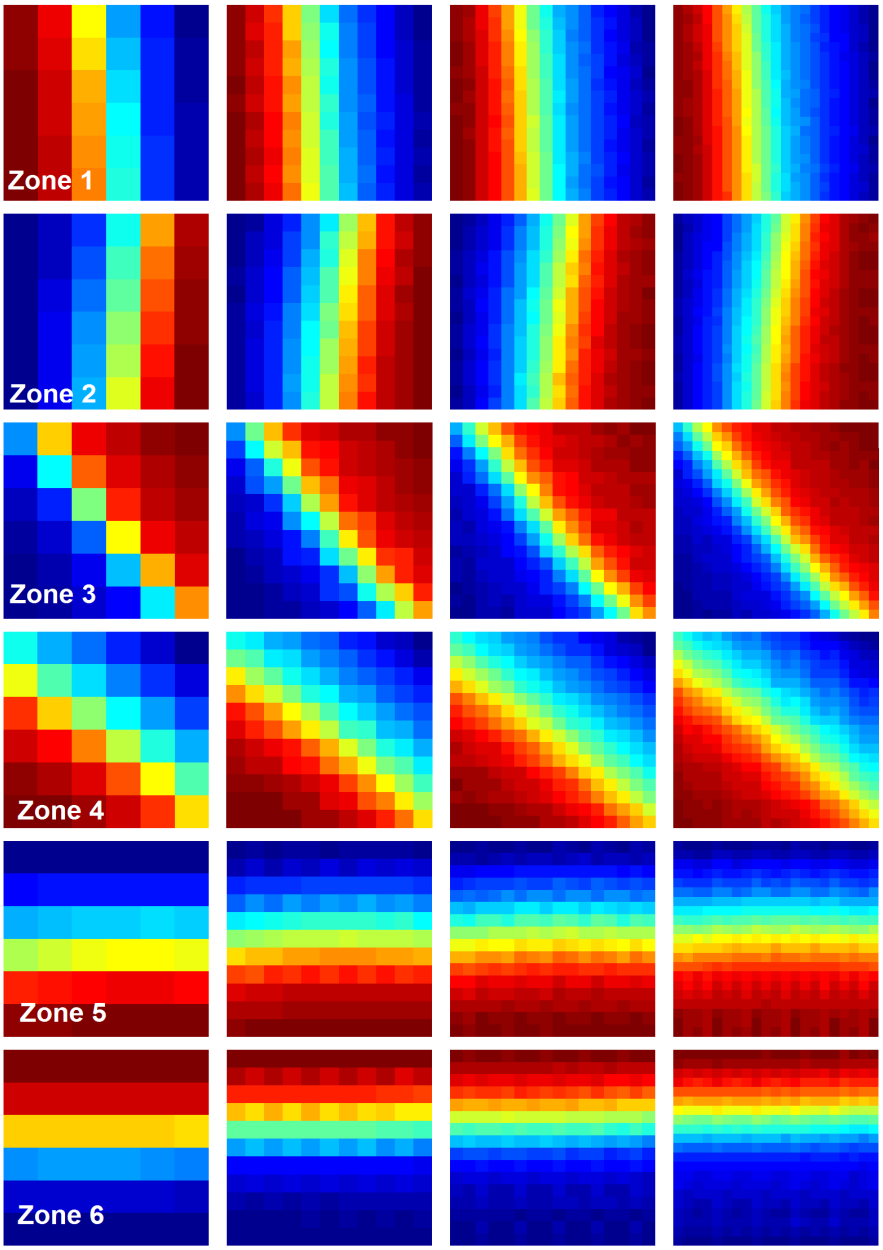

(a) raw image (b) 2x (c) 3x (d) 4x

Figure 4-9 Comparison of super-resolved high-resolution image for passive thermography using the FLIR ONE. The selected regions are highlighted in Figure 4-8 from Zone 1 to 6 respectively. It should be noted that the colormap could be different with Figure 4-8 for better visualisation.

Experiment 2

Figure 4-8 shows a snapshot of the captured thermal image using FLIR ONE with a spatial resolution of 160 × 120 pixels. In comparison to Figure 4-4, the poor, degraded quality of the image can be observed. In line with the lower pixel resolution, the wider angle of view, miniature sensor size and a large stand-off distance clearly contribute to the image quality. Further, the image shows a great deal of pixelation even at the full field of view even before reviewing the highlighted zones of interest. Super-resolved results of the highlighted six regions of interest with the size of 5 × 5 pixels (to ensure the same spatial size as Experiment 1) are shown in Figure 4-9. It can be observed that the image

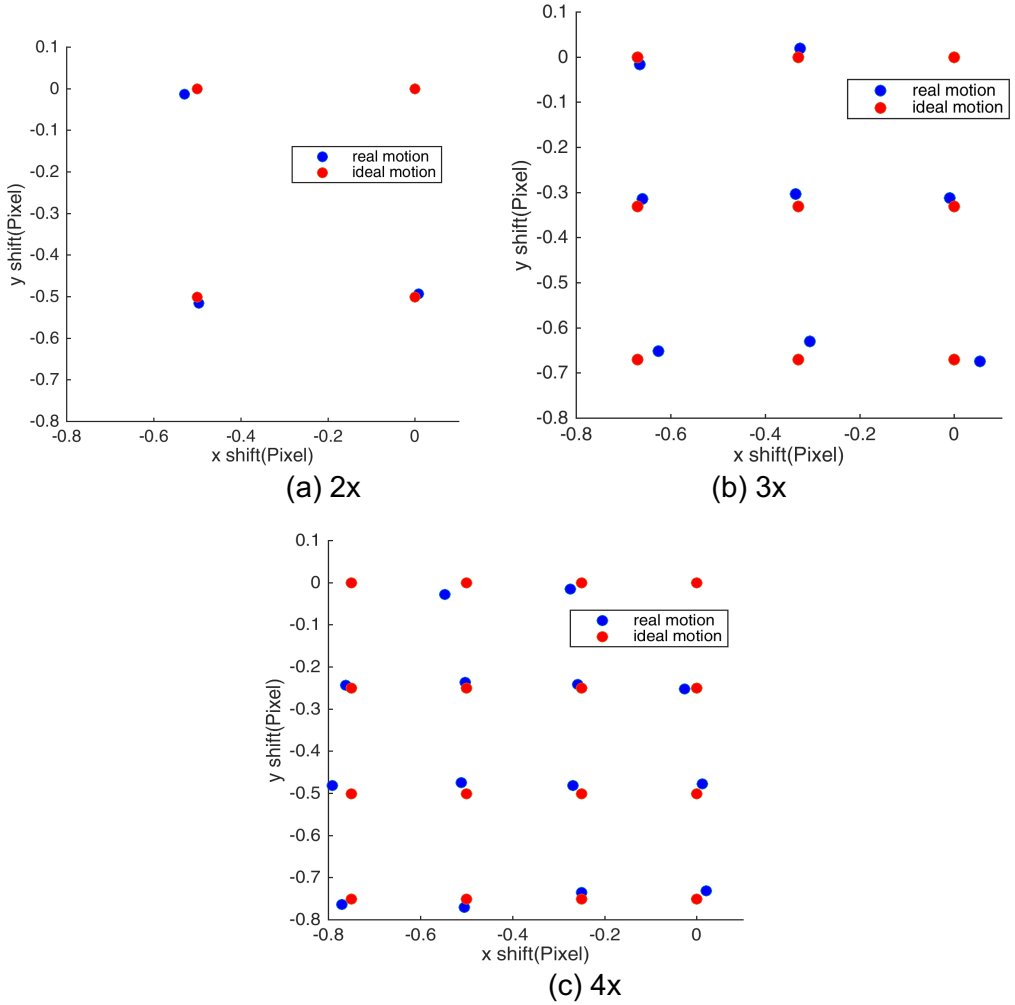

Figure 4-10 Measured motion in x and y directions for the thermal image using FLIR ONE when the IR camera moves (blue dots), where the ideal motion parameters are also plotted (red dots).

sharpness on boundaries has had a large improvement for each direction. The image quality becomes better and better following the increment of the scale factor. However, the level of improvement is not as significant as that of Experiment 1, even though the motions applied are very close to the ideal values, as shown in Figure 4-10.

Experiment 3

This section aims to quantify quality improvement using the proposed technique. The well-accepted nearest neighbour and *bicubic* interpolation method are selected as the baseline. Each IML_i was applied by these interpolation methods and compared with IMR_i to calculate the PNSR, SSIM and Entropy for each pair. The maximum of PNSR and SSIM, and the minimum of Entropy were then calculated, based on Eqs. (4-15) - (4-17), to represent the improvement of the interpolation methods.

Table 4-3 Quantitative performance comparison of the proposed technique with classic interpolation methods for experiment 3

	Scale factor	Nearest interpolation	*Bicubic* interpolation	Proposed method
m_PSNR	2	31.96	34.27	**41.70**
	3	31.32	36.30	**40.65**
	4	28.60	32.12	**35.36**
m_SSIM	2	0.94	0.96	**0.97**
	3	0.93	0.96	**0.96**
	4	0.91	0.94	**0.95**
m_ET	2	3.54	2.39	**2.24**
	3	3.64	2.67	**2.47**
	4	3.56	2.80	**2.63**

The comparison of calculated criteria for two interpolation methods and the proposed technique is as shown in Table 4-3. Taking the m_PSNR values for example, it can be calculated that the proposed method produced

$$(41.70 - 31.96)/31.96 = 30.5\% \quad (4\text{-}18)$$

$$(40.65 - 31.32)/31.32 = 29.8\% \quad (4\text{-}19)$$

$$(35.36 - 28.60)/28.60 = 23.6\% \quad (4\text{-}20)$$

increment against the nearest neighbour interpolation for the scale factor 2, 3, and 4, respectively. In comparison with the most well-accepted *bicubic* interpolation, our method produced 21.7%, 11.9% and 10.1% increment in percentage. Similar observations are applicable on m_SSIM and m_ET. The proposed method consistently produced the best results with a significant margin.

Figure 4-11 plots the visual comparison between the raw HR image (640 × 480 pixels), down-sampled LR image (160 × 120 pixels), the *bicubic* interpolated HR image (640 × 480 pixels) and the HR image (640 × 480 pixels) produced by the SRE4T system with the scale factor of 4. A region of 120 × 120 pixels of the HR image is shown to better visualise the difference. It can be observed that the proposed method produced a much better recovery of the ground truth. Whilst, achieving the image close to the raw HR image would be an ideal case, the sensor currently does not come with that level of refinement in the real case, and is evidenced by the LR image. The boundary on the *bicubic* interpolated image improved from the pixelated LR image, but the image now includes a minor distortion combined with blurriness of the image boundary. The super-resolved image however shows significant improvement in comparison with the LR image. Further, the sharpness of the image seems to have also improved and it is a better image in comparison with the *bicubic* interpolated image. The only minor downside is that the outer edge which is close to the reflected temperature of the room adds edge artefacts (the boundary between blue and yellow band), whereas the high-temperature bands (represented by the various shades of red) shows a true similarity with the raw HR image indicating that the performance of the sensor

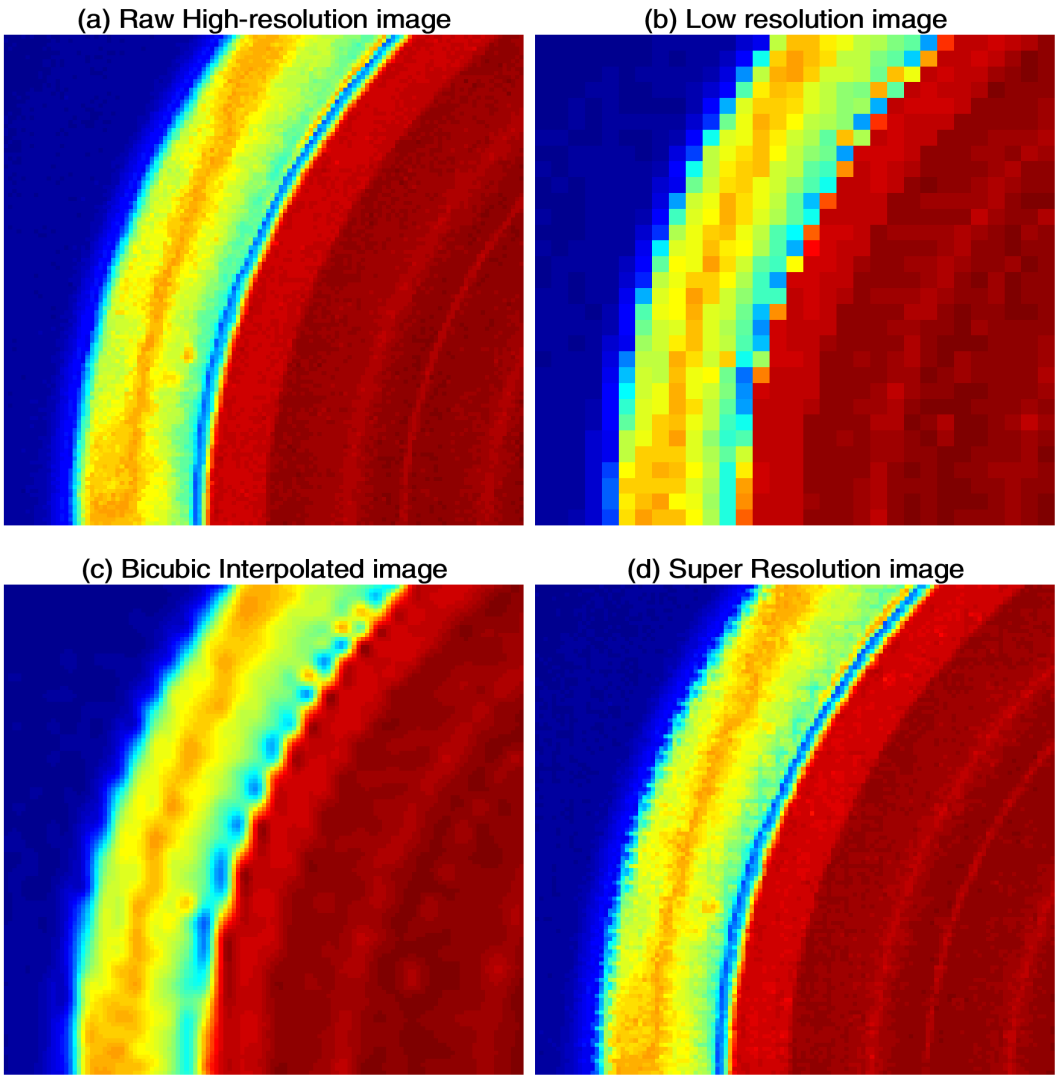

Figure 4-11 Comparison of the raw high-resolution image resized low-resolution image, the bicubic interpolated high-resolution image and the super-resolved high-resolution image using the proposed technique for the scale factor of 4.

above the reflected temperature could improve the overall quality of the object being investigated.

Motion mode: This study introduced a representative method that allows for global motions to be incorporated during data capture, where the IR camera was mounted onto the XY translation stage. The choice of using an appropriate method needs to be evaluated to achieve controlled motion, which is critical to improve the image quality. For instance, the global motion should be achieved by considering if the camera can be mounted onto a suitable translation stage or the

sample being tested. Additionally, an appropriate field of view must be chosen to ensure only the targeted object is shown in the scene, through selecting the region of interest, changing the lens, or adjusting the working distance.

Passive and Active mode: It should be noted that this study only focused on passive thermography where there is no excitation involved and the temperature distribution of the object does not change. The proposed SRE4T technique also has the potential to be applied to the pulsed flash thermography where the temperature of the object changes and the data is recorded as a function of time. One uncertainty introduced by the active mode, which could affect the performance, is the applied heat. The SRE4T technique assumes that the thermal behaviour of the object does not change for tests with different motions. It is difficult to control the heat source to ensure the heat applied on the object surface is the same for multiple tests as the system is still analogous. The second difficulty is that the images selected for registration and reconstruction must be extracted at the same timestamp. This can be challenging due to the limitation of the sample rate and the potential difference from the initial temperature.

Maximal achievable scale factor: Theoretically, this value depends on the working distance, stage step and camera specifications. The results in this section have shown that the accuracy of motion control becomes more and more challenging following the increment of the scale factor. It could be caused by human error when operating the stage, or the physical limitation of the stage. One potential solution is to automate this process by using a motorised XY translation stage. The stage movement, data capture and image reconstruction can be automatically implemented using an algorithm. The advantages are that 1) the motion error caused by a human can be reduced; 2) the operating speed of this system will be much faster.

4.3.5 Summary

Aiming to advance thermography by improving its accuracy and reliability, and adaptability on in-service inspection, this section proposes a SRE4T system to improve spatial resolution benefitting from accurately controlled sub-pixel movements. Both quantitative and qualitative results, for a high-end IR camera

and a low-end IR camera, showed that this solution can significantly improve the spatial resolution of the acquired thermal images at the expense of consuming more time during data collection and the extra cost of the translation stage that is usually much cheaper than upgrading to a high-resolution IR camera.

It should be noted that the experiments focused on passive thermography, where it is assumed that the thermal diffusion during data acquisition is saturated and that no external pulse or excitation has been used to alter the diffusion. The speed to capture data is therefore not important theoretically. However, for real applications, it is always suggested to maximise the sample rate through an automated fast-moving XY translation stage.

This technique will potentially be applied to active thermography to advance NDT, where the challenge is that, significant thermal diffusion takes place during data capture. Particularly, for high thermal-conductivity materials, such as metals and alloys, the thermal diffusion is quick, and the sample rate must be fast enough to ensure there is no or very limited thermal diffusion change in-between the captured low-resolution images. Such a problem could be mitigated through automatically controlling a high-speed camera and fast-moving stage, but the problem cannot be solved entirely. Therefore, this solution is more suitable to inspect low thermal-conductivity materials, such as Carbon Fibre Reinforced Polymers (CFRP). Another solution is conducting a multiple-inspection process with identical inspection parameters except shifting the relative position between the camera and the sample, and then registering and reconstructing the low-resolution images from the same time-stamp.

The proposed solution is also straightforward to extend to digital imaging. The ultimate aim is to advance the capability of the existing sensor through enhanced signal and image processing, thus achieving improved information on the features that will help discriminate the part with added confidence. Features that were once invisible, now become visible, the measurement accuracy is improved, which improves not just the overall performance but also our ability to make confident decisions based on the thermogram. Meanwhile, with the reduction of instrument cost, it is envisaged that this work will be adapted to both passive and

active thermography and will encompass the multidisciplinary field of digital imaging.

4.4 The Second Generation System of the Proposed Super Resolution Technology (Automatic system)

To achieve faster speed, better control and better image quality based on the first-generation system, an automatic and controllable XY stage is upgraded and used to produce a sequence of controlled sub-pixel movements. The second-generation system is an automatic and controllable spatial-resolution improvement technique by fusing a sequence of low-resolution images captured by precisely controlling the position between the specimen and the camera. The performance of the proposed system was tested on both digital and thermal imaging to inspect electronic boards.

4.4.1 Algorithm

The algorithms are the same as the first-generation system. There are two main stages to fuse the captured LR raw images into an HR image: image registration is used to estimate motion parameters between the LR images, while image reconstruction is used to combine the registered LR images to reconstruct an HR image by using the estimated motion parameters. In this system, the method developed by Keren et al. [118] was employed to estimate the shifts (both horizontal and vertical shifts) and rotations among the LR images due to its fine performance to tackle the global motion. In terms of image reconstruction, it will be used the structure-adaptive normalised convolution (SANC) reconstruction method [119] proposed for the fusion of irregularly sampled data obtained from the different LR images.

4.4.2 Experiments

The entire experiment consisted of two parts, the digital camera Super-Resolution experiment and the IR camera Super-Resolution experiment. The experimental setup is shown in Figures 4-12(a) and (b), and Figure 4-12(c) shows

all the equipment involved in the experiment. The digital camera and IR camera are fixed on the tripod to fix the position. Two Printed Circuit Board (PCB) A and

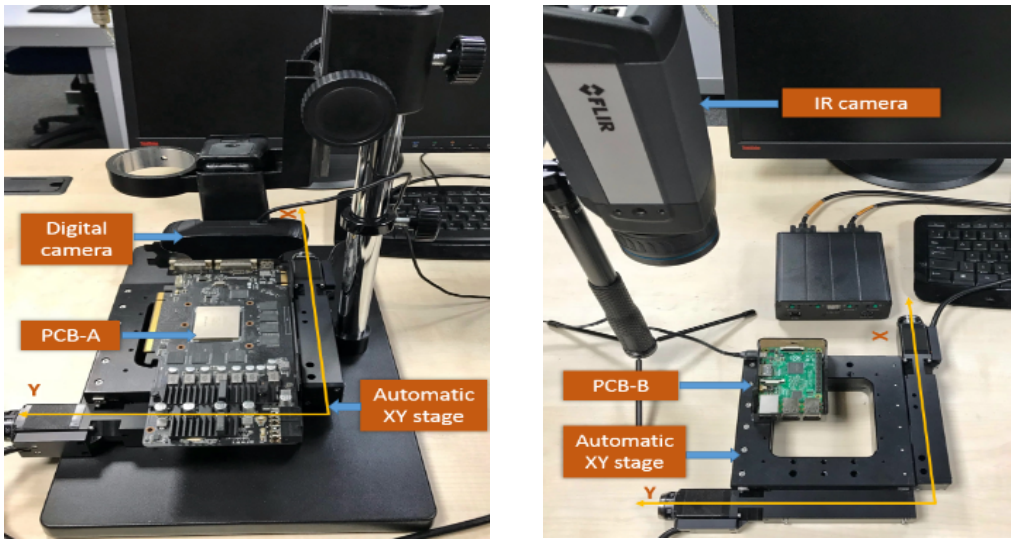

(a) (b)

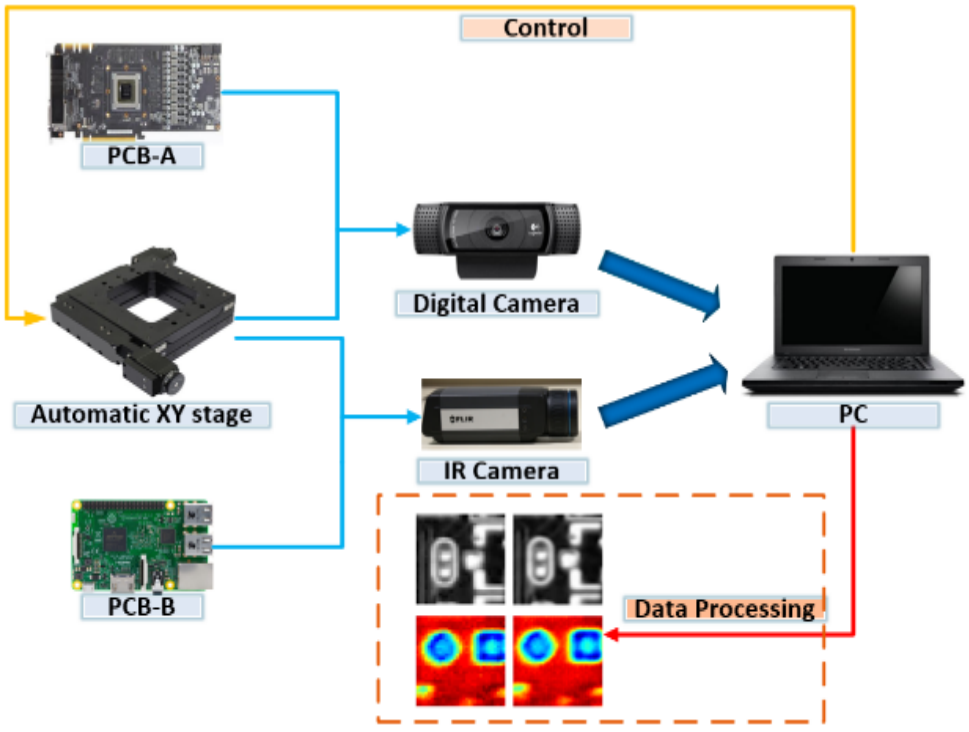

(c)

Figure 4-12 Experiment setup. (a) The experiment setup for Digital Camera; (b) The experiment set up for FLIR A655sc IR Camera; (c) The flow chart of the whole experiment.

B are fixed on the automatic XY movement stage for the digital camera and IR camera respectively. The minimum movement of the stage that could be achieved was 0.31 μm. PCB-A, as the target of the digital camera, is a computer graphics card and was inspected under room temperature without power-on. PCB-B is the Raspberry-pi and was inspected under power-on for more than half an hour to ensure the consistency of temperature during the data capture. The steady-state temperature of the PCB-B central region was 38.2-45.5 °C. The room temperature for both experiments was recorded at 22 °C and the relative humidity value was 55%.

There are two kinds of potential motion modes in these experiments. One is that the object is fixed and the camera is mounted on the automatic XY stage to enable motion. The other is that the camera is fixed and the object is mounted on the automatic XY stage. Both modes can introduce global sub-pixel motion, which is the key to increase the resolution of static objects. The second mode was used in this study.

The sub-pixel movement is established according to the required scale factor of the SR technique. Set a $(a > 1)$ as the scale factor, and for each data acquisition, the automatic XY stage moves a step of $1/a$ pixel either in the x or y-direction. Assuming the object position in the thermal image on the first data capture as the reference, denoted as (x_0, y_0), the camera is moved to ensure that the following positions of the object on the image are achieved:

$$\begin{cases} (x_0, y_0), \left(x_0 + \frac{1}{a}, y_0\right), \dots, \left(x_0 + \frac{a-1}{a}, y_0\right), \\ \left(x_0, y_0 + \frac{1}{a}\right), \left(x_0 + \frac{1}{a}, y_0 + \frac{1}{a}\right), \dots, \left(x_0 + \frac{a-1}{a}, y_0 + \frac{1}{a}\right), \\ \left(x_0, y_0 + \frac{a-1}{a}\right), \left(x_0 + \frac{1}{a}, y_0 + \frac{a-1}{a}\right), \dots, \left(x_0 + \frac{a-1}{a}, y_0 + \frac{a-1}{a}\right) \end{cases} \quad \vdots \quad (4\text{-}21)$$

It can be inferred from Eq. (4-21) that the total number of images to be captured is a^2.

The motion step in the translation stage depends on the camera's inherent parameters and the distance from the camera to the object surface. This study

uses a simple calibration process to achieve the parameter α, which indicates the required movement of the stage in the x or y direction to achieve a representative shift of one pixel in an image. In this study, one image was captured along the x-direction of the stage which represents a shift of 1 mm. The shift of the calibrator on the images is now measured and denoted as m pixels. Then α is written as

$$\alpha = 1/m \tag{4-22}$$

This step can then be repeated for the y-direction. In this research, the calibration step was conducted automatically.

In this study, a digital camera with a resolution of 640×480 pixels and an IR camera with a resolution of 640×480 pixels were selected for testing, as shown in Figure 4-12. In order to adjust the distance between the camera and the surface of the object to ensure a good field of view of the object, the working distance of the digital camera was set as 120 mm. The estimated α is 155μm, considering the minimum step size of the XY stage of 0.31μm. Therefore, the maximal scale factor that this device can achieve is 500. The working distance of the IR camera was set as 180 mm and the estimated α is calculated as 145 μm. The estimated maximal scale factor of the device can achieve is 467. It is worth noting that the maximum resolution scale factor of the device that can be achieved depends on the working distance, intrinsic parameters of the camera and step size of the stage. For both experiments, six sets of data were collected aiming to achieve the scale factor of 2, 4, 6, 8, 10 and 20. The resolutions of produced HR images are 1280 x 960, 2560 x 1920, 3840 x 2880, 5120 x 3840, 6400 x 4800 and 12800 x 9600 pixels respectively.

4.4.2.1 Performance Evaluation

No-Reference quality metrics were selected to quantitatively evaluate the improvement of image quality based on statistical features. Natural Image Quality Evaluator (NIQE) is a completely blind image quality analyser that only makes use of measurable deviations from statistical regularities observed in natural images, without training on human-rated distorted images, and indeed without

any exposure to distorted images [123]. It calculates the no-reference image quality score for images, and the smaller score indicates better perceptual quality.

Entropy is another quantitative measure of image quality. Information entropy is a quantitative measure of the information transmitted by the image. The image quality can be quantitatively compared when the transmitted information provided by the images are known [124]. From the physical measurement's point of view, the more information is transmitted, the bigger the Entropy score, the better the image quality is.

4.4.2.2 Result and Discussion

Experiment 1

Figure 4-13 displays a snapshot taken by the digital camera with a spatial resolution of 640 × 480 pixels. It can be seen that various electronic components

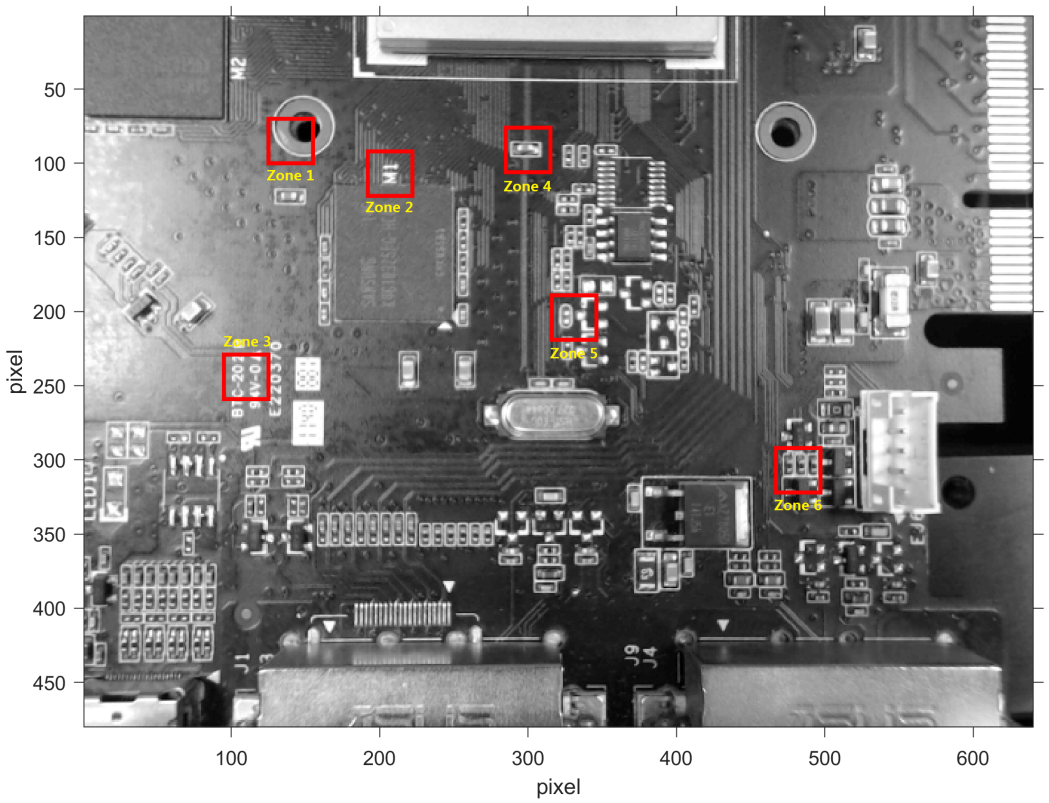

Figure 4-13 A digital image of the PCB-A, where ROIs are highlighted by rectangles.

are integrated on the PCB-A and digital identifiers are printed on its surface. For the scale factor 2, 4, 6, 8, 10 and 20, a total number of 4, 16, 36, 64, 100 and 400 images with this resolution were captured respectively. In order to better show the details of the improvement, six regions of interest (ROI) were highlighted with a size of 30 × 30 pixels in Figure 4-13. A comparison is made between the original image and the super-resolution image for each scale factor, as seen in Figure 4-14. It can be clearly observed that the proposed automatic controllable spatial resolution improvement technology significantly improved the sharpness of the edge in the selected RIOs. Figure 4-15 (left column) plots the measured Entropy and NIQE, representing the image quality, against different scale factors. It can be observed that as the scale factor increased, the details presented in the HR image became richer, but the trend was not linear. After the scale factor reached

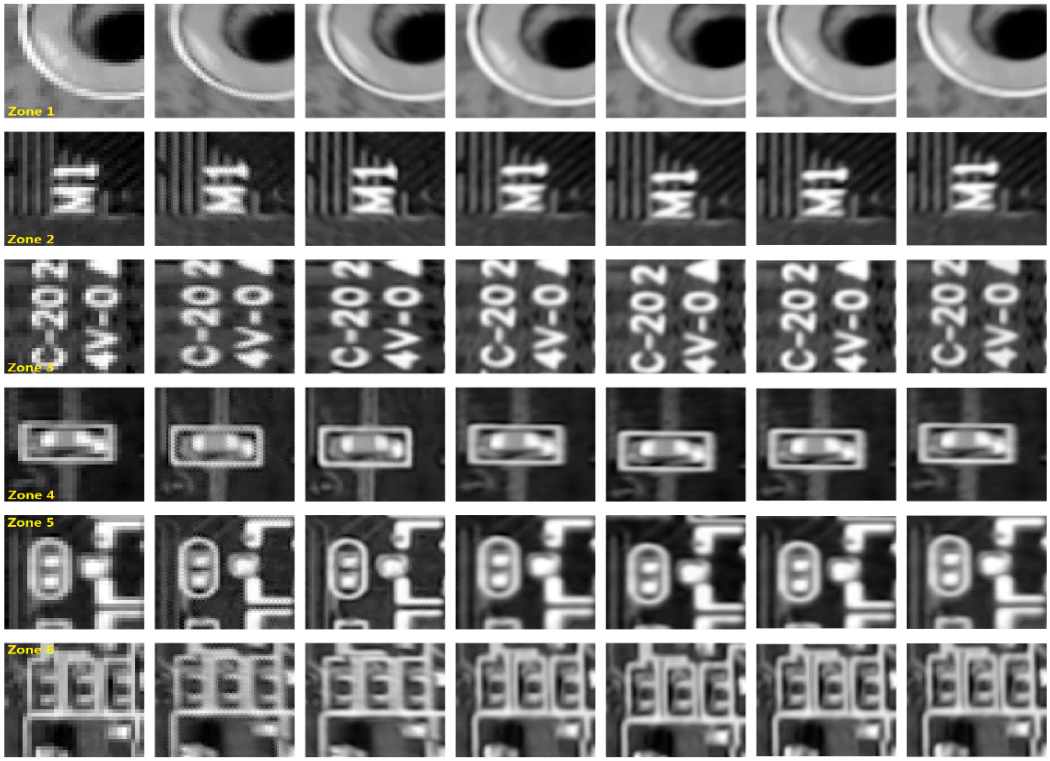

(a) raw image (b) 2x (c) 4x (d) 6x (e) 8x (f) 10x (g) 20x

Figure 4-14 Comparison of super-resolved high-resolution digital images for different scale factors.

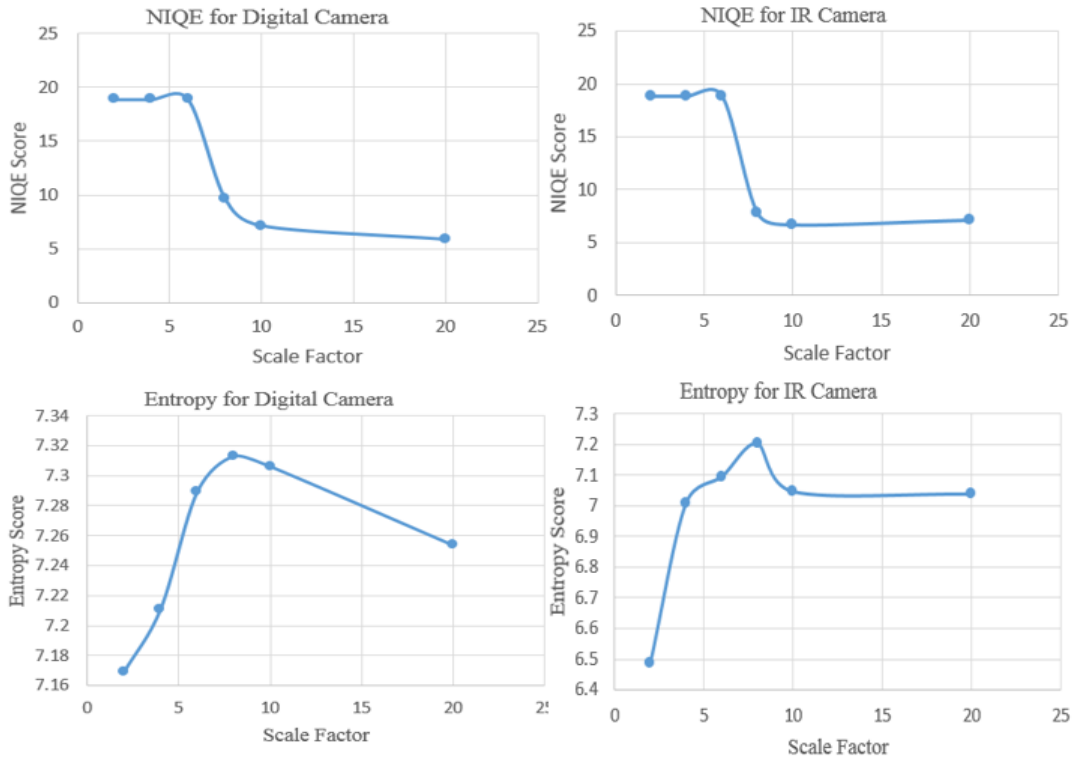

Figure 4-15 Results of quantitative evaluation for both experiments (left column: digital imaging; right column: thermal imaging)

8, the speed of image quality improvement was significantly slowed down. Meanwhile, it must be understood that the increase of the scale factor will increase the time cost of data collection and the computational cost of image reconstruction.

It should be noted that the performance of the techniques introduced is largely dependent on the accuracy of the motion. Figure 4-16 plots the comparison between the estimated motion (blue dot) using the employed image registration method and the ideal motion (red dot) for the six scale factors. It is shown that there are small absolute errors in both directions which may be due to inaccurate calibration of α. Furthermore, it can be observed that when the scale factor is large (> 10), the error becomes larger which may be caused by inaccurate control of the xy stage. Although theoretically, a higher scale factor should provide better

image quality, it is more difficult to control the movement among images which lead to a possibly even worse image quality.

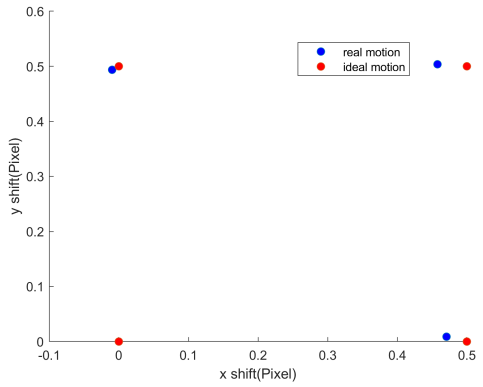

(a) 2X

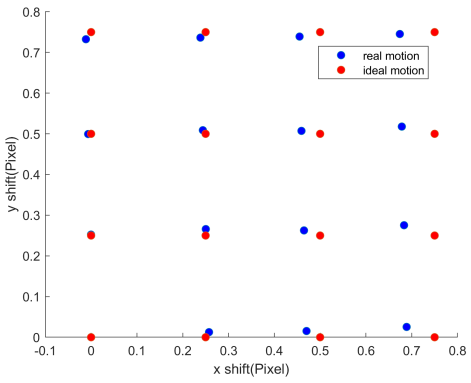

(b) 4X

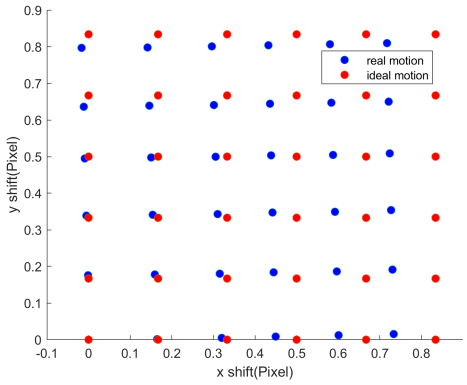

(c) 6X

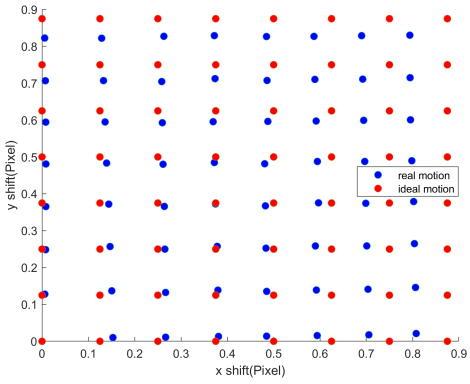

(d) 8X

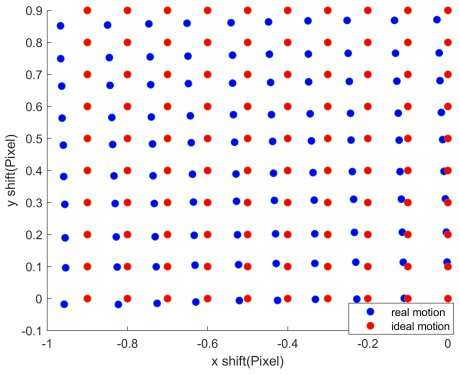

(e) 10X

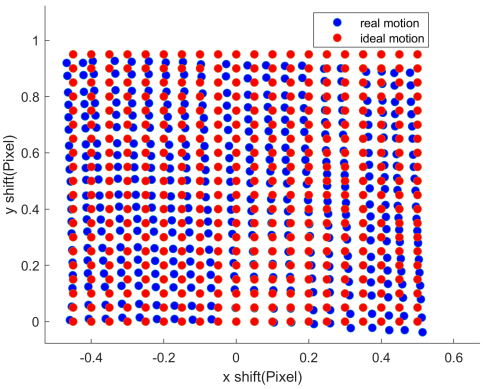

(f) 20X

Figure 4-16 Comparison of the measured motion in x and y directions among the digital images (blue dots) with the ideal motion (red dots).

Experiment 2

Figure 4-17 shows a snapshot of a thermal image captured using the IR camera FLIR A655sc with a spatial resolution of 640 x 480 pixels. The same as the previous experiment, the scale factors of 2, 4, 6, 8, 10, and 20 were tested. The size of the super-resolution results of the highlighted six regions of interest is 30 x 30 pixels, as illustrated in Figure 4-17. Figure 4-18 compares the raw image with the reconstructed high-resolution images for the tested scale factor. It can be observed that the sharpness of the thermal image on the edge greatly improved for all ROIs. There was no significant improvement observed for a scaling factor > 8. The measured Entropy and NIQE, representing the thermal image quality, against different scale factors are plotted in Figure 4-15 (right column). As the scale factor increased (a < 10), the image quality increased as expected, also was not in a linear manner. When the scale factor was larger than 8, the degree of image quality improvement significantly slowed down. This is clear evidence that there is a cap on image quality using this technique.

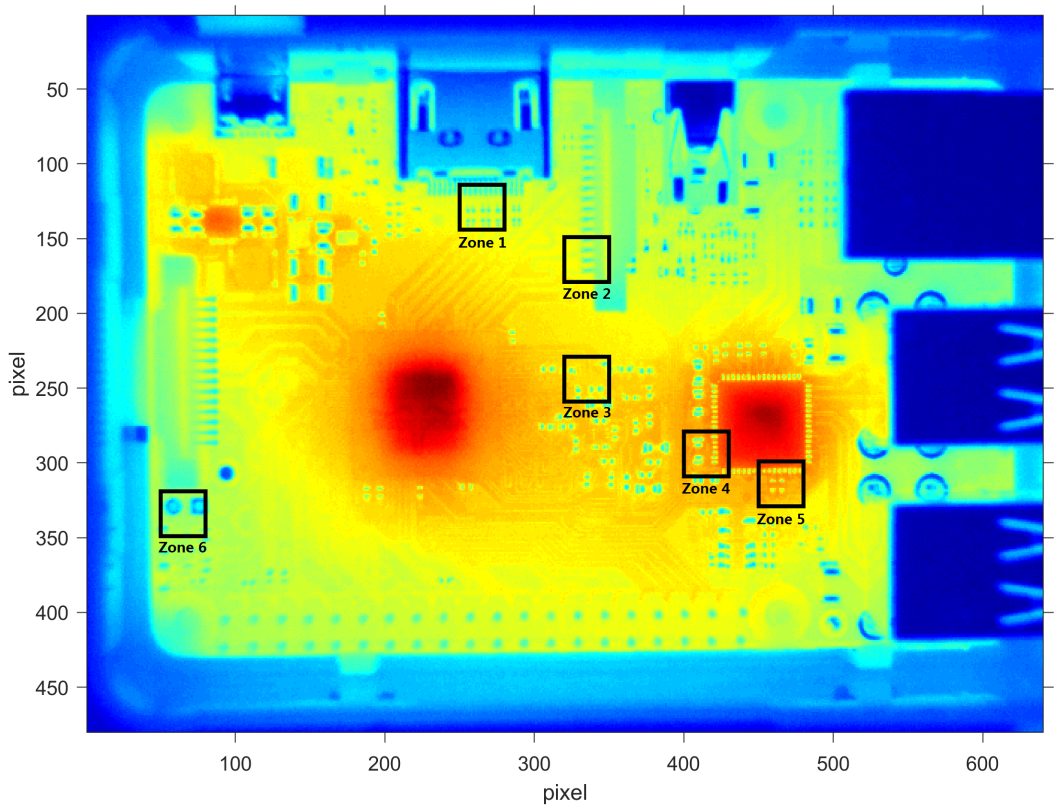

Figure 4-17 A thermal image of the PCB-B, where ROIs are highlighted by rectangles.

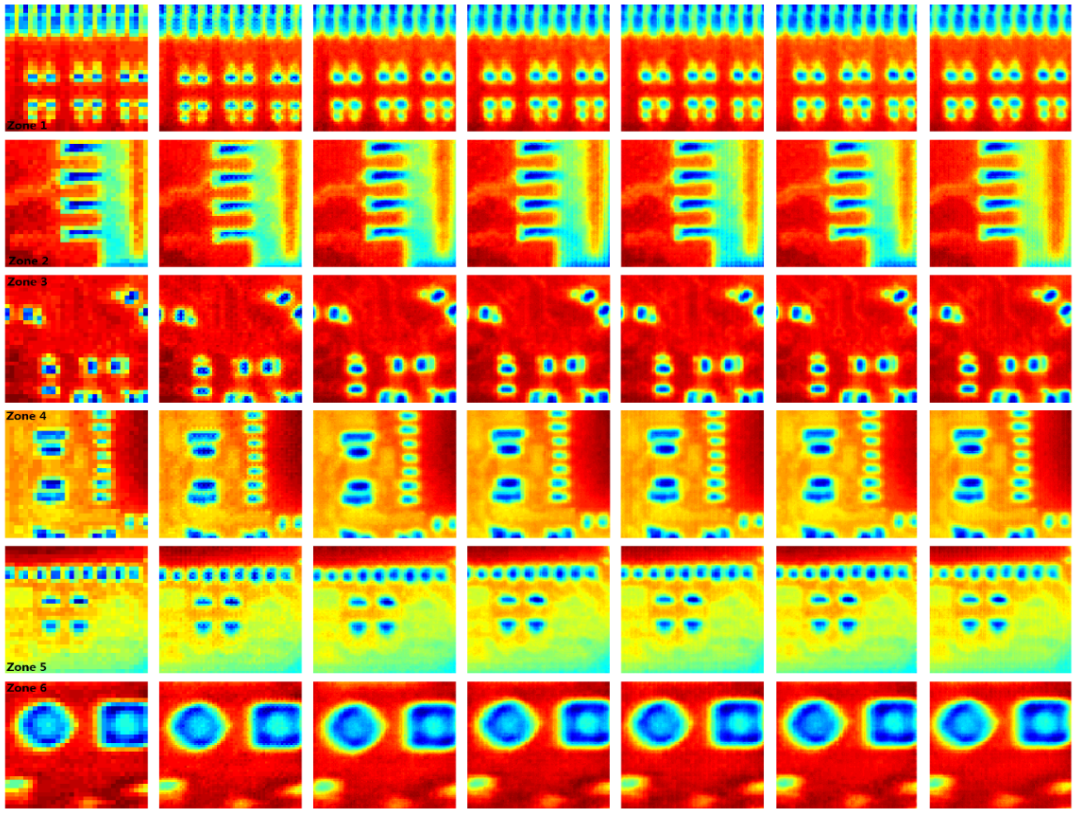

(a) raw image (b) 2x (c) 4x (d) 6x (e) 8x (f) 10x (g) 20x

Figure 4-18 Comparison of super-resolved high-resolution thermal images for different scale factors.

Figure 4-19 plots the comparison between the estimated motion (blue dot) using the employed image registration method and the ideal motion (red dot) for the six scale factors. Similar to the observation in the previous experiment, it is shown that the error becomes larger following the increment of the scale factor.

4.4.2.3 Conclusion

In this part, an automatic and controllable spatial resolution improvement technology has been proposed and tested on both digital imaging and thermal imaging, aiming to improve the accuracy and reliability of NDT. By accurately controlling the position between the sample and the camera, the shortcomings of poor stability and poor repeatability of the existing SR technologies are overcome. For experiments using both digital and infrared cameras, quantitative and

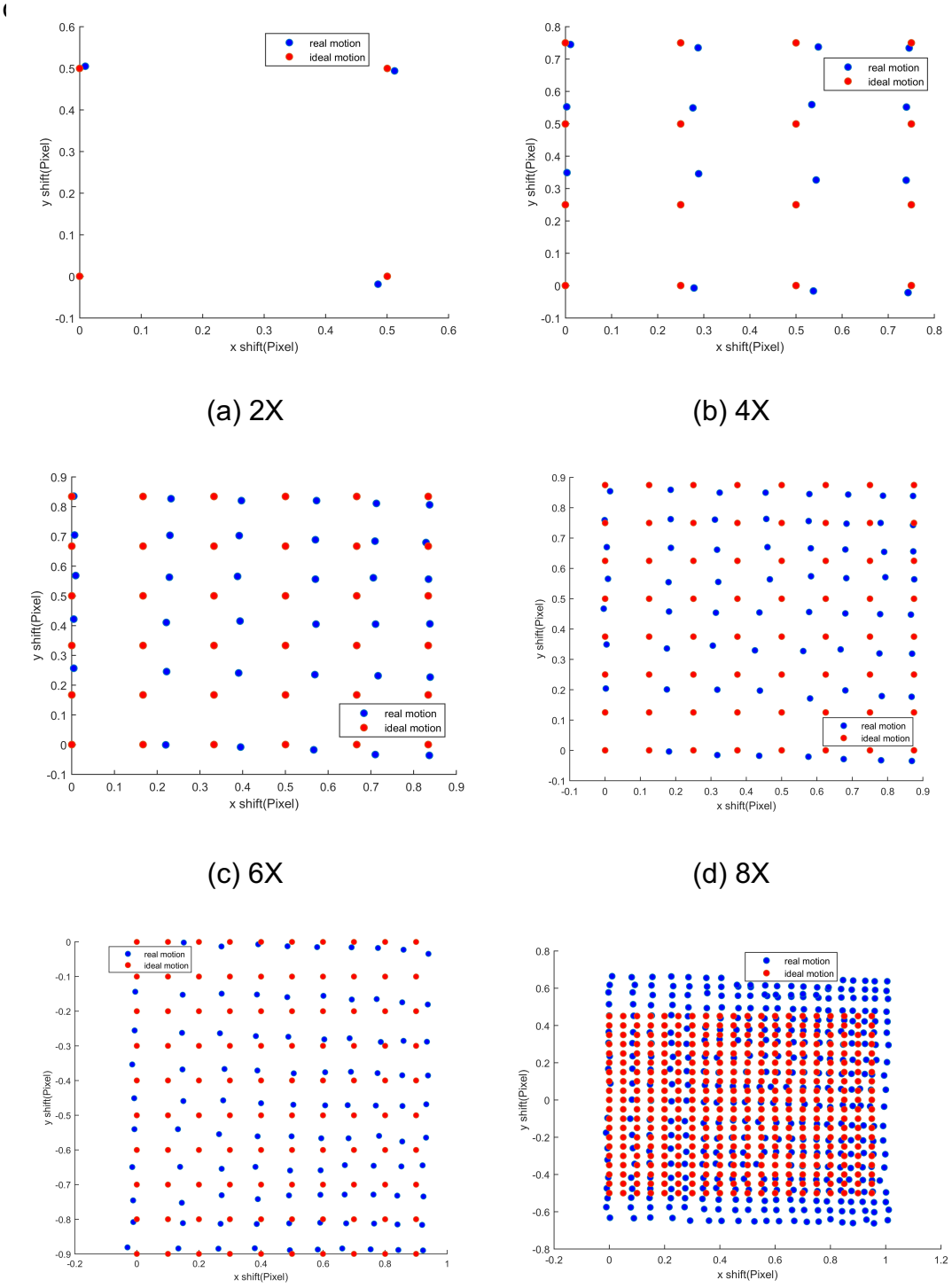

Figure 4-19 Comparison of the measured motion in x and y directions among the thermal images (blue dots) with the ideal motion (red dots).

spatial resolution of the acquired image by offering more details of edges. As evident by the NIQE value, the averaged image quality is improved from 18 to 6. The use of the automatic XY stage greatly reduced the time of data acquisition. Enhancing the capabilities of existing sensors by enhanced signal and image processing methods, and obtaining improved information about features, helped to increase confidence in degradation assessment. This technology is likely to be applied to active thermal imaging in the future, but this requires further research to confirm. With the further advancement of this research, the reduction of instrument cost and the improvement of measurement accuracy will create new environments and opportunities for the rapid development of the NDT technology.

4.5 Summary

A novel Spatial Resolution Enhancement for a Thermogram (SRE4T) system has been proposed to significantly improve the spatial resolution without upgrading the sensor. A high-resolution thermal image was reconstructed by fusing a sequence of low-resolution images with sub-pixel movements. To achieve the best image quality, instead of benefiting from the natural movements of existing studies, two systems containing the manual and automatic-controllable XY stage were used to produce a sequence of controlled sub-pixel movements. The performance of the proposed system was tested on both high-end and low-end thermal imagers. Both visual and quantitative results successfully demonstrated the considerable improvement of the quality of thermal images (up to 30.5% improvement of peak signal to noise ratio).

5 MINIATURISED ACTIVE THERMOGRAPHY (MAT) SYSTEM WITH INITIAL VALIDATION

5.1 Introduction

This chapter aims to propose a novel miniaturised active thermography (MAT) system, with its qualitative and quantitative performance evaluation of a variety of defects in composites using two types of excitation: flash and laser, respectively. The outline of this chapter is illustrated in Figure 5-1.

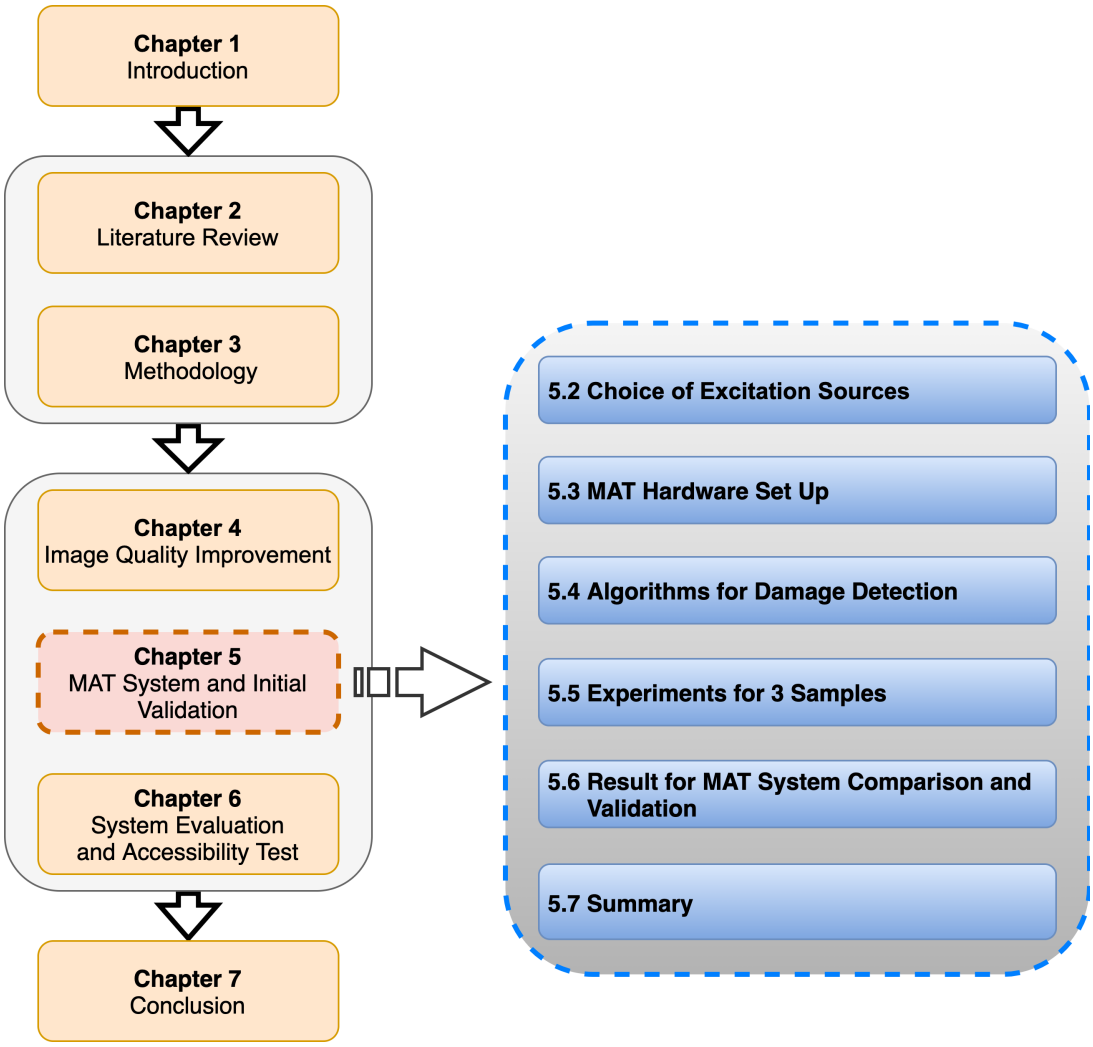

Figure 5-1 The outline of Chapter 5

The MAT system consists of a miniaturised commercial infrared (IR) sensor, FLIR Lepton, and an external excitation source (either flash lamp or laser), all of which

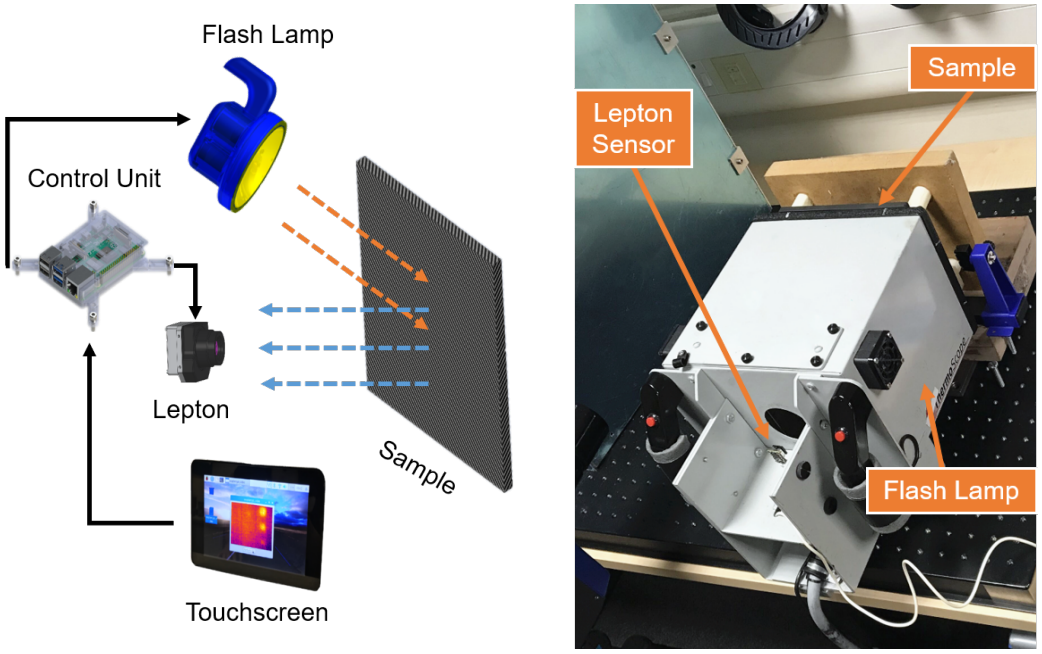

(a)

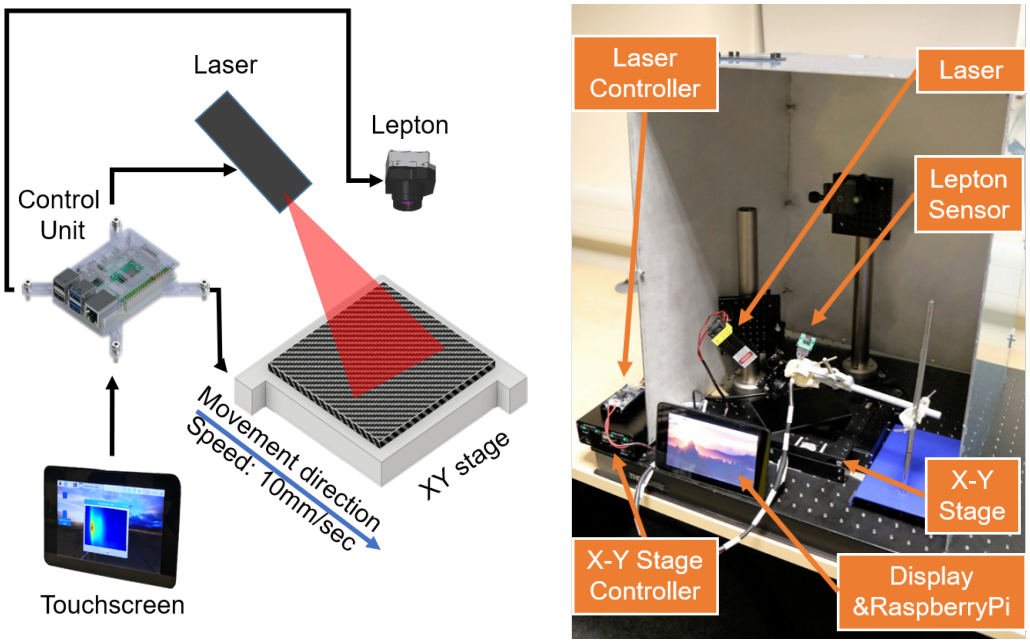

(b)

Figure 5-2 The two proposed miniaturised active thermography systems. (a) MAT system 1 (excitation source: flash lamp); (b) MAT system 2 (excitation source: laser) (Note: the system is a fully enclosed system and at the time of this image, the system was turned off.)

are integrated with a Raspberry Pi 3B+ along with a 7-inch touch screen (as shown in Figure 5-2). The system works under the reflective mode, where the sensor and excitation source are on the same side of the targeted component. Dedicated algorithms and corresponding software implementation were developed and integrated with the Raspberry Pi to capture, store and process the data. Though the computing capability is not as powerful as traditional PCs, the computational time is acceptable considering the relatively small size of the IR images and the low sample rate. The raw thermal images and results of the analysis can be visualised by a mini touch screen.

5.2 Choice of Excitation Sources

The flash has the advantages of covering a large excitation area with fast speed, but due to the factors such as irradiation distance and energy attenuation, the working distance should not be too far. Compared with the flash, the laser has advantages in energy density, intensity, accuracy, and ease in modulation [125]. It is an ideal excitation source for remote detection of delamination or cracks defects in composites. Compared with the Eddy current induction [126], the attenuation of the laser beam is very low, which leads to long-distance heating capacity and all these features support its application in a geometrically intricate environment.

5.3 Miniaturised Active Thermography (MAT) Hardware Set Up

The proposed MAT system accommodates two types of excitation source: optical flash (Figure 5-2(a)) and laser (Figure 5-2(b)). The compatibility of multiple excitation sources enables the flexibility to detect a variety of defects. Flash and laser are not combined but chosen separately according to the characteristics of their different excitation modes to increase the flexibility of the MAT system for detecting different types of defects. For example, the flash excitation is suitable for large-area defects such as delamination while the laser usually achieves good detection results for cracks or small damage. The pulsed MAT system is powered by two capacitor-bank-controlled xenon flash lamps assembled inside a box with internal reflectors with a nominal flash power output of 2KJ over a 250 x 200 mm

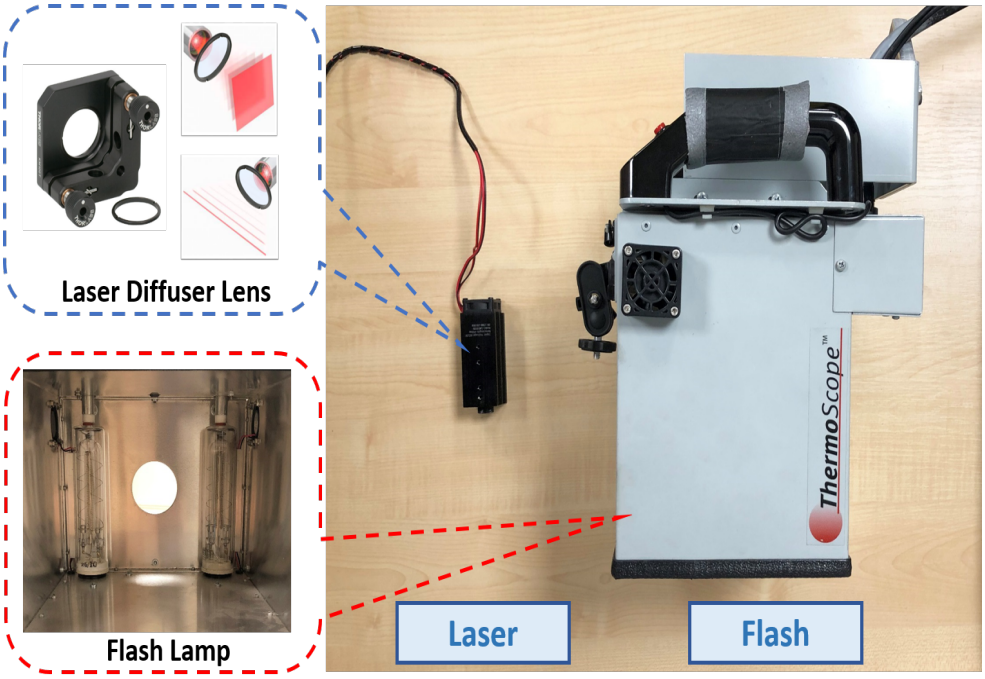

Figure 5-3 Comparison of the laser and flash excitation sources.

area (see Figure 5-3). The flash energy can be adjusted considering the adjustable working distance between 200 mm to 300 mm. The laser MAT system employs a low-cost semiconductor laser generator with a 450 nm wavelength, and a laser head dimension of 86×33×33 mm (see Figure 5-3). The small size, directionality and flexibility of laser pattern allows the proposed MAT system to work under geometrically intricate space. The 15 W laser beam is shaped to a line using an optical shaping lens (see Figure 5-3). Whilst the flash lamps provide superior inspection results both qualitatively and quantitatively, the ability to introduce such systems for in-accessible areas remains a challenge. The laser system, on the contrary, due to its compact design, non-attenuated energy exposure and the ability to reconstruct line-based data in real-time comes as an alternate technique that shows great potential for such intricate inspections.

5.4 Algorithms for Damage Detection

One objective of this study is to identify and develop appropriate quantitative evaluation algorithms for this MAT system, specifically considering the fact that the sensor has a significantly low SNR. Dedicated data analysis approaches for the MAT system to evaluate defects are proposed considering the degraded

signal quality. This section introduces a few methods for defect enhancement and depth measurement, for laser thermography and pulsed thermography respectively.

5.4.1 Pulsed Thermography

Based on the Fourier heat transfer law, the surface temperature due to a defect at depth *L* for a plate is given by [127]

$$T(t) = \frac{Q}{\sqrt{\pi\rho ckt}}\left[1 + 2\sum_{n=1}^{\infty} exp\left(-\frac{n^2L^2}{\alpha t}\right)\right] \tag{5-1}$$

where *T(t)* is the temperature variation of the surface at time *t*, *Q* is the pulse energy, *α* is the thermal diffusivity of the material, *ρ, c*, and *k* are the material density, specific heat capacity and thermal conductivity respectively.

For the pulsed MAT system, we propose to use the Logarithmic Second-Derivative method (LSD) [89] and the New Least-squares Fitting (NLSF) method [93] to estimate the defect depth. They are state-of-the-art of defect depth estimation. In LSD, the temperature decay curve is converted into the logarithmic domain, and then the curve is fitted with a polynomial model to reduce temporal noise and save storage space. This process is referred to as the Thermographic Signal Reconstruction (TSR) [89]. The peak of the second derivative of the TSR fitting is often used to estimate the defect depth. The polynomial model is written as

$$\ln\big(T(t)\big) \approx \sum_{n=0}^{N} a_n \big(\ln(t)\big)^n \tag{5-2}$$

where *N* is the order of the polynomial function (normally N is chosen between 6 to 8), and an are polynomial coefficients to be estimated. The first and second derivatives of TSR can also be used for defect enhancement [128] by providing higher defect contrasts. It can be computed by

$$\frac{d\ln\big(T(t)\big)}{d\ln(t)} \approx \sum_{n=1}^{N} a_n \cdot n \cdot \big(\ln(t)\big)^{n-1} \tag{5-3}$$

$$\frac{d^2\ln\big(T(t)\big)}{d^2\ln(t)} \approx \sum_{n=2}^{N} a_n \cdot n \cdot (n-1) \cdot \big(\ln(t)\big)^{n-2} \tag{5-4}$$

If the thermal diffusivity α is known, the depth of defect can then be estimated by

$$L = \sqrt{t_{LSD} \cdot \pi \cdot \alpha} \tag{5-5}$$

where t_{LSD} is the peak time of the second derivative.

The Least-Squares Fitting (LSF) method [92] uses a curve-fitting approach based on a 1-D heat transfer model to fit the raw temperature decay curve to identify the defect depth. The model is written as

$$T(t) \approx \frac{B}{\sqrt{t}}\left[1 + 2\sum_{n=1}^{\infty} exp\left(-\frac{n^2L^2}{\alpha t}\right)\right] - st \tag{5-6}$$

where L is the sample or the defect depth and B is a numerical value. This method has good resistance to noise, but it assumes a thermal wave reflection coefficient (R) of 1, which is not valid in most real situations. The NLSF method estimates the value of R directly from the observation data and has a higher accuracy of defect depth estimation [93]. The analytical model of NLSF is written as

$$\tilde{T}(t, A, W, R, t_s, s) = \frac{A}{\sqrt{t + t_s}}\left[1 + 2\sum_{n=1}^{M} R^n exp\left(-\frac{n^2W}{t + t_s}\right)\right] - s(t + t_s) \tag{5-7}$$

where $A=\frac{Q}{\sqrt{\pi\rho ck}}$, $W=\frac{L^2}{\alpha}$, t_s is the starting time of sampling, s is the slope, and M is a large iteration number. There are five parameters to be estimated including A, W, R, t_s, and s. A nonlinear least-squares solver in MATLAB (*lsqnonlin*) is applied to solve this five-parameter optimisation problem. The initial value of the parameter t_s is selected as zero and the lower and upper bounds are selected as -1 and 1 respectively because it is usually very close to zero. The initial value of R is selected as 1 and the lower and upper bounds are selected as 0 and 1 respectively. The selection of A depends on the energy applied on the inspection

surface, and the selection of W depends on the material and thickness of samples. The lower and upper bounds of W and A are usually selected as 5 times lower and 5 times higher than the initial values. The lower and upper bounds of s are selected as -50 and 50, and the initial value is chosen as 0. It should be noted that the computational time of this method depends on the selection of initial value and lower and upper bounds. Once the optimal parameters are estimated, if α is known, the defect depth can be estimated by

$$L = \sqrt{W \cdot \alpha} \tag{5-8}$$

5.4.2 Laser Thermography

This research proposes to use the Savitzky-Golay [94] filter, a digital smoothing filter, to increase the SNR of the low resolution and noisy IR images from Lepton. This is achieved by fitting successive time frames (or within a time window) with a pre-defined degree polynomial. As in the case of scattered signals, when the data points are equally spaced, an analytical solution can be derived in the form of a single set of convolution coefficients. The 1st and 2nd TSR derivatives of the filtered IR images can further reduce noise and enhance the true defect.

It should be noted that, in this study, the relative position between the laser and IR camera is fixed and the laser line is always on. In raw IR images, the intensity of the laser line is so high that the damage contrast is very low and sometimes the damage is almost undetectable. The 1st or 2nd derivative between two adjacent frames will remove the laser line and preserve the change between

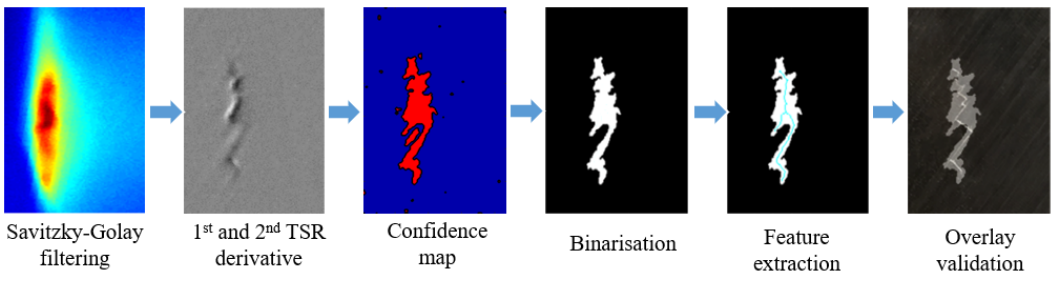

Figure 5-4 The proposed damage evaluation process for the laser MAT system.

these two images, by which means the contrast of defects/damage is significantly enhanced. The proposed process to evaluate damage using the laser MAT system is illustrated in Figure 5-4. Initially, the Savitzky-Golay filter [94] is applied to the raw data cube to reduce temporal noise for all pixels (Figure 5-4(a)). Then the process to calculate the 1st or 2nd TSR derivative using Eqs. (5-3)-(5-4) is followed to remove the interference of the laser line and further reduce the temporal noise (Figure 5-4(b)). A confidence map method [129] is applied to highlight the area with a significant difference from sound areas (Figure 5-4(c)), where the intensity of thermal images is transferred into the confidence level of the inspection. By selecting an appropriate threshold (95% confidence level is selected for this study), a binary image (Figure 5-4(d)) is produced to isolate the damage. A skeleton extraction method is then used to describe the morphological feature of the detected damage for easy quantitative comparison and validation based on the overlay with the binary image (Figure 5-4(e)) or the 1st or 2nd TSR derivative image (Figure 5-4(f)).

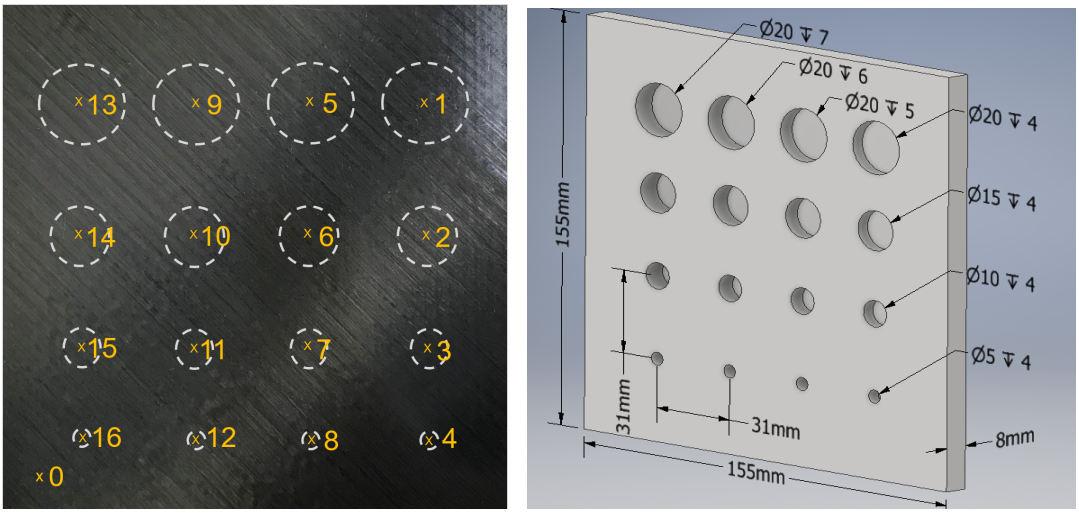

(a) Front side **(b) Back side (3D view)**

Figure 5-5 Illustration of Sample 1 (CFRP). (a) Dash circle indicates the dimensions and locations of defects on the backside. Point 1-16 mark different defects and Point 0 is sampled from a sound region (reference region) (b) Design dimensions of defects on the backside.

5.5 Experiments for 3 Samples

Three carbon fibre reinforced polymer laminates with a variety of defects are evaluated quantitatively and qualitatively using the proposed system by comparing them with two existing non-miniaturised systems.

5.5.1 Samples

This research employs three Carbon Fibre Reinforced Plastics (CFRP) laminates with different types of defect, marked as Sample 1, Sample 2 and Sample 3. All CFRP laminates were made by unidirectional Toray 800 carbon fibres pre-impregnated with Hexcel M21 epoxy resin. Sample 1 has a dimension of 155×155×8mm which contains 16 artificial flat-bottomed defects. The specification of Sample 1 and a snapshot are shown in Figure 5-5. Point 1-16 indicate different defects and Point 0 is sampled from the sound region (reference region). The defects are arranged in the 4 by 4 array layout, and the distance between the centres of two adjacent holes is 31 mm. As illustrated in Figure 5-4(b), the holes were drilled with four groups of diameters (5, 10, 15, and 20 mm) and four groups of thicknesses (7, 6, 5, and 4 mm), representing defect depths of 1, 2, 3, and 4 mm, from the top inspection surface. The defects in each row

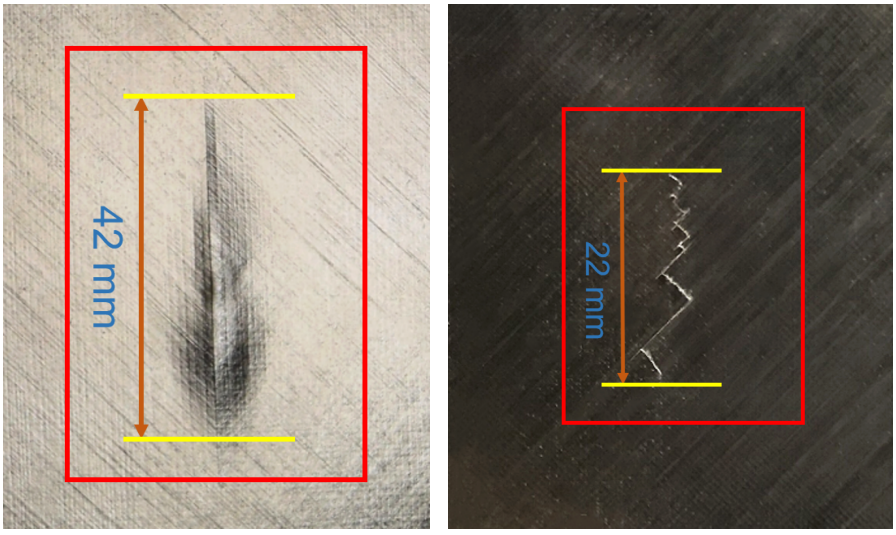

(a) Sample 2 (b) Sample 3

Figure 5-6 Illustration of the inspection surface of Sample 2 and 3, where delamination and crack are presented.

have the same diameter but different depths, while the holes in each column have different diameters but the same depth. This sample is used to qualitatively and quantitatively evaluate the performance of the pulsed MAT system with comparative studies being taken up with the classic pulsed thermographic inspection using the high-resolution FLIR SC7600 IR camera.

The dimension of Sample 2 and Sample 3 is 150×120×5mm, where impact damage is presented. Sample 2, shown in Figure 5-6(a), contains a 42 mm length compound damage that features both crack and delamination. Sample 3, shown in Figure 5-6(b), has a 22 mm "Zigzag" shaped crack. The inspection and evaluation of this type of complex damage are crucial to the life assessment and maintenance of composite structures [130]. These two samples were used to qualitatively evaluate the performance of the laser MAT system with the classic laser thermographic inspection using the high-resolution FLIR A655sc IR camera.

5.5.2 Experiments Plan

Two experiments were implemented for these three samples. For the comparison study, Experiment 1 was conducted on Sample 1 using the proposed MAT and SC7600 under the experimental setup shown in Figure 5-2(a). A flash excitation source was used to provide homogenous heating for the front side of Sample 1. The working distance from the two cameras to the sample surface is 250 mm. The flash energy applied to the sample was 2 kJ. The framerate of Lepton and SC7600 was set at 8.7 Hz and 10 Hz respectively. The whole inspection duration is 70 seconds, indicating 609 and 700 frames being captured, respectively.

Experiment 2 was conducted on Samples 2 and 3 using the proposed laser MAT, shown in Figure 5-2(b). The line laser beam was projected on the sample surface with a 45°angle. The laser energy is 15 W. The microbolometer based LWIR FLIR A655sc was used for comparison purposes. The framerate of Lepton and A655sc was set at 8.7 Hz and 25 Hz respectively. Lepton works at a 100 mm distance away from the sample surface while the working distance of A655sc is 200 mm. An automatic XY stage facilitated the movement of the sample at a speed of 10 mm/sec. The sample was fixed on the XY stage horizontally, keeping the IR lens perpendicular to the sample surface. During the process of testing, the positions

of the camera and laser head are fixed, while only the sample is moved using the XY stage. This setup aims to reduce the noise caused by the movement of the camera and the interference to the laser head.

5.6 Result for MAT System Comparison and Validation

5.6.1 Results of the Flash-based MAT System

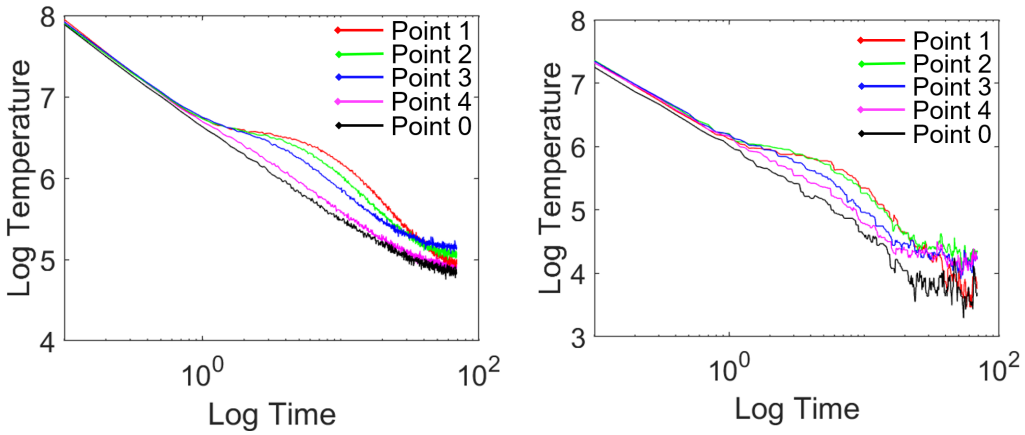

(a) SC7600---Point 1, 2, 3, 4 & 0

(c) MAT---Point 1, 2, 3, 4 & 0

(b) SC7600---Point 1, 5, 9 & 0

(d) MAT---Point 1, 5, 9 & 0

Figure 5-7 Comparison of the temperature-time decay profiles in the logarithmic domain of the selected defects.

Figure 5-7 plots the raw temperature-time decay curves in the logarithmic domain using the proposed MAT system and SC7600 system for the selected points. Figures 5-7(a) and (c) show the curves representing defects with the same depth but different sizes, as well as the reference. Figures 5-7(b) and (d) show the curves for defects of the same size at different depths. It can be observed from

the comparison that although SC7600 has better signal quality than the Lepton sensor, the MAT system can effectively capture the difference of decay curve among the selected defects and the reference for both groups. This observation

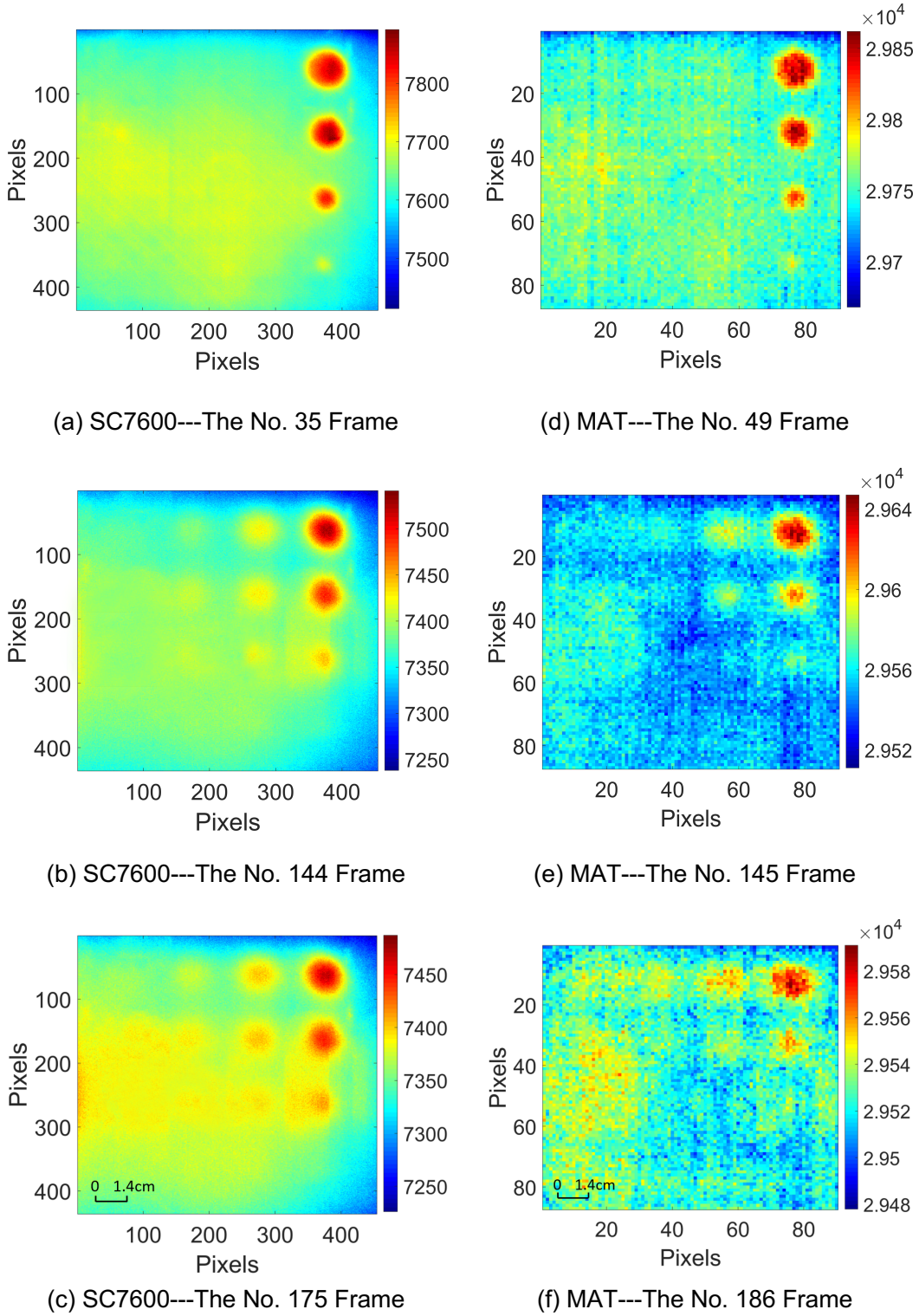

(a) SC7600---The No. 35 Frame

(d) MAT---The No. 49 Frame

(b) SC7600---The No. 144 Frame

(e) MAT---The No. 145 Frame

(c) SC7600---The No. 175 Frame

(f) MAT---The No. 186 Frame

Figure 5-8 The raw thermal images at different frames for Sample 1.

suggests that the proposed MAT system can detect the selected defects with reduced contrast.

Table 5-1 Visualisation of each defect using a local contrast colormap for the proposed system and sc7600

Defect	Radius (mm)	Depth (mm)	Radius/Depth ratio	SC7600		MAT	
1	10	1	10		✓		✓
2	7.5	1	7.5		✓		✓
3	5	1	5		✓		✓
4	2.5	1	2.5		✓		✓
5	10	2	5		✓		✓
6	7.5	2	3.75		✓		✓
7	5	2	2.5		✓		✓
8	2.5	2	1.25		✓		
9	10	3	3.33		✓		✓
10	7.5	3	2.5		✓		✓
11	5	3	1.67		✓		
12	2.5	3	0.83				
13	10	4	2.5				
14	7.5	4	1.88				
15	5	4	1.25				
16	2.5	4	0.63				

Due to the difference in defect size and depth, the maximal temperature contrast to sound areas for each defect appears at different times. Figures 5-8(a)-(c) show the 35th, 144th and 175th thermal images after the flash from SC7600 and Figures 5-8(d)-(f) show the 49th, 145th and 186th frames after the flash from the proposed MAT system. It should be noted that the framerate is different between the two systems and therefore the frame number showing the highest contrast is different. Results from both systems show that the defects with shallow depth, such as Defects 1-4, appear earlier. In addition, relatively sharp edges can be observed on the large defects, while the results of smaller ones have blurred edges. Not all defects can be detected due to a small radius/depth ratio for both systems [131]. It should be noted that Figure 5-8 uses a global colourmap and therefore the contrast of small or deep defects is not as sharp as that of the large and the shallow defects. To better evaluate the detectability, a region of 100×100 pixels for each defect is selected for SC7600 and a region of 25×25 pixels for each defect is selected for MAT for comparison and the results are tabulated in Table 5-1. The images presented in the table shows the highest contract frame of the first derivative of TSR using a local colourmap. The images from the MAT system are scaled up 4 times with a media filter which is applied for easier comparison. It can be observed that

- SC7600 can detect 11 defects including Defect 1, 2, 3, 4, 5, 6, 7, 8, 9, 10, 11 while MAT can detect 9 defects including Defect 1, 2, 3, 4, 5, 6, 7, 9, 10.
- For SC7600, the threshold of the detectable radius/depth ratio is 1.25 and the threshold of the detectable depth is 3mm. Defects 13 and 14 are not well represented even though the radius/depth ratio is over 1.25.
- For the proposed MAT system, the threshold of the detectable radius/depth ratio is 2.5 and the threshold of the detectable depth is 3mm.

To quantify the detectability of each defect, the SNR values, in our case constitutes to be the contrast-to-noise ratio, for all 16 defects were calculated for each frame using the following equation [132]

$$\mathrm{SNR(t)} = \frac{\overline{T_d(t)} - \overline{T_s(t)}}{\sigma(T_s(t))} \tag{5-9}$$

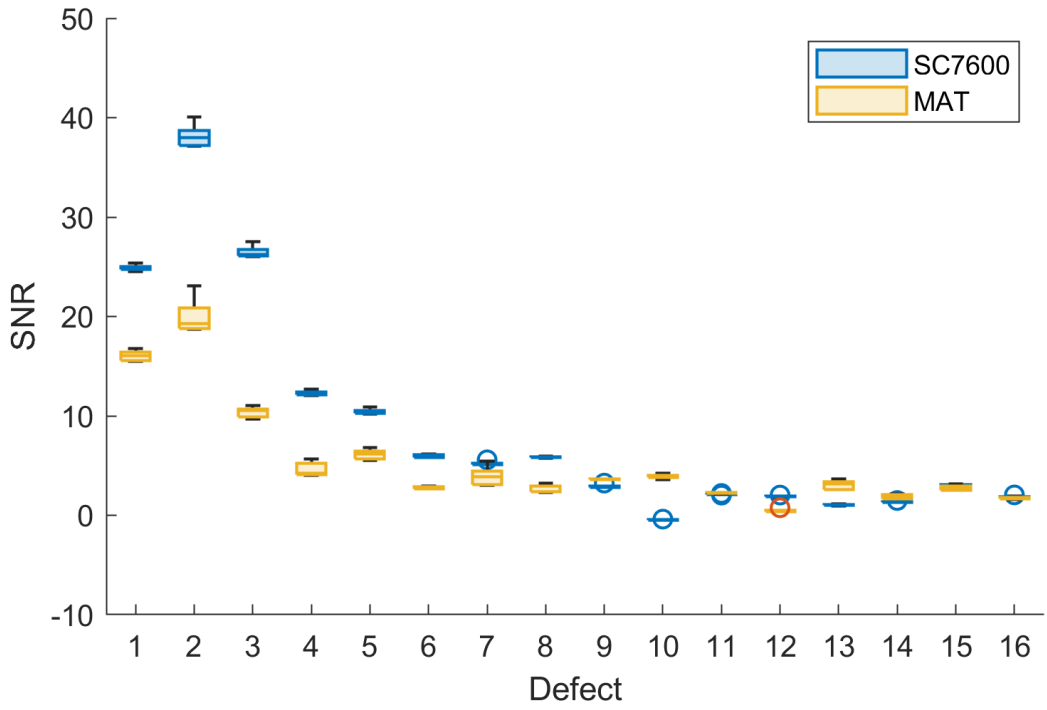

Figure 5-9 Comparison of SNR for SC7600 and MAT system for each defect.

where $\overline{T_d(t)}$ is the average temperature over a defect region (5×5 pixels for SC7600 and 3×3 pixels for MAT), $\overline{T_s(t)}$ is the average temperature over a sound region (20×20 pixels for SC7600 and 5×5 pixels for MAT). The SNR values for a total of 200 frames of each defect were calculated and the top 10% was selected to represent the detectability, the results of which are shown in Figure 5-9. As expected, the SNR values of SC7600 for most defects are consistently higher than the MAT system, representing superior detectability. For the defects with a large radius/depth ratio, such as Defect 1-5, the SNR for MAT is large than 5, indicating a good detectability. All the above observations suggest that although the detectability of MAT is compromised due to the low specification of temperature and spatial resolutions, MAT can be effectively used to detect defects in composites.

To further quantitatively evaluate the performance, Table 5-2 shows the estimated defect depths of the selected points using the LSD and NLSF methods for two systems. For the same defect, SC7600 measures the depth more

accurately (error up to 11%) than MAT (error up to 25%). In terms of two depth measurement methods, NLSF (average errors are 3.8% and 5.5% for two systems respectively) performs better than LSD (average errors are 6.2% and 14.3% for two systems respectively). It is observed that NLSF works particularly better than LSD for MAT where the noise level is high, which confirms the research finding in [93]. This is because NLSF is based on fitting a physical model while LSD is based on fitting a numerical model where the model can be easily over-fitted when the noise level is high. Although the high-resolution camera is superior to the MAT system in the overall depth measurement accuracy, there is no significant difference (e.g. max error 10% vs 11%) if the right method is chosen. Figure 5-10 plots a polygon map of depth measurement error using LSD and NLSF for Sample 1, which transfer from the results of Table 5-2. The blue colour plots the LSD method, while the red colour plots the NLSF method. The dashed

Table 5-2 The estimated depth and ground truth of the selected defects for Sample 1

Point No.			1	2	3	5	6
Ground Truth (mm)			1	1	1	2	2
SC7600	Estimated Depth (mm)	LSD	1.05	0.97	0.89	1.90	1.86
		Error	0.05	0.03	0.11	0.10	0.14
		%	5.0	3.0	11.0	5.0	7.0
		NLSF	1.01	0.98	0.90	2.09	1.97
		Error	0.01	0.02	0.10	0.09	0.03
		%	1.0	2.0	10.0	4.5	1.5
MAT	Estimated Depth (mm)	LSD	1.12	1.19	1.25	1.87	1.82
		Error	0.12	0.19	0.25	0.13	0.18
		%	12.0	19.0	25.0	6.5	9.0
		NLSF	1.05	0.98	0.89	2.10	2.09
		Error	0.05	0.02	0.11	0.10	0.09
		%	5.0	2.0	11.0	5.0	4.5

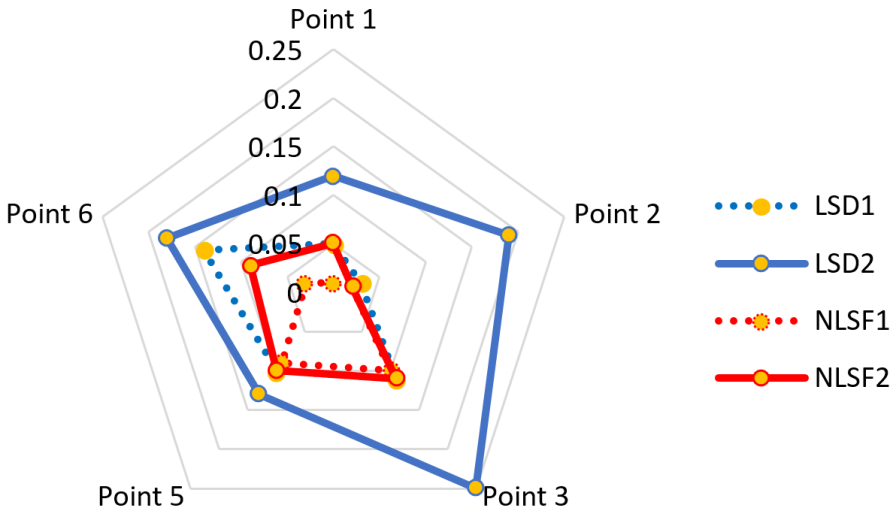

Figure 5-10 The error range of SC7600 and the MAT system using LSD and NLSF methods, where LSD1 and NLSF1 come from SC7600 (dash line), and LSD2 and NLSF2 come from MAT (solid line).

line is from SC7600 and the solid line is from the MAT system. It can be observed that although SC7600 with flash excitation overall performs better than pulsed MAT for both algorithms, the performance of NLSF based on MAT is even better than that of LSD with SC7600.

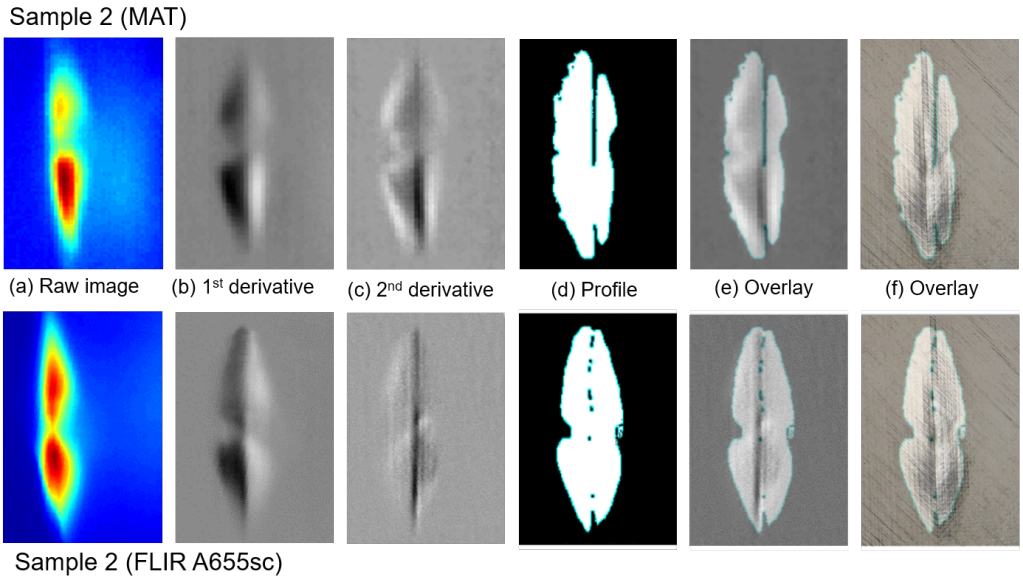

Figure 5-11 Damage visualisation using the laser MAT system (top row) and A655sc (bottom row) for Sample 2.

5.6.2 Results of the Laser-based MAT System

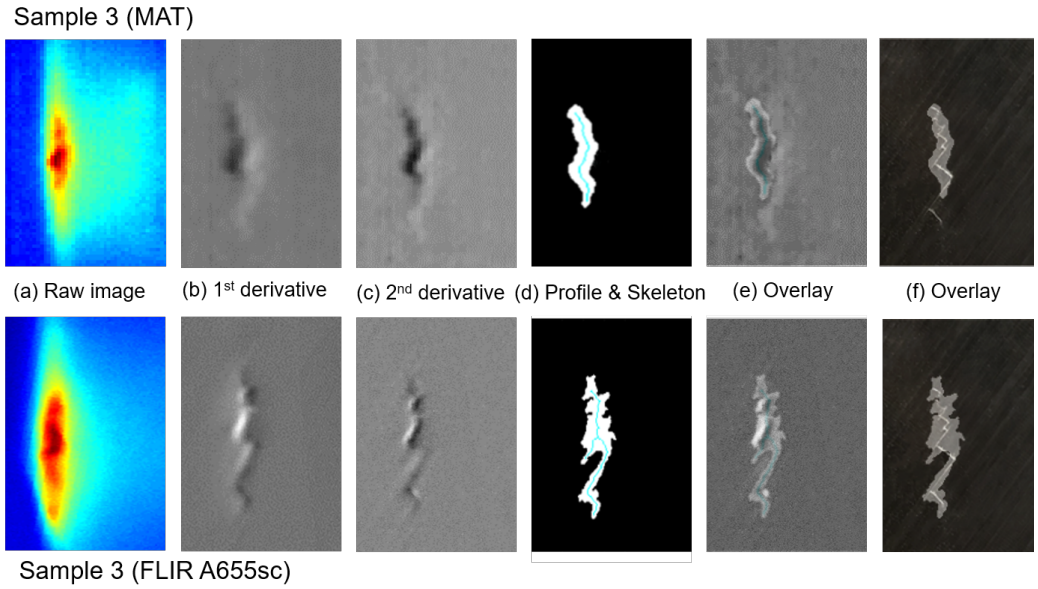

Figure 5-12 Damage visualisation using the laser MAT system (top row) and A655sc (bottom row) for Sample 3.

Figure 5-11 and 5-12 show the detection results for Sample 2 and 3 using the proposed MAT system and A655sc based on the laser excitation, where six visualisations are presented including raw images, the 1st derivative, 2nd derivative, extracted profile of the defect, the overlay of profile and the 2nd derivative image, and the overlay of profile and the digital surface image (from left to right). In the raw images, the laser beam overlaps with the damage which makes it a challenge to see the true damage profile. After applying the Savitzky-Golay smoothing filter, the 1st and 2nd TSR derivatives of the filtered IR images (see Figures 5-11 (b) and (c) graphs) improve the damage representation with a high-contrast contour, after the removal of the laser beam from the images. For Sample 2, a butterfly shape impact damage can be well observed in the 1st derivative image. The vertical crack, shown in Figure 5-6(a), can be observed in the 2nd derivative image. For Sample 3, the zigzag crack can be observed in both 1st and 2nd derivative images while the 2nd derivative image shows sharper edges.

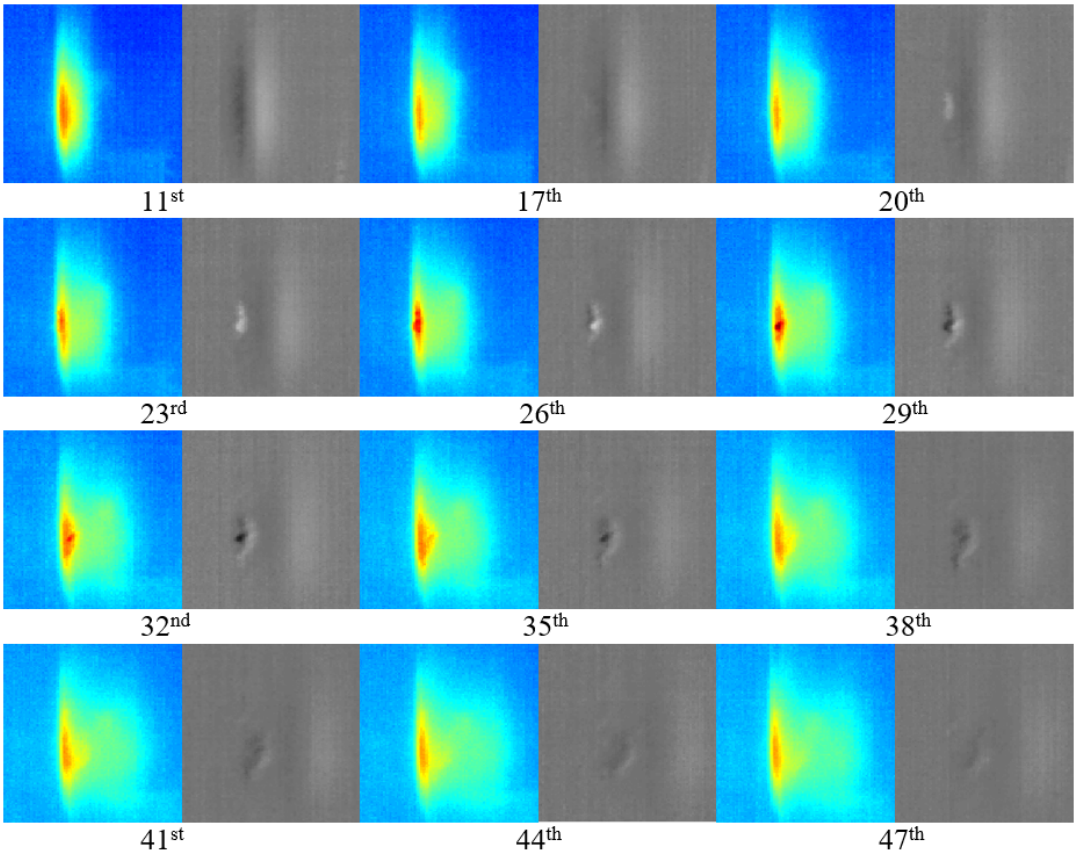

Figure 5-13 The raw thermal images (colour) and corresponding 2nd derivative (gray) for different frames during the scan of the proposed laser MAT system for Sample 3.

The results from the MAT system have less sharp boundaries than those from A655sc mainly due to the lower spatial resolution. However, it does not affect the determination of the type, profile and measurement of damage. In addition, the 2nd derivative is more appropriate to detect sharp damage (e.g. crack) and the 1st derivative is more appropriate to detect damage with a large area (e.g. delamination).

To further understand how to select the optimised frame to represent the defects of Sample 2 and 3, Figures 5-13 and 5-14 were produced to show the raw thermal image and corresponding visualisation of the detected defect at different frames. The first row shows three frames when the laser line is on the right of the defect, where the defect can barely be observed. The second row shows three frames when the laser line is overlapping with the defect, where a partial defect is visible.

The third row shows three frames when the laser line is on the left of the defect, which offer the optimised representation of the defect with high contrast. When the laser line passes the defect for a while, as shown in the fourth row, the contrast of the defect decreases.

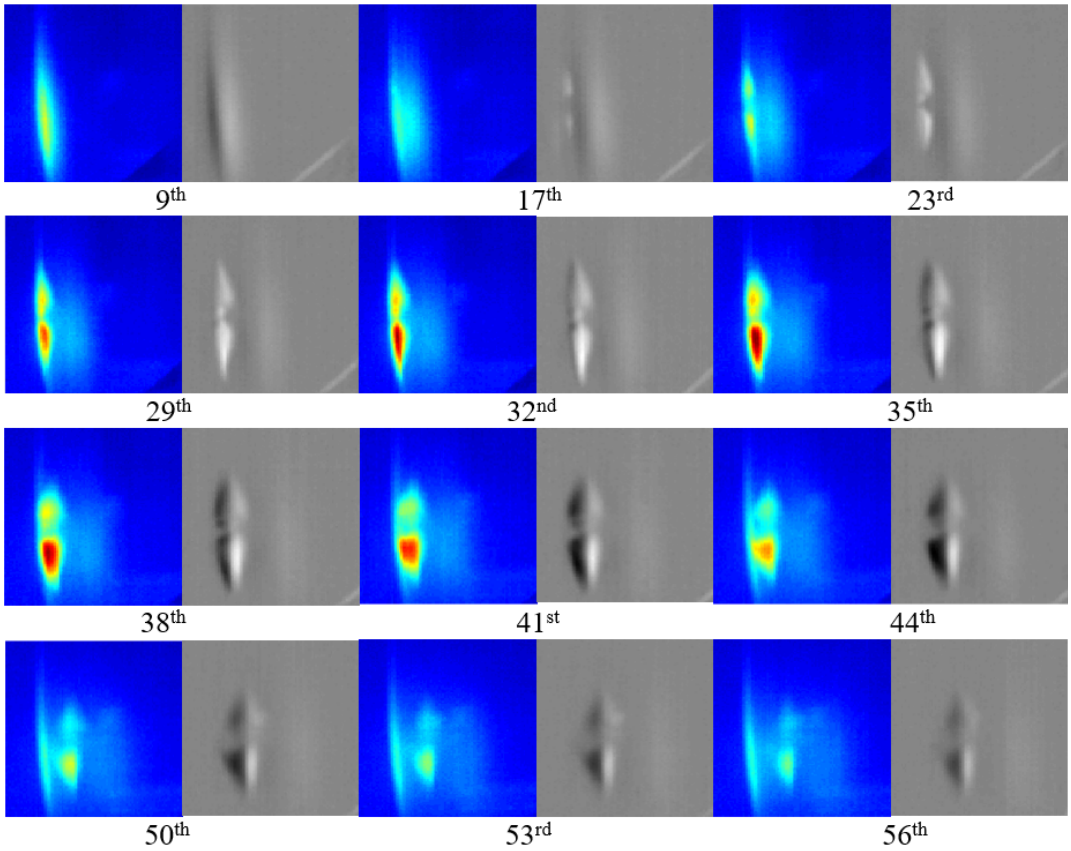

Figure 5-14 The raw thermal images (colour) and corresponding 1st derivative (gray) for different frames during the scan of the proposed laser MAT system for Sample 2.

All these observations demonstrate that the proposed laser MAT can effectively evaluate the impact damage of composite laminates, particularly for large delamination, the performance is similar to the classic laser thermography.

5.7 Summary

Aiming to improve the applicability and accessibility of active thermography and simultaneously reduce the cost of the inspection equipment, a novel MAT system including hardware integration and algorithm development was proposed in this

section with its qualitative and quantitative evaluation to detect defects and damage in composite laminates. Integrated with Raspberry Pi and two different exciting sources, the performance of the proposed MAT system has been evaluated to detect flat bottom holes, impact damage and crack in composite laminates, in comparison to existing systems with high-end infrared sensors. The results show that the proposed system can work with laser and flash effectively for degradation assessment although the detectability is compromised. Data pre-processing methods, such a TSR, Savitzky-Golay smoothing filter and media filter are strongly recommended for MAT to reduce temporal and spatial noise before quantitative analysis. For the laser-based MAT system, the 1st and 2nd derivative TSR images show improved performance in representing the damage than the raw images. The 1st derivative image is more appropriate for damage with a large size while the 2nd derivative image is more appropriate for damage with a sharp boundary.

One limitation of this system is that it has a sample rate of fewer than 10 fps, which limits its application to capture the thermal behaviour of materials with high thermal conductivity and diffusivity. The proposed system has a prominent price advantage and a significantly small volume. Its small and flexible body could better adapt to complex and geometrically intricate space in the industrial in-situ inspection.

6 SYSTEM EVALUATION ON COMPOSITE IMPACT DAMAGE SAMPLE, METAL SAMPLE AND ACCESSIBILITY

6.1 Introduction

This chapter introduces the evaluation test of the developed MAT system on CFRP samples with impact damage and metal samples with Flat-Bottom Hole. An accessibility test has been designed and conducted to evaluate the proposed system's performance to access geometrically intricate space. The outline of the chapter is illustrated in Figure 6-1.

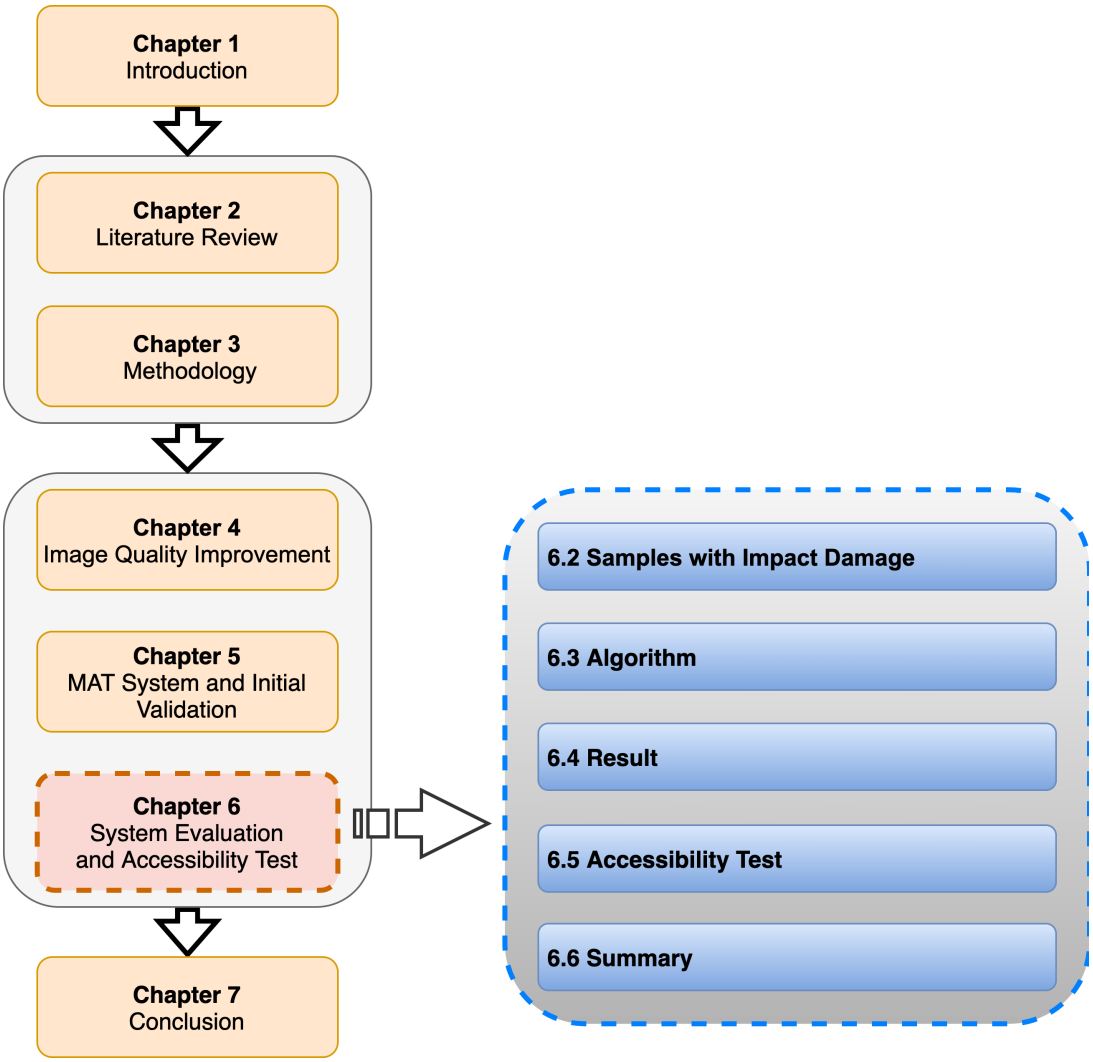

Figure 6-1 The outline of Chapter 6.

6.2 Samples with Impact Damage

Impact damage in composite laminates attracts great attention due to its significant degradation of structural integrity, but its detection is challenging due to its bare visibility and structural complexity, so-called barely visible impact damage (BVID) [133]. The testing specimens were produced with the dimension of 150 x 100 x 4 mm, which were made of unidirectional Toray 800 carbon fibres pre-impregnated with Hexcel M21 epoxy resin. As shown in Figure 6-2, a standard specimen is displayed and the area of the red box presents the areas with defects caused by the impact. The laminates were subjected to a drop test machine with predefined energy levels using a 16 mm (diameter), 2.281 kg hemispherical indenter, the impactor of the machine as shown in Figure 6-3. Impact energy was adjusted by changing the height of the drop-weight. The

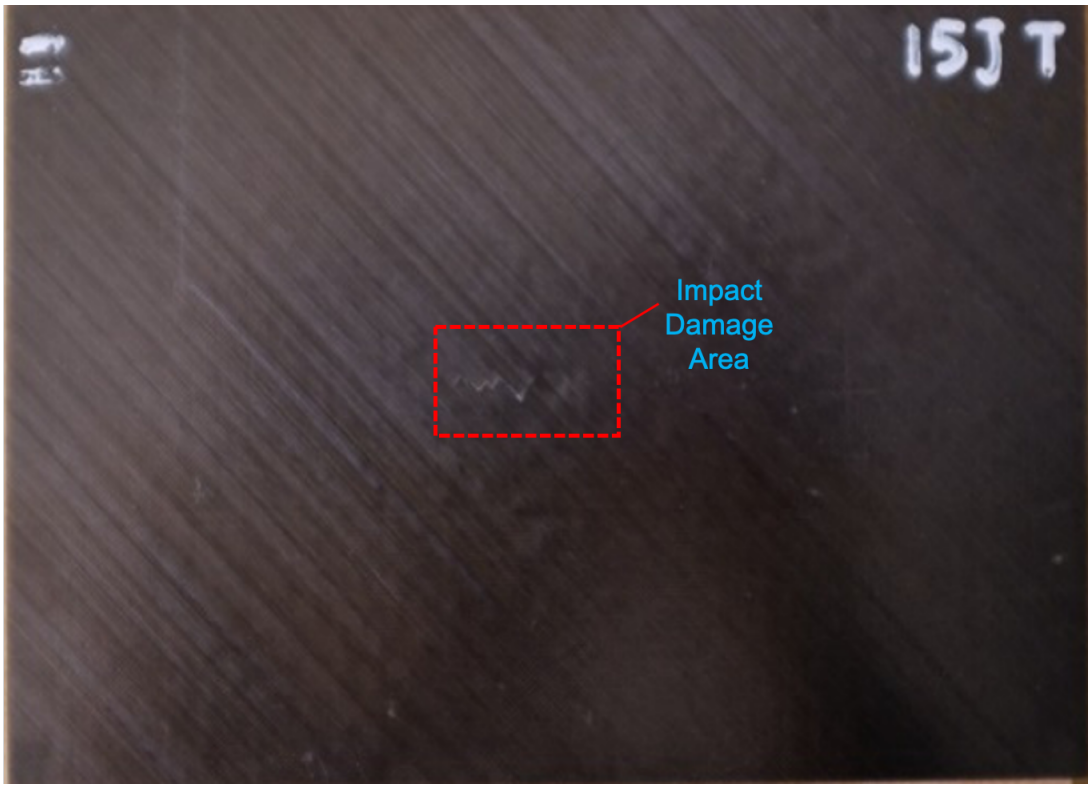

Figure 6-2 A standard specimen (impacted side).

Figure 6-3 Drop-weight tower.

specimens were subjected to represent impact energies of 5, 10, 15, 20, 25 and 30 J respectively. Figures 6-4 and 6-5 show the double sides of these five CFRP samples with impact damage subjected to different impact energies. The strike dents and damage with unpredictable directions are mixed and visible from the impacted side. But on the rear surface, the damage appearing as a form of combined damage with delamination overlapping with cracks are hidden or less obvious. Considering the thickness of the sample and its low thermal diffusivity, for SC7600, the sampling rate of 25 Hz was used, and a total of 1000 frames,

equivalent to 40 s data length, were captured and analysed; for the MAT system, the sampling rate was 8.7HZ, and total 350 frames, equivalent to 40 s data length.

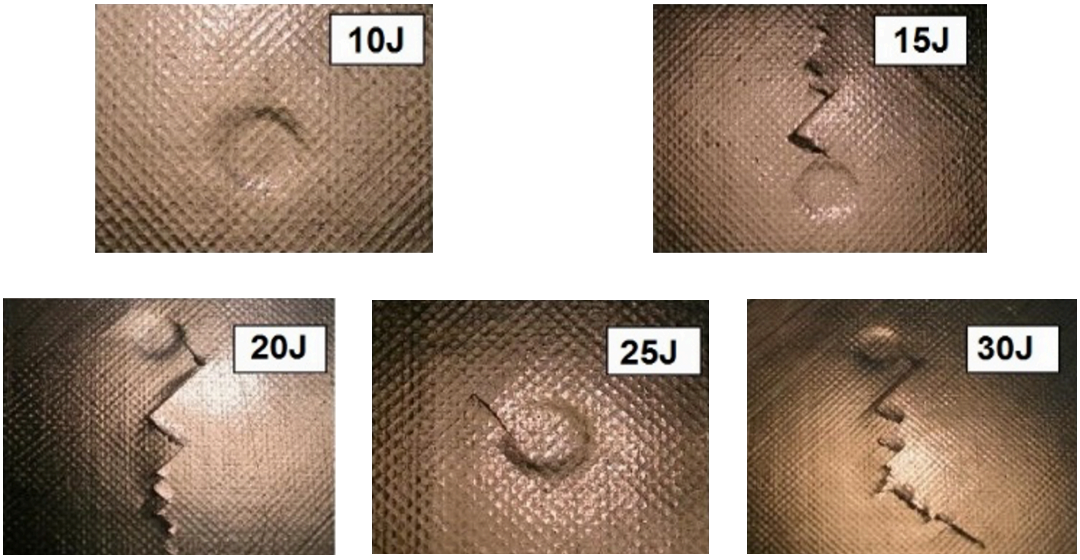

Figure 6-4 Visible impact damage from impacted side of the specimens.

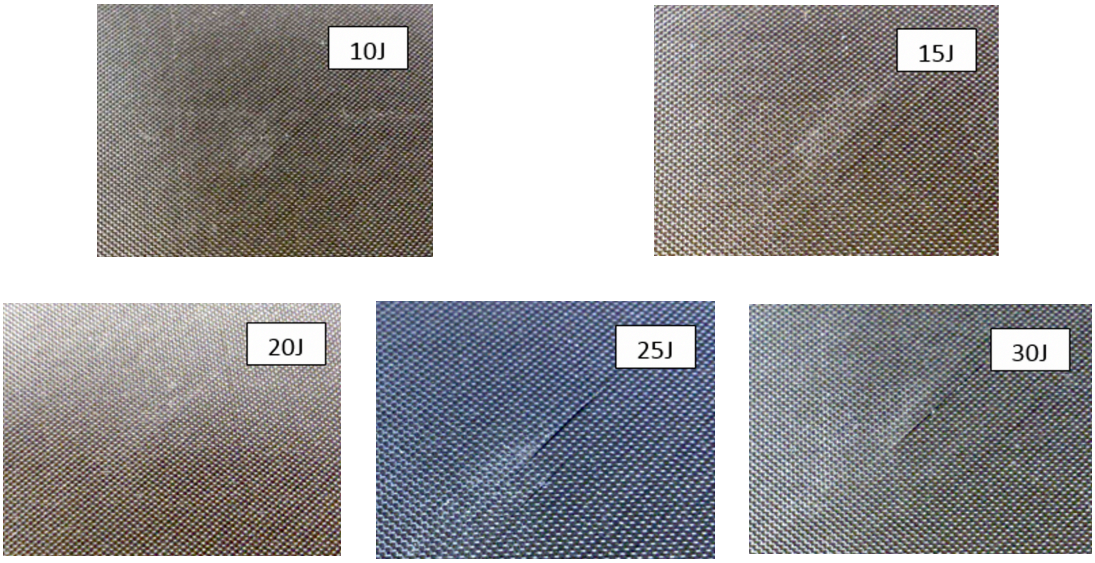

Figure 6-5 Invisible or unobvious impact damage from back side of the specimens.

6.3 Algorithm

The pulsed excitation source was used in the evaluation testing. Based on the Fourier heat transfer law, the surface temperature due to a defect at depth *L* for a plate is given by [127]

$$T(t) = \frac{Q}{\sqrt{\pi\rho ckt}}\left[1 + 2\sum_{n=1}^{\infty} exp\left(-\frac{n^2L^2}{\alpha t}\right)\right] \quad (6\text{-}1)$$

where *T(t)* is the temperature variation of the surface at time *t*, *Q* is the pulse energy, *α* is the thermal diffusivity of the material, *ρ, c*, and *k* are the material density, specific heat capacity, and thermal conductivity respectively.

To quantify the detectability of each defect under different impact energy, the SNR values, in our case constitutes to be the contrast-to-noise ratio, which for the defect was calculated for each frame using the following equation [132]

$$\mathrm{SNR(t)} = \frac{\overline{T_d(t)} - \overline{T_s(t)}}{\sigma(T_s(t))} \quad (6\text{-}2)$$

where $\overline{T_d(t)}$ is the average temperature over a defect region (5×5 pixels for SC7600 and 3×3 pixels for MAT), $\overline{T_s(t)}$ is the average temperature over a sound region (20×20 pixels for SC7600 and 5×5 pixels for MAT).

6.4 Result

The maximal temperature contrast to sound areas for each defect appears at different times due to the difference in defect size and depth. Figure 6-6 displays the thermal image of the sample with 10J impact. Figures 6-6(a)-(c) show the 2nd (0.23s), 8th (0.92s), and 14th (1.6s) thermal images after the flash from the proposed MAT system and Figures 6-6(d)-(f) show the 2nd (0.08s), 20th (0.8s) and 38th (1.52s) frames after the flash from SC7600. It should be noted that the framerate is different between the two systems and therefore the frame number showing the highest contrast is different. The results of detected defects of the other 4 samples (samples with 30J, 25J, 20J, and 15J impact energy) are shown in Figures 6-7, 6-8, 6-9, and 6-10. The lower the induced impact energy, the smaller the damage is. As expected, the crack length and delamination area

increase with the impact energy (see from Figure 6-6 to 6-10), and the proposed system and high-end IR camera can both capture the damage, while the edge of defect from the MAT system (see from Figure 6-10(a)(b)(c)) is less clear than that from SC7600 (see from Figure6-10(d)(e)(f)). Meanwhile, the SNR values for a total of 200 frames of each defect were calculated and the top 10% was selected to represent the detectability. The results are shown in Figure 6-11. As expected, the SNR values of the SC7600 for defects are consistently higher than those of the MAT system, representing superior detectability. However, all SNR for the MAT under different impact energy is larger than 15 dB, even up to 45 dB at 30J impact energy, indicating a good level of detectability. All the above observations suggest that although the detectability of MAT is compromised due to the low specification of temperature and spatial resolutions, the MAT can be effectively used to detect defects in composites.

The metal sample has a dimension of 145×132×6mm which contains 11 artificial flat-bottomed defects. The specification of this sample and a snapshot can be seen in Figure 6-12, where Point 1-11 indicate different defects and Point 0 is sampled from the sound region. As illustrated in Figure 6-12(b), the holes were back-drilled with seven diameters (1.5, 2.5, 3.5, 4.5, 7.5, 15, and 20mm) and one thickness (4.5 mm), representing a defect depth of 1.5mm, from the surface.

To illustrate the detectability of defects with different depths, the maximal temperature contrast appearing at different times is analysed. Figure 6-13(a) shows the 12^{th} (0.24s) thermal images after the flash from SC7600 using 50HZ frame rate, and Figure 6-12(b) shows the 4^{th} (0.46s) frame after the flash from the proposed MAT system using 8.7HZ frame rate. Due to the high thermal conductivity and diffusivity of metal, the optimal frame for displaying defects appears earlier than composite materials. The defects with shallow surface depth appear earlier. In addition, relatively sharp edges can be observed on the biggest defects, while the results of smaller ones have blurred edges. It can be observed that not all defects can be detected. SC7600 can detect 6 defects representing Point 1, 2, 3, 4, 5, 6, while the proposed MAT system can inspect only 1 defect representing Point 1. Two reasons lead to this result: (a) the low-resolution leads

to the decrease of the detectability of the MAT system, and the small defects are not easily detected; (b) the low frame rate leads to the incomplete capture for the

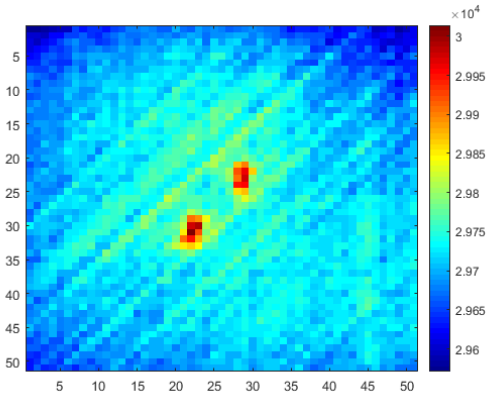

(a) MAT - 10J - 2nd Frame

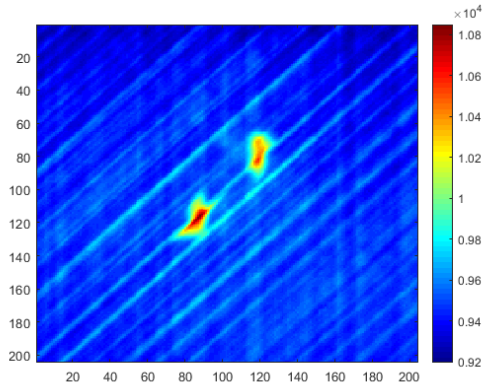

(d) SC7600 - 10J - 2nd Frame

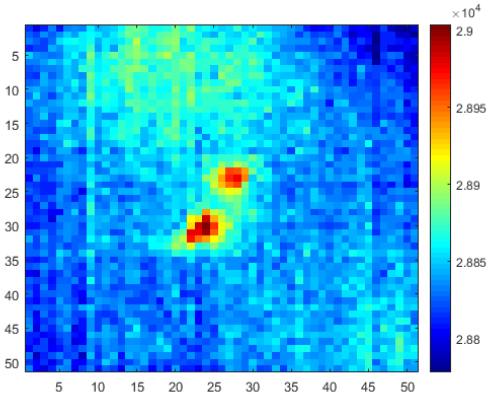

(b) MAT - 10J - 8th Frame

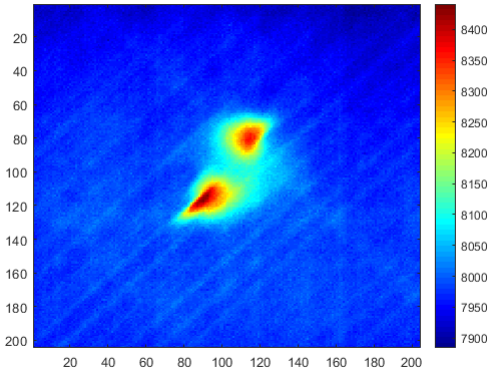

(e) SC7600 - 10J - 20th Frame

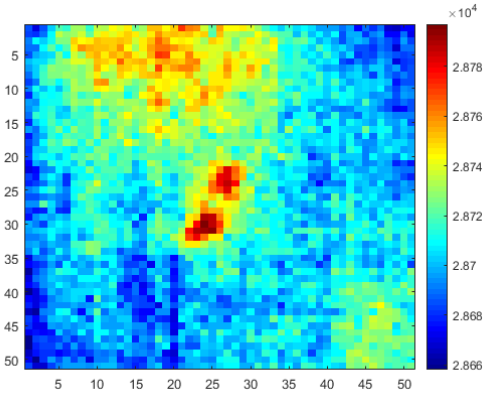

(c) MAT - 10J - 14th Frame

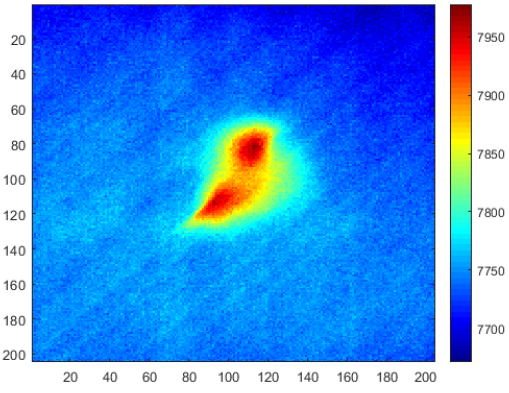

(f) SC7600 - 10J - 38th Frame

Figure 6-6 The raw thermal images at different times after the flash for the 10J sample.

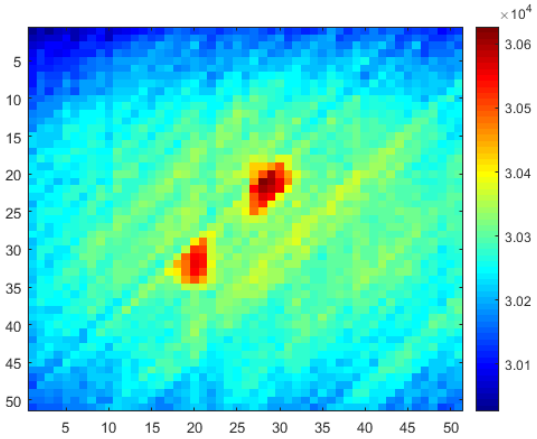

(a) MAT - 15J - 2nd Frame

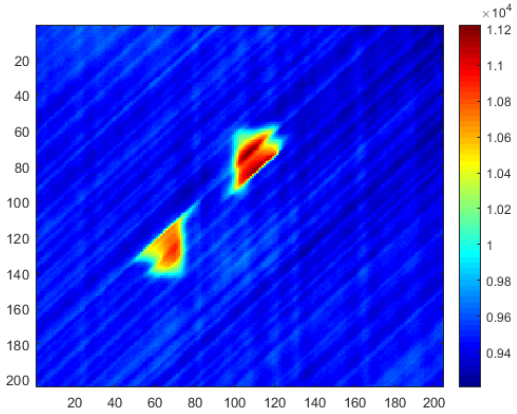

(d) SC7600 - 15J - 2nd Frame

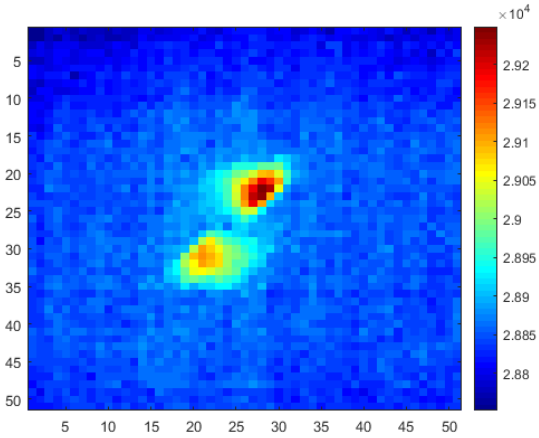

(b) MAT - 15J - 8th Frame

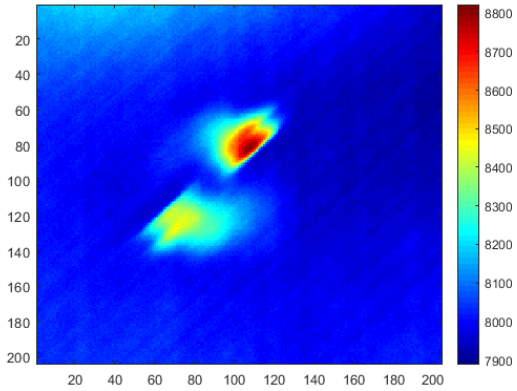

(e) SC7600 - 15J - 20th Frame

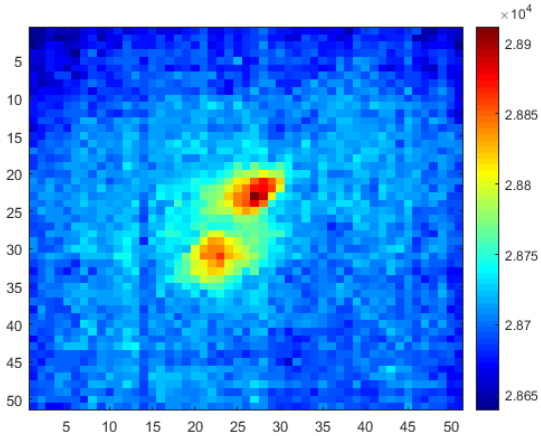

(c) MAT - 15J - 14th Frame

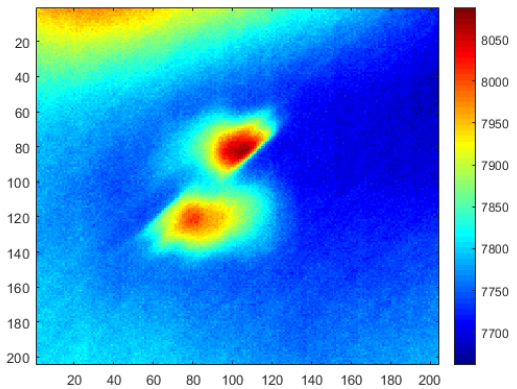

(f) SC7600 - 15J - 38th Frame

Figure 6-7 The raw thermal images at different times after the flash for the 15J sample.

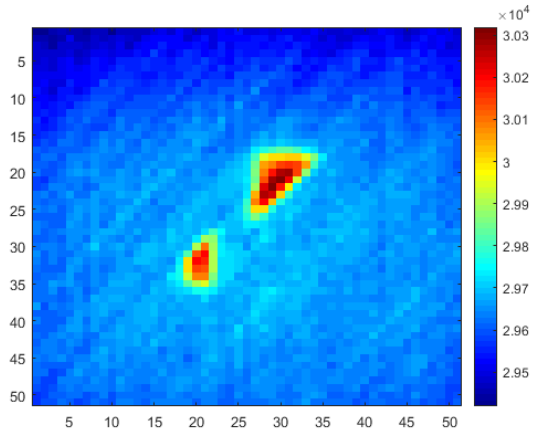

(a) MAT - 20J - 2nd Frame

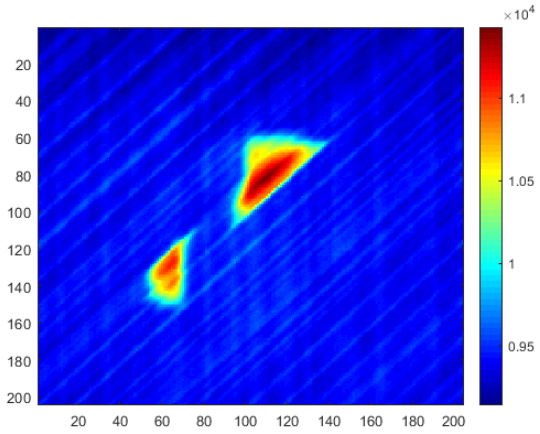

(d) SC7600 - 20J - 2nd Frame

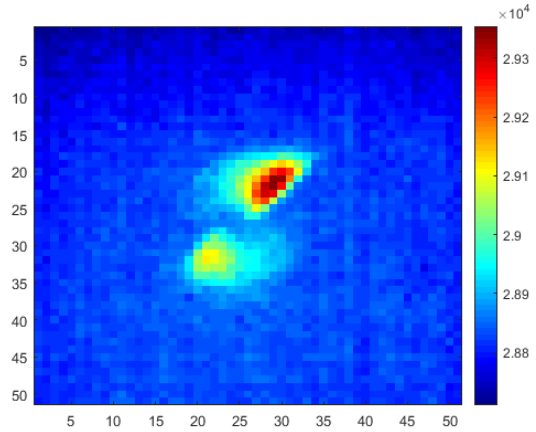

(b) MAT - 20J - 8th Frame

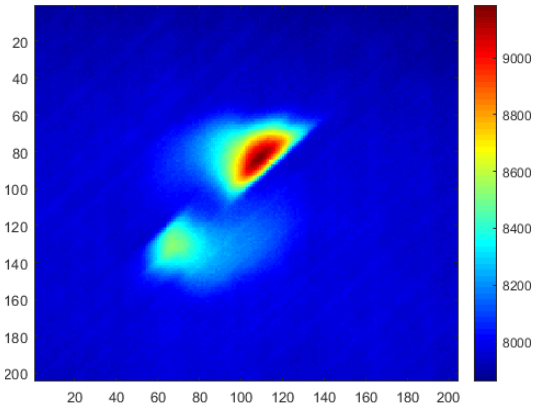

(e) SC7600 - 20J - 20th Frame

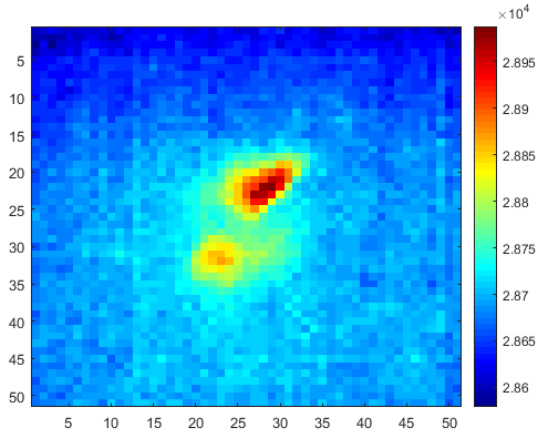

(c) MAT - 20J - 14th Frame

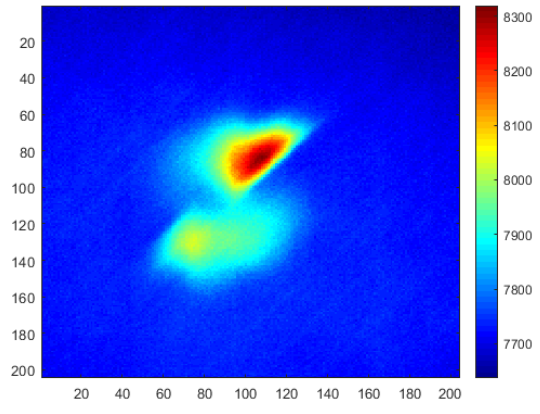

(f) SC7600 - 20J - 38th Frame

Figure 6-8 The raw thermal images at different times after the flash for the 20J sample.

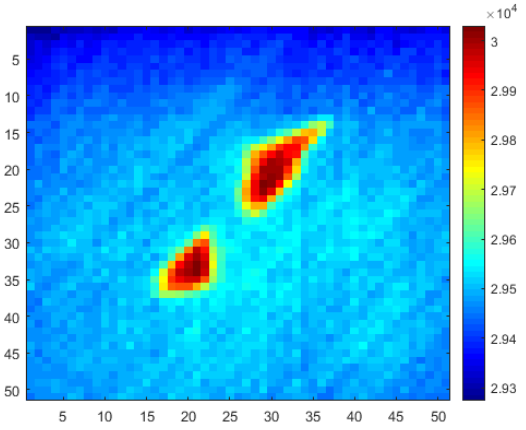

(a) MAT - 25J - 2nd Frame

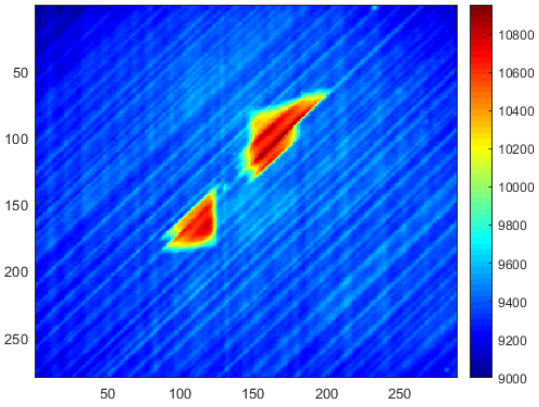

(d) SC7600 - 25J - 2nd Frame

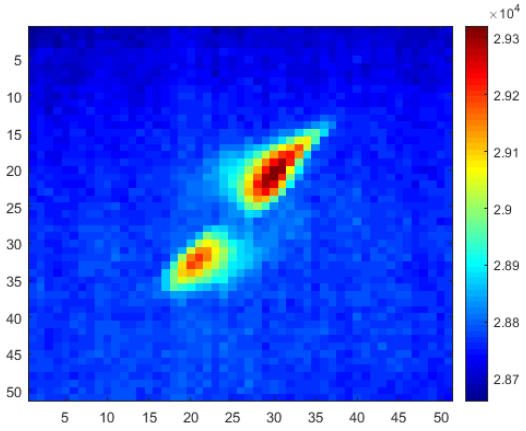

(b) MAT - 25J - 8th Frame

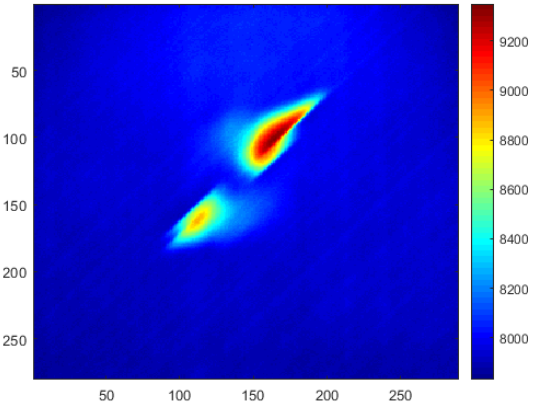

(e) SC7600 - 25J - 20th Frame

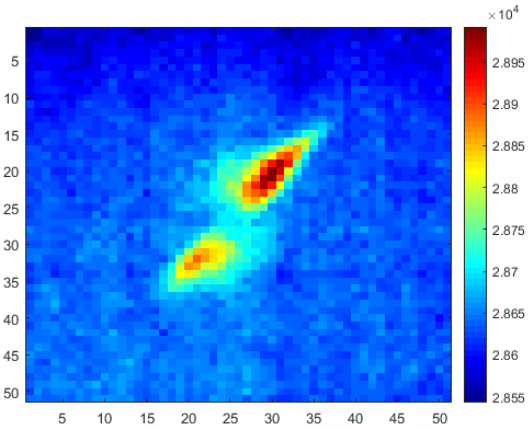

(c) MAT - 25J - 14th Frame

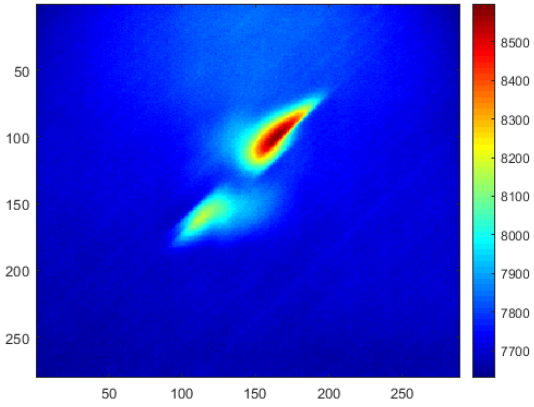

(f) SC7600 - 25J - 38th Frame

Figure 6-9 The raw thermal images at different times after the flash for the 25J sample.

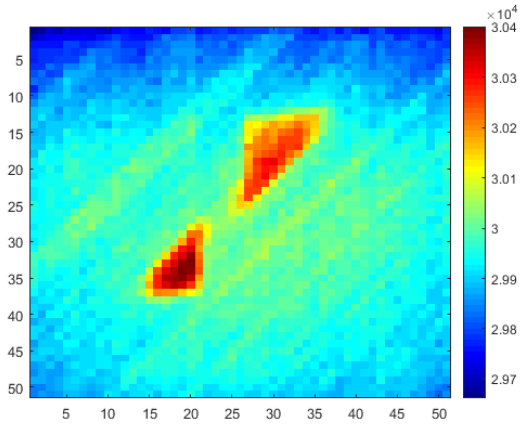

(a) MAT - 30J - 2nd Frame

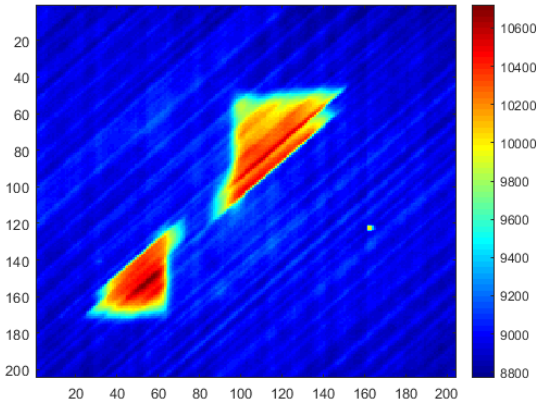

(d) SC7600 - 30J - 2nd Frame

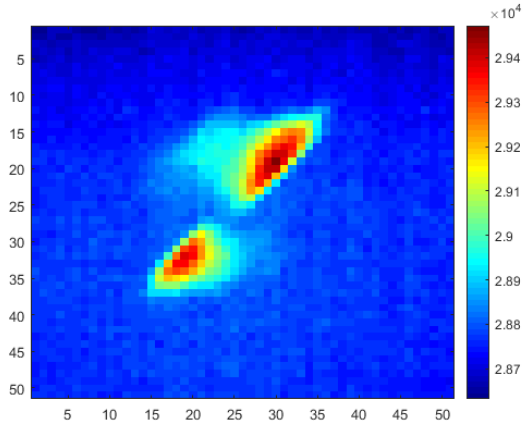

(b) MAT - 30J - 8th Frame

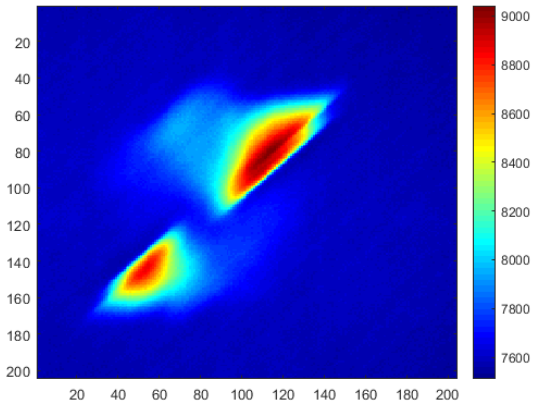

(e) SC7600 - 30J - 20th Frame

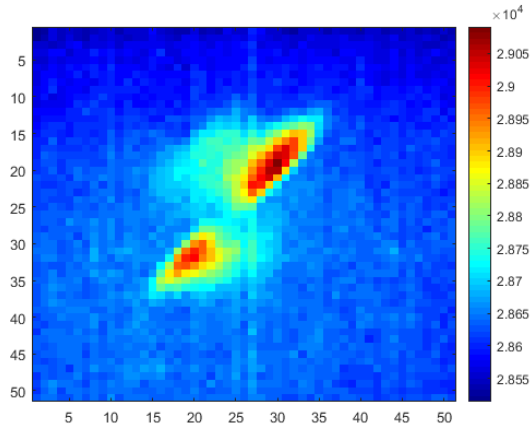

(c) MAT - 30J - 14th Frame

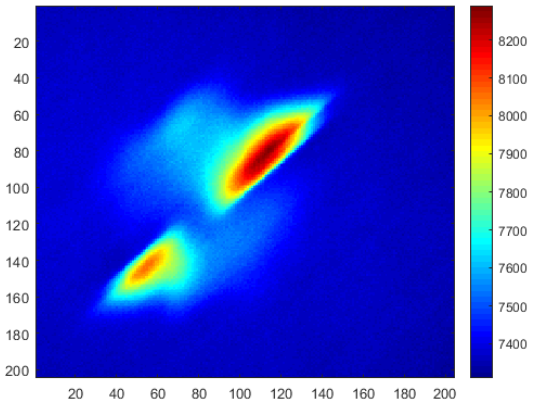

(f) SC7600 - 30J - 38th Frame

Figure 6-10 The raw thermal images at different times after the flash for the 30J sample.

transient heat change process by the MAT system. Moreover, considering the characteristics of high thermal conductivity & diffusivity of metal, and electromagnetic performance, if the metal sample can be heated continuously by eddy currents induced by electric currents in the coil produced from the induction heating, the detection performance can be improved.

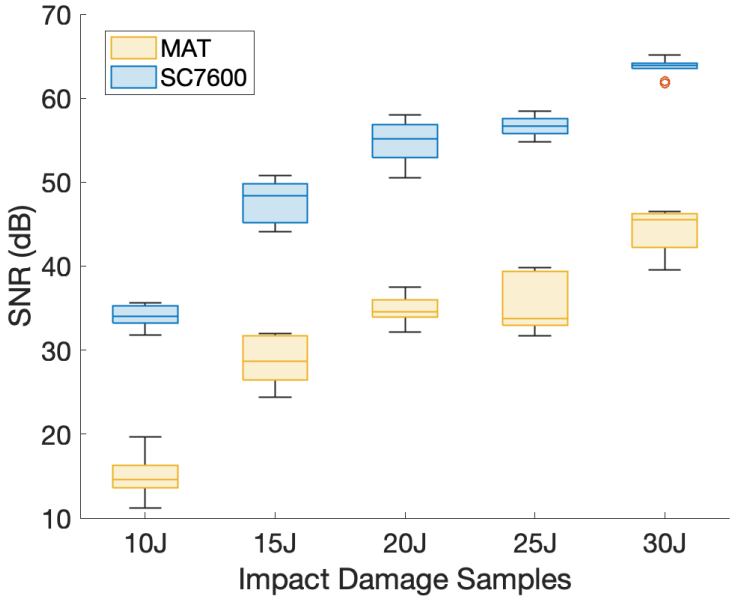

Figure 6-11 Comparison of SNR for MAT system and SC7600 for each impact energy damage.

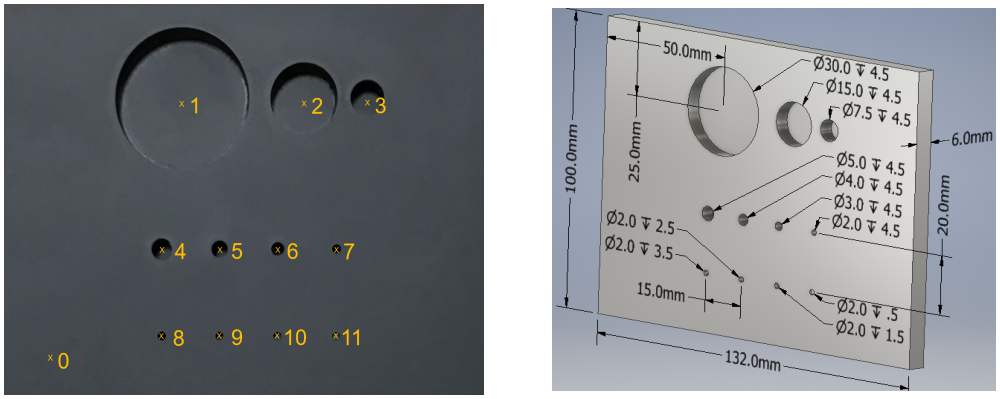

(a) Back side (b) 3D view

Figure 6-12 Illustration of Sample (steel). (a) A snapshot of the drilled side. Point 1-11 mark different defects and Point 0 is sampled from a sound region (reference region) (b) Dimensions of defects.

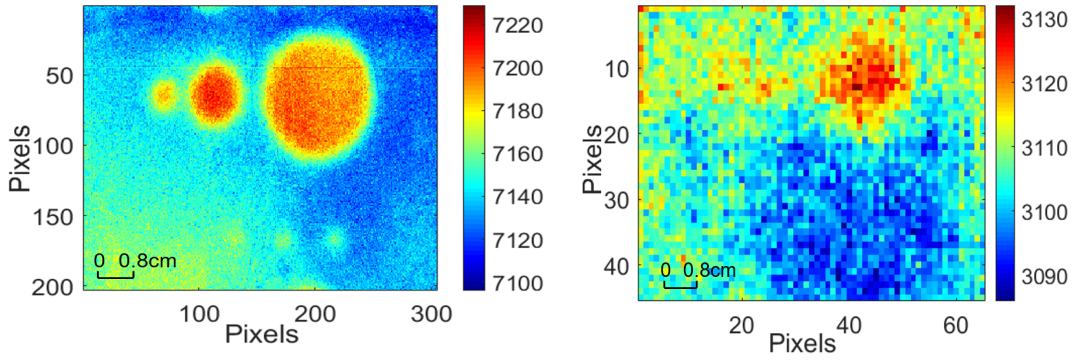

(a) SC7600---The No. 12th Frame (b) MAT---The No. 4th Frame

Figure 6-13 The raw thermal images at different times for Metal Sample.

6.5 Accessibility Test

To verify the accessibility of the MAT system, a representative use case such as a wing box will be simulated and tested. Figure 6-14(a) presents the process by 3D simulation. At the present stage, there is no condition to inspect the real wing box, so a model representing part of the wing box interior was made by a cardboard box, seen in Figure 6-14(b). Lightening holes are reserved for routine maintenance, and the placement of the two replacement samples indicates the part of the wing covering and the part of the internal skeleton respectively. As expected, the MAT system has accessibility and applicability to deploy for geometrically intricate systems and narrow space targets because of its small size and volume. It should be pointed out that the laser excitation source has not been integrated into the experiment because of its high energy and high safety requirements. The fibre laser, which has a small laser head and uses an optical fibre cable made of silica glass to guide light, will be tested and adjusted repeatedly in the lab's protective enclosure in the coming work. It will be introduced into the actual inspection environment under the condition of ensuring safety in the future.

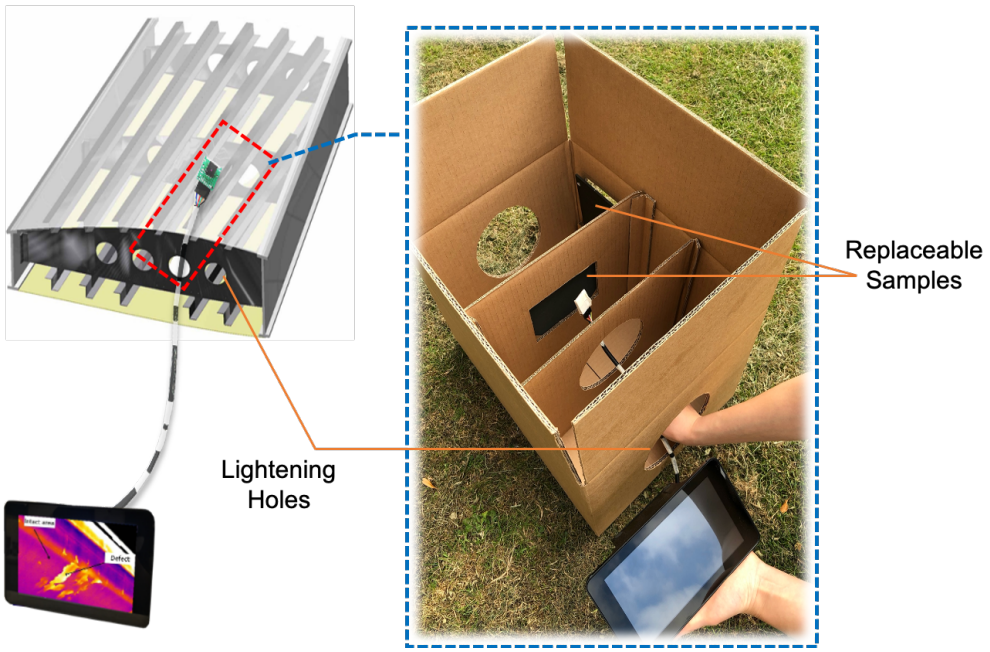

Figure 6-14 Accessibility test (a) 3D simulation for wing box inspection (b) Test physical prototype what simulate the part of wing box structure.

6.6 Summary

Aiming to validate the inspection performance and accessibility of the proposed MAT system, a few composite samples with impact damage and metal sample have been tested by the proposed system and high-end IR camera respectively. Meanwhile, an accessibility test is designed and conducted to evaluate the proposed system's performance to access geometrically intricate space. The results show that the proposed system can effectively detect impact damage in composites. It is observed that the crack length and delamination area increases with the impact energy. Due to the limitation of the SNR of the sensor, the display quality of the defect edge of the proposed system is slightly lower than that of the high-end camera. However, it does not affect the overall result judgment, except for a little blur located at the edge of the defect. For the metal sample, the low frame rate of the proposed system is not matching the high thermal conductivity

and high diffusivity of the material, so the MAT system is more appropriate for composite rather than metal. Through the accessibility test, it is proved that the MAT system has enhanced accessibility and applicability to deploy for geometrically intricate systems and narrow space targets. It also needs to be pointed out that the laser excitation source is not integrated for accessibility tests due to safety reasons at the present stage, and it will be introduced into actual scenes after safety assessment in future work.

7 CONCLUSIONS

This PhD project has developed a miniaturised active thermography (MAT) system for 'in-situ' inspection of complex industrial components, which contains low-cost, flexible, and configurable characteristics. This chapter presents the accomplishment of the targeted objectives, challenges, major findings, main contributions to knowledge, limitations of the proposed system, and recommendations for future work.

7.1 Contributions to Knowledge

This section describes the achievement and contributions of the research. The main contributions of this research can be summarised below:

(1). This research systematically identifies and analyses the current state-of-the-art of NDT miniaturisation techniques and discusses the challenges and prospects of miniaturisation of the commonly used NDT techniques. Found through literature review, the industrial endoscope is limited to detecting small surface defects and is not appropriate for sub-surface. The miniaturisation of Ultrasonic Testing is restricted by its coupling technology. The influence of radioactivity and its strict requirements on the detection environment restricts the miniaturisation of Radiation Testing. The miniaturised design of magnetic particle detection will reduce the lifting force and detection rate. Additionally, it is found that active thermography has a great prospect of miniaturisation for 'in-situ' inspection of complex components and systems. The flexibility with the selection of an excitation source and the choice of a small infrared sensor makes this work more attractive both scientifically and for industrial applications.

(2). This research proposed a novel miniaturised active thermography (MAT) system based on a commercial thermal imaging sensor featured with small size and low cost, where two optional excitation sources including flash and laser have been designed and integrated, to inspect and to evaluate defects of CFRP samples. According to the current sensor technology, FLIR Lepton

was identified as one of the smallest long-wavelength IR camera sensors in the market. RaspberryPi was selected to be the processor because its computing power matches with the lepton sensor which has low spatial resolution and frame rate. The results show that the proposed system can work effectively for the degradation assessment of composite laminates. Because of the compact size, lightweight and flexibility of the proposed MAT system, it can also integrate with a robot and Unmanned Aerial Vehicle (UAV) to inspect difficult-to-climb targets (e.g., wind turbine blades) and systems in hazardous condition (e.g., nuclear power generation).

(3). This research proposed a novel SRE4T system that allows improving the measurement accuracy of thermography inspection without upgrading sensors, based on the manual and automatic & controllable XY stage, to improve the spatial resolution of passive thermal images. In addition to thermal images, this technique can also be applied to other areas such as digital images. In other words, the technique can largely solve the inherent low resolution and low SNR problems of low-end sensors.

(4). This research proposed a novel data process, image processing, and feature extraction framework dedicated for the MAT system which features low-resolution and low SNR, to reduce the influence of noise and enhance the detectability of damage. Three carbon fibre reinforced polymer laminates with a variety of defects are evaluated quantitatively and qualitatively using the proposed system by comparing two existing non-miniaturised systems. Data pre-processing methods, such a TSR, Savitzky-Golay smoothing filter, and media filter are strongly recommended for MAT to reduce temporal and spatial noise before quantitative analysis. For the laser-based MAT system, the 1st and 2nd derivative TSR images show improved performance in representing the damage than the raw images. The 1st derivative image is more appropriate for damage with a large size while the 2nd derivative image is more appropriate for damage with a sharp boundary but with more noise. The methods can be applied to the vast majority of low-end IR sensors. It will greatly reduce the procurement cost of enterprises, expand the popularity of the use of IR sensors, and

contribute to the future development of the Structural Health Monitoring (SHM) field.

7.2 Research Findings

The overall conclusions of this research can be summarised below:

(1). The proposed MAT system can work with laser and flash effectively for degradation assessment although the detectability is compromised. Meanwhile, the data quality for the composite material seems to be more reliable and quantifiable than metal due to the relatively low sample rate of the sensor and the high thermal conductivity of the material (steel).

(2). The proposed MAT system has the most capability of the high-end system in terms of damage detection and depth measurement in CFRP laminates, although the detectability of defects against radius/depth ratio is compromised.

(3). The proposed Spatial Resolution Enhancement for a Thermogram (SRE4T) system can significantly improve the spatial resolution without upgrading the sensor, which through a high-resolution thermal image is reconstructed by fusing a sequence of low-resolution images with sub-pixel movements, up to 30.5% improvement of peak signal to noise ratio.

(4). The proposed MAT system introduces more noise than the high-end system. For the 16 flat-bottom holes CFRP sample, the average SNR is 10 dB lower than SC7600. Therefore, data pre-processing methods, such a TSR, Savitzky-Golay smoothing filter, and media filter are strongly recommended to reduce temporal and spatial noise before quantitative analysis.

(5). For the laser-based MAT system, the 1st and 2nd derivative TSR images show improved performance in representing the damage than the raw images. The 1st derivative image is more appropriate for damage with a large size while the 2nd derivative image is more appropriate for damage with a sharp boundary.

(6). Compared to the existing systems, the proposed system has a prominent price advantage and miniaturised volume. Its flexible body can better adapt to complex and geometrically intricate systems.

(7). The accessibility test proved that the MAT system has enhanced accessibility and applicability to deploy for geometrically intricate systems and narrow space targets.

7.3 Research Limitations and Future Work

Although the system has plenty of merits, some issues need to be further addressed. The research limitations and future work are shown below:

1. The proposed MAT system has a maximal sample rate of 10 fps, which limits its application to capture the thermal behaviour of materials with high thermal conductivity and diffusivity. At the present stage, choosing object materials with low thermal conductivity, such as CFRP and GFRP, will be the most effective method to overcome the existing problems. With the rapid development of sensor technology, the problem of low sample rate will be gradually solved, and the range of inspection targets will continue to expand. In addition, it has a prominent price advantage and a significantly small volume. Its small and flexible body could better adapt to complex and geometrically intricate space in the industrial in situ inspection in the future. It therefore will make a significant economic and social impact.
2. The second-generation SRE4T (Spatial Resolution Enhancement for a Thermogram) system significantly improves the spatial resolution without upgrading the sensor and also improves the measurement accuracy of thermography inspection. However, this technology has only been applied to passive thermography in this research, not active thermography. It can be applied to active thermal imaging in the future, but this requires further research to confirm its performance. In the future, sensor arrays will be considered to apply to the MAT system, improve and optimise the temporal responses.
3. The research has not worked with other thermal excitation sources, such as ultrasonic and microwave, which may also have the potential to work with

this sensor. In the future, more excitation sources will be explored considering different applications.

4. All the experiments and tests are based on the laboratory. It has not been used in real-world scenarios, such as the wing box or the aero-engine. In the future, the MAT system will be applied to more real inspection environments, and then it can be optimised and upgraded accordingly.

REFERENCES

[1] S. Addepalli, R. Roy, D. Axinte, and J. Mehnen, "'In-situ' Inspection Technologies: Trends in Degradation Assessment and Associated Technologies," *Procedia CIRP*, vol. 59, no. TESConf 2016, pp. 35–40, 2017, doi: 10.1016/j.procir.2016.10.003.

[2] S. K. Dwivedi, M. Vishwakarma, and P. A. Soni, "Advances and Researches on Non Destructive Testing: A Review," *Mater. Today Proc.*, vol. 5, no. 2, pp. 3690–3698, 2018, doi: 10.1016/j.matpr.2017.11.620.

[3] S. Perinpanayagam, D. Robb, D. J. Ewins, and J. M. Barragan, "Non-linearities in an aero-engine structure: From test to design," in *Proceedings of the 2004 International Conference on Noise and Vibration Engineering, ISMA*, 2004, no. Clv, pp. 3167–3181.

[4] I. Pioro and R. Duffey, "Current status of electricity generation in the world and future of nuclear power industry," in *Managing Global Warming*, T. M. B. T.-M. G. W. Letcher, Ed. Elsevier, 2019, pp. 67–114.

[5] L. Mishnaevsky, K. Branner, H. N. Petersen, J. Beauson, M. McGugan, and B. F. Sørensen, "Materials for wind turbine blades: An overview," *Materials (Basel).*, vol. 10, no. 11, pp. 1–24, 2017, doi: 10.3390/ma10111285.

[6] A. N. Ser'eznov, L. N. Stepanova, A. S. Laznenko, S. I. Kabanov, V. L. Kozhemyakin, and V. V. Chernova, "Static Tests of Wing Box of Composite Aircraft Wing Using Acoustic Emission and Strain Gaging," *Russ. J. Nondestruct. Test.*, vol. 56, no. 8, pp. 611–619, Aug. 2020, doi: 10.1134/S1061830920080094.

[7] Z. Chen, Z. Jiang, W. Gui, and C. Yang, "A Novel Device for Optical Imaging of Blast Furnace Burden Surface: Parallel Low-Light-Loss Backlight High-Temperature Industrial Endoscope," *IEEE Sens. J.*, vol. 16, no. 17, pp. 6703–6717, Sep. 2016, doi: 10.1109/JSEN.2016.2587729.

[8] Karl Storz, "Flexible Endoscopes Extremely flexible endoscopes." https://www.karlstorzndtec.com/fileadmin/user_upload/produkte/Produktd

atenblaetter/96191077_KSNDTec_PB3_Produktbrosch-E_15-01-2019.pdf.

[9] M. J. Lovejoy, *Magnetic Particle Inspection: A practical guide*. Springer Science & Business Media, 2012.

[10] Johnson & Allen, “Permanent Magnet.” https://www.johnsonandallen.co.uk/product/rpns.

[11] A. du Plessis, S. G. le Roux, and A. Guelpa, “The CT Scanner Facility at Stellenbosch University: An open access X-ray computed tomography laboratory,” *Nucl. Instruments Methods Phys. Res. Sect. B Beam Interact. with Mater. Atoms*, vol. 384, pp. 42–49, Oct. 2016, doi: 10.1016/j.nimb.2016.08.005.

[12] U. Ewert, “Current Developments in Digital Radiography and Computed Tomography from nm to Macro Scale,” in *12th European Conference on Non-Destructive Testing (ECNDT 2018).*, 2018, pp. 1–9.

[13] General Electric, “DXR250C-W/DXR250U-W Wireless Digital X-ray Detector.” https://www.gemeasurement.com/inspection-ndt/radiography-and-computed-tomography/dxr250c-wdxr250u-w-digital-detectors.

[14] F. Huan, L. Xiucheng, W. Bin, H. Qiang, and H. Cunfu, “Design of a miniaturised ultrasonic guided wave inspection instrument for steel strand flaw detection,” *Insight - Non-Destructive Test. Cond. Monit.*, vol. 59, no. 1, pp. 17–23, Jan. 2017, doi: 10.1784/insi.2017.59.1.17.

[15] Sonotron NDT, “ISONIC utPod.” http://www.sonotronndt.com/utpod.htm.

[16] W. Du, Y. Zhao, R. Roy, S. Addepalli, and L. Tinsley, “A review of miniaturised Non-Destructive Testing technologies for in-situ inspections,” *Procedia Manuf.*, vol. 16, no. November, pp. 16–23, 2018, doi: 10.1016/j.promfg.2018.10.152.

[17] D. Thapa, N. Samadi, A. Parkhimchyk, and N. Tabatabaei, “Comparison of low cost and research grade active thermography platforms for detection

of early dental caries," in *Optical Sensing and Detection VI*, Apr. 2020, no. May, p. 10, doi: 10.1117/12.2555279.

[18] Automation Technology, "C-CheckIR." https://www.automationtechnology.de/cms/en/mobile-ndt-systems-for-maintenance/.

[19] W. Du, H. Liu, A. Sirikham, S. Addepalli, and Y. Zhao, "A miniaturised active thermography system for in-situ inspections," 2020.

[20] I. Symposium *et al.*, "Development and demonstration of an automated system for limited access weld inspection by using infrared active thermography," pp. 1–8, 2015, [Online]. Available: http://urn.kb.se/resolve?urn=urn:nbn:se:hv:diva-9283.

[21] W. Du, H. Liu, A. Sirikham, S. Addepalli, and Y. Zhao, "A miniaturised active thermography system for in-situ inspections," *IFAC-PapersOnLine*, vol. 53, no. 3, pp. 66–71, 2020, doi: 10.1016/j.ifacol.2020.11.011.

[22] Y. Yu, Y. Yan, F. Wang, G. Tian, and D. Zhang, "An approach to reduce lift-off noise in pulsed eddy current nondestructive technology," *NDT E Int.*, vol. 63, pp. 1–6, Apr. 2014, doi: 10.1016/j.ndteint.2013.12.012.

[23] Á. Carrasco, F. Méndez, F. Leaman, and C. Molina Vicuña, "Short Review of the Use of Acoustic Emissions for Detection and Monitoring of Cracks," *Acoust. Aust.*, Feb. 2021, doi: 10.1007/s40857-021-00219-4.

[24] A. Hain, A. E. Zaghi, A. Kamali, R. P. Zaffetti, B. Overturf, and F. E. Pereira, "Applicability of 3-D Scanning Technology for Section Loss Assessment in Corroded Steel Beams," *Transp. Res. Rec. J. Transp. Res. Board*, vol. 2673, no. 3, pp. 271–280, Mar. 2019, doi: 10.1177/0361198119832887.

[25] T. Stratoudaki, M. Clark, and P. D. Wilcox, "Full matrix capture and the total focusing imaging algorithm using laser induced ultrasonic phased arrays," in *AIP Conference Proceedings*, 2017, vol. 1806, no. February 2017, p. 020022, doi: 10.1063/1.4974563.

[26] C. E. Betz, *Principles of magnetic particle testing*. Magnaflux Corp., 1967.

[27] K. Tout, A. Meguenani, J.-P. Urban, and C. Cudel, “Automated vision system for magnetic particle inspection of crankshafts using convolutional neural networks,” *Int. J. Adv. Manuf. Technol.*, vol. 112, no. 11–12, pp. 3307–3326, Feb. 2021, doi: 10.1007/s00170-020-06467-4.

[28] S. Liu, Y. Sun, M. Gu, C. Liu, L. He, and Y. Kang, “Review and analysis of three representative electromagnetic NDT methods,” *Insight-Non-Destructive Test. Cond. Monit.*, vol. 59, no. 4, pp. 176–183, 2017.

[29] Y. Sun, Y. Kang, and C. Qiu, “A new NDT method based on permanent magnetic field perturbation,” *NDT E Int.*, vol. 44, no. 1, pp. 1–7, Jan. 2011, doi: 10.1016/j.ndteint.2010.01.007.

[30] P. Hirsch, H. P. T. Hirsch, and P. Gmbh, “New Developed AC / DC-Pulse Technology for MT- Testing and Demagnetization of Steel Components,” vol. 1, pp. 1–8, 2016.

[31] R. Link, N. Riess, and U. R. Link, “Magnetic Particle Testing using Cross- and Additional Orthogonal Magnetic Coils- Application in Components of Large Dimensions,” pp. 1–8, 2016.

[32] T. Ito, A. Kasahara, and M. Hori, “Novel Demagnetization Method after Magnetic Particle Testing,” pp. 1–16.

[33] MAGNAFLUX, “AC/DC Electromagnetic Yoke.” https://magnaflux.com/Magnaflux/Products/Magnetic-Particle-Inspection/Equipment/Yokes/Y-7.htm.

[34] MAGNAFLUX, “Permanent Magnetic Yoke.” https://magnaflux.com/Magnaflux/Products/Magnetic-Particle-Inspection/Equipment/Yokes/YM-5.htm.

[35] L. Filipczyński, Z. Pawłowski, and J. Wehr, *Ultrasonic methods of testing materials*. Butterworths, 1966.

[36] Y. Aoyama, I. Takasu, and Y. Unigame, “Improvement in Efficiency of

Ultrasonic Tests for the Macroscopic Inclusions Evaluation," *J. ASTM Int.*, vol. 9, no. 4, pp. 1–7, 2012.

[37] S. Chaki and G. Bourse, "Guided ultrasonic waves for non-destructive monitoring of the stress levels in prestressed steel strands," *Ultrasonics*, vol. 49, no. 2, pp. 162–171, Feb. 2009, doi: 10.1016/j.ultras.2008.07.009.

[38] Y. Wang, X. Li, and B. Zheng, "Experimental study on mechanical properties of clay soil under compression by ultrasonic test," *Eur. J. Environ. Civ. Eng.*, vol. 22, no. 6, pp. 666–685, Jun. 2018, doi: 10.1080/19648189.2016.1217791.

[39] J. Blitz and G. Simpson, *Ultrasonic methods of non-destructive testing*, vol. 2. Springer Science & Business Media, 1995.

[40] Structural Diagnostics Inc, "Ultrasonic Testing." http://www.sdindt.com/Ultrasonic-Testing.html.

[41] F. Han, L. Zhang, and K. Cui, "Measuring Thickness of Object with Ultrasonic Thickness Gauge," in *MATEC Web of Conferences*, 2018, vol. 175, p. 3029.

[42] I. N. Ermolov, "Achievements in the theory of ultrasonic defectoscopy, its problems and prospects," *Defektoskopiya*, vol. 40, no. 10, pp. 13–48, 2004.

[43] Cygnus Instruments, "Ultrasonic Thickness Gauges," [Online]. Available: https://www.cygnus-instruments.com/en/product/cygnus-dive-underwater-gauge/.

[44] Sonatest, "UT & PA Flaw Detectors." https://sonatest.com/products/flaw-detectors/veo.

[45] OLYMPUS CORPORATION, "The EPOCH® 6LT Portable Flaw Detector." https://www.olympus-ims.com/en/epoch-6lt/.

[46] OLYMPUS CORPORATION, "Phased Array Wheel Probe." https://www.olympus-ims.com/en/rollerform/.

[47] Y. Zhan, C. Liu, J. Zhang, G. Mo, and C. Liu, "Measurement of residual

stress in laser additive manufacturing TC4 titanium alloy with the laser ultrasonic technique," *Mater. Sci. Eng. A*, vol. 762, no. June, p. 138093, Aug. 2019, doi: 10.1016/j.msea.2019.138093.

[48] S. K. Chakrapani, V. Dayal, and D. Barnard, "Detection and Characterization of Waviness in Unidirectional GFRP Using Rayleigh Wave Air Coupled Ultrasonic Testing (RAC-UT)," *Res. Nondestruct. Eval.*, vol. 24, no. 4, pp. 191–201, Oct. 2013, doi: 10.1080/09349847.2013.786158.

[49] M. Rutsch *et al.*, "Air-coupled ultrasonic bending plate transducer with piezoelectric and electrostatic transduction element combination," *IEEE Int. Ultrason. Symp. IUS*, vol. 2019-Octob, pp. 147–150, 2019, doi: 10.1109/ULTSYM.2019.8925701.

[50] Y. Zhang, S. Huang, W. Zhao, S. Wang, and Q. Wang, "Electromagnetic ultrasonic guided wave long-term monitoring and data difference adaptive extraction method for buried oil-gas pipelines," *Int. J. Appl. Electromagn. Mech.*, vol. 54, no. 3, pp. 329–339, 2017.

[51] K. K. Junjie CHANG1, 2, Chao LU1, "Development of Non-Contact Air Coupled Ultrasonic Testing System for Reinforced concrete Structure," in *2013 Far East Forum on Nondestructive Evaluation/Testing: New Technology and Application*, no. 2, pp. 3–4.

[52] N. Boaretto and T. M. Centeno, "Automated detection of welding defects in pipelines from radiographic images DWDI," *NDT E Int.*, vol. 86, no. November 2016, pp. 7–13, Mar. 2017, doi: 10.1016/j.ndteint.2016.11.003.

[53] R. R. da S. & D. Mery, "The state of the Art of Weld Seam Radiographic Testing," *Mater. Eval.*, pp. 643–647, 2007.

[54] Kalkars NDT Services, "Radiographic Testing." http://www.ndt.kalkars.com/radiographic-testing-training.

[55] G. S. Risti, "THE DIGITAL FLAT-PANEL X-RAY DETECTORS."

[56] MITECH, "XXQ-2505 Portable X-ray Flaw Detector."

http://www.rstar.com/manufacturer-28211-ndt-x-ray-flaw-detector.

[57] General Electric, “industrial CT Scanner for fully automated industrial Computed Tomography.” https://www.gemeasurement.com/inspection-ndt/radiography-and-computed-tomography/phoenix-vtomex-m.

[58] X. P. V Maldague, “Introduction to NDT by active infrared thermography,” *Mater. Eval.*, vol. 60, no. 9, pp. 1060–1073, 2002, [Online]. Available: http://w3.gel.ulaval.ca/~maldagx/r_1221t.pdf.

[59] C. Ibarra-Castanedo, A. Bendada, and X. P. V. Maldague, “Thermographic Image Processing for NDT,” *IV Conf. Panam. END*, pp. 1–12, 2007.

[60] S. Shepard, “Flash thermography of aerospace composites,” *IV Conf. Panam. END Buenos Aires*, p. 7, 2007, doi: 10.1016/j.compositesa.2011.01.007.

[61] Y. Zhao, L. Tinsley, S. Addepalli, J. Mehnen, and R. Roy, “A coefficient clustering analysis for damage assessment of composites based on pulsed thermographic inspection,” *NDT E Int.*, vol. 83, pp. 59–67, 2016, doi: 10.1016/j.ndteint.2016.06.003.

[62] T. Widjanarko, L. Tinsley, R. Roy, and J. Mehnen, “Characterisation and performance assessment of a pulsed-thermography camera system for component degradation inspection,” in *proceedings of the 1st International Conference on Through-life Engineering Services, Cranfield*, 2012, pp. 297–308.

[63] S. Sfarra, C. Ibarra-Castanedo, F. Lambiase, D. Paoletti, A. Di Ilio, and X. Maldague, “From the experimental simulation to integrated non-destructive analysis by means of optical and infrared techniques: results compared,” *Meas. Sci. Technol.*, vol. 23, no. 11, p. 115601, Nov. 2012, doi: 10.1088/0957-0233/23/11/115601.

[64] S. Guibert, A. Bendada, and X. P. V Maldague, “Active Infrared thermography techniques for the non-destructive testing of materials,” *Ultrason. Adv. Methods Nondestruct. Test. Mater. Charact.*, pp. 325–348,

2007.

[65] X. P. V. Maldague, T. S. Jones, H. Kaplan, S. Marinetti, and M. And Prystay, *Fundamentals of Infrared and Thermal Testing*, 3rd ed. Ohio: ASNT, 2001.

[66] C. Ibarra-Castanedo *et al.*, “Comparative Study of Active Thermography Techniques for the Nondestructive Evaluation of Honeycomb Structures,” *Res. Nondestruct. Eval.*, vol. 20, no. 1, pp. 1–31, Jan. 2009, doi: 10.1080/09349840802366617.

[67] X. Lu *et al.*, “Pulsed Air-Flow Thermography for Natural Crack Detection and Evaluation,” vol. 20, no. 14, pp. 8091–8097, 2020.

[68] L. Lei, G. Ferrarini, A. Bortolin, G. Cadelano, P. Bison, and X. Maldague, “Thermography is cool: Defect detection using liquid nitrogen as a stimulus,” *NDT E Int.*, vol. 102, no. May 2018, pp. 137–143, Mar. 2019, doi: 10.1016/j.ndteint.2018.11.012.

[69] X. Zhang *et al.*, “CFRP Impact Damage Inspection Based on Manifold Learning Using Ultrasonic Induced Thermography,” *IEEE Trans. Ind. Informatics*, vol. 15, no. 5, pp. 2648–2659, May 2019, doi: 10.1109/TII.2018.2866413.

[70] B. Gao, L. Bai, W. L. Woo, G. Y. Tian, and Y. Cheng, “Automatic Defect Identification of Eddy Current Pulsed Thermography Using Single Channel Blind Source Separation,” *IEEE Trans. Instrum. Meas.*, vol. 63, no. 4, pp. 913–922, Apr. 2014, doi: 10.1109/TIM.2013.2285789.

[71] G. Steenackers, J. Peeters, S. Verspeek, and B. Ribbens, “From Thermal Inspection to Updating a Numerical Model of a Race Bicycle: Comparison with Structural Dynamics Approach,” *Appl. Sci.*, vol. 8, no. 2, p. 307, Feb. 2018, doi: 10.3390/app8020307.

[72] D. P. Almond, S. L. Angioni, and S. G. Pickering, “Long pulse excitation thermographic non-destructive evaluation,” *NDT E Int.*, vol. 87, no. July 2016, pp. 7–14, Apr. 2017, doi: 10.1016/j.ndteint.2017.01.003.

[73] Z. Wang, G. Tian, M. Meo, and F. Ciampa, “Image processing based quantitative damage evaluation in composites with long pulse thermography,” *NDT E Int.*, vol. 99, no. July, pp. 93–104, Oct. 2018, doi: 10.1016/j.ndteint.2018.07.004.

[74] H. A. Thajeel, “Numerical modeling of infrared thermography techniques via ANSYS,” *Missouri Univ. Sci. Technol.*, 2013.

[75] C. Ibarra-Castanedo *et al.*, “Comparative Study of Active Thermography Techniques for the Nondestructive Evaluation of Honeycomb Structures,” *Res. Nondestruct. Eval.*, vol. 20, no. 1, pp. 1–31, Jan. 2009, doi: 10.1080/09349840802366617.

[76] B. Liu, H. Zhang, H. Fernandes, and X. Maldague, “Experimental Evaluation of Pulsed Thermography, Lock-in Thermography and Vibrothermography on Foreign Object Defect (FOD) in CFRP,” *Sensors*, vol. 16, no. 5, p. 743, May 2016, doi: 10.3390/s16050743.

[77] C. Ibarra-Castanedo, N. P. Avdelidis, M. Grenier, X. Maldague, and A. Bendada, “Active thermography signal processing techniques for defect detection and characterization on composite materials,” in *Thermosense XXXII*, Apr. 2010, vol. 7661, p. 76610O, doi: 10.1117/12.850733.

[78] M. H. Wong and K. H. H. Goh, “Infrared Thermography of Complex 3D Printed Components,” no. October 2018, Oct. 2018, [Online]. Available: http://arxiv.org/abs/1810.05413.

[79] A. Dillenz, T. Zweschper, and G. Busse, “Progress in ultrasound phase thermography,” in *Proc.SPIE*, Mar. 2001, vol. 4360, pp. 574–579, doi: 10.1117/12.421042.

[80] L. D. Favro, X. Han, Z. Ouyang, G. Sun, H. Sui, and R. L. Thomas, “Infrared imaging of defects heated by a sonic pulse,” *Rev. Sci. Instrum.*, vol. 71, no. 6, pp. 2418–2421, Jun. 2000, doi: 10.1063/1.1150630.

[81] L. Pieczonka, F. Aymerich, and W. J. Staszewski, “Impact Damage Detection in Light Composite Sandwich Panels,” *Procedia Eng.*, vol. 88, no.

December, pp. 216–221, 2014, doi: 10.1016/j.proeng.2014.11.147.

[82] Y. He, G. Tian, M. Pan, and D. Chen, “Eddy current pulsed phase thermography and feature extraction,” *Appl. Phys. Lett.*, vol. 103, no. 8, p. 084104, Aug. 2013, doi: 10.1063/1.4819475.

[83] U. Netzelmann and G. Walle, “Induction thermography as a tool for reliable detection of surface defects in forged components,” *17th WCorld Conf. NDT, Shanghai, China*, no. October 2008, p. 8, 2008, [Online]. Available: http://www.ndt.net/article/wcndt2008/papers/337.pdf.

[84] J. Wilson, G. Tian, I. Mukriz, and D. Almond, “PEC thermography for imaging multiple cracks from rolling contact fatigue,” *NDT E Int.*, vol. 44, no. 6, pp. 505–512, Oct. 2011, doi: 10.1016/j.ndteint.2011.05.004.

[85] X. Maldague, “Theory and practice of infrared technology for nondestructive testing,” 2001.

[86] H. I. Ringermacher, R. J. Archacki Jr, and W. A. Veronesi, “Nondestructive testing: Transient depth thermography.” US Patents, Jan. 27, 1998.

[87] Z. Zeng, J. Zhou, N. Tao, L. Feng, and C. Zhang, “Absolute peak slope time based thickness measurement using pulsed thermography,” *Infrared Phys. Technol.*, vol. 55, no. 2–3, pp. 200–204, 2012.

[88] D. P. Almond and S. K. Lau, “Defect sizing by transient thermography. I. An analytical treatment,” *J. Phys. D. Appl. Phys.*, vol. 27, no. 5, p. 1063, 1994.

[89] S. M. Shepard, “Reconstruction and enhancement of active thermographic image sequences,” *Opt. Eng.*, vol. 42, no. 5, p. 1337, May 2003, doi: 10.1117/1.1566969.

[90] S. M. Shepard, “Temporal noise reduction, compression and analysis of thermographic image data sequences.” US Patents, Feb. 04, 2003.

[91] J. G. Sun, “Analysis of Pulsed Thermography Methods for Defect Depth Prediction,” *J. Heat Transfer*, vol. 128, no. 4, pp. 329–338, Apr. 2006, doi:

10.1115/1.2165211.

[92] J. G. Sun, “Method for Determining Defect Depth using Thermal Imaging,” vol. 2, no. 12, Art. no. US6542849B2, 2003.

[93] A. Sirikham, Y. Zhao, and J. Mehnen, “Determination of thermal wave reflection coefficient to better estimate defect depth using pulsed thermography,” *Infrared Phys. Technol.*, vol. 86, pp. 1–10, Nov. 2017, doi: 10.1016/j.infrared.2017.08.012.

[94] A. Savitzky and M. J. E. Golay, “Smoothing and Differentiation of Data by Simplified Least Squares Procedures.,” *Anal. Chem.*, vol. 36, no. 8, pp. 1627–1639, Jul. 1964, doi: 10.1021/ac60214a047.

[95] Therm-App, “Therm-App TH.” https://therm-app.com/therm-app-thermography/.

[96] FLIR, “FLIR ONE.” http://www.flir.co.uk/flirone/ (accessed May 28, 2018).

[97] SEEK Thermal, “Seek Thermal Compact.” https://www.thermal.com/compact-series.html.

[98] FLIR, “LEPTON 3.” http://www.flir.co.uk/cores/lepton/.

[99] S. Addepalli, R. Roy, D. Axinte, and J. Mehnen, “‘In-situ’ Inspection Technologies: Trends in Degradation Assessment and Associated Technologies,” *Procedia CIRP*, vol. 59, no. TESConf 2016, pp. 35–40, 2017, doi: 10.1016/j.procir.2016.10.003.

[100] T. Li, D. P. Almond, and D. A. S. Rees, “Crack imaging by scanning pulsed laser spot thermography,” *NDT E Int.*, vol. 44, no. 2, pp. 216–225, 2011, doi: 10.1016/j.ndteint.2010.08.006.

[101] P. Broberg, “Surface crack detection in welds using thermography,” *NDT E Int.*, vol. 57, pp. 69–73, 2013, doi: 10.1016/j.ndteint.2013.03.008.

[102] A. Sirikham, Y. Zhao, H. Y. Nezhad, W. Du, and R. Roy, “Estimation of Damage Thickness in Fiber-Reinforced Composites using Pulsed Thermography,” *IEEE Trans. Ind. Informatics*, vol. 15, no. 1, pp. 445–453,

Jan. 2019, doi: 10.1109/TII.2018.2878758.

[103] J. Zhu, G. Tiany, Q. Min, and J. Wu, “Comparison Study of Different Features for Pocket Length Quantification of Angular Defects Using Eddy Current Pulsed Thermography,” *IEEE Trans. Instrum. Meas.*, vol. 68, no. 5, pp. 1373–1381, May 2019, doi: 10.1109/TIM.2018.2890053.

[104] A. Redjimi, D. Knežević, K. Savić, N. Jovanović, M. Simović, and D. Vasiljević, “Noise Equivalent Temperature Difference Model for Thermal Imagers, Calculation and Analysis,” *Sci. Tech. Rev.*, vol. 64, no. 2, pp. 14–19, 2014.

[105] Infratec, “New Infrared camera ImageIR ® 9300 Series.” https://www.infratec.co.uk/thermography/infrared-camera/imageir-9300/.

[106] H. Zhang, R. Yang, Y. He, A. Foudazi, L. Cheng, and G. Tian, “A Review of Microwave Thermography Nondestructive Testing and Evaluation,” *Sensors*, vol. 17, no. 5, p. 1123, May 2017, doi: 10.3390/s17051123.

[107] G. Gaussorgues and S. Chomet, *Infrared thermography*, vol. 5. Springer Science & Business Media, 1993.

[108] M. Mancuso and S. Battiato, “An introduction to the digital still camera technology,” *ST J. Syst. Res.*, vol. 2, no. 2, pp. 1–9, 2001.

[109] P. J. Withagen, F. C. A. Groen, and K. Schutte, “CCD Color Camera Characterization for Image Measurements,” *IEEE Trans. Instrum. Meas.*, vol. 56, no. 1, pp. 199–203, Feb. 2007, doi: 10.1109/TIM.2006.887667.

[110] W. E. Erkonen, “Basic principles of non-contact temperature measurement,” *Radiol. 101 Basics Fundam. Imaging*, pp. 3–7, 1998.

[111] S. D. Holland and J. Renshaw, “Physics-based image enhancement for infrared thermography,” *NDT E Int.*, vol. 43, no. 5, pp. 440–445, Jul. 2010, doi: 10.1016/j.ndteint.2010.04.004.

[112] H. I. Ashiba, H. M. Mansour, M. F. El-Kordy, and H. M. Ahmed, “A New Approach for Contrast Enhancement of Infrared Images Based on Contrast

Limited Adaptive Histogram Equalization," *Appl. Math. Inf. Sci. Lett. An Int. J. Appl. Math. Inf. Sci. Lett*, vol. 3, no. 3, pp. 123–125, 2015, doi: 10.12785/amisl/030306.

[113] M. S. Alam, J. G. Bognar, R. C. Hardie, and B. J. Yasuda, "Infrared image registration and high-resolution reconstruction using multiple translationally shifted aliased video frames," *IEEE Trans. Instrum. Meas.*, vol. 49, no. 5, pp. 915–923, 2000, doi: 10.1109/19.872908.

[114] FLIR, "Flir UltraMax." https://www.flir.com/discover/rd-science/ultramax--the-ultimate-resolution/.

[115] J. Sadi and A. Crastes, "High resolution images obtained with uncooled microbolometer," in *Proceedings of SPIE*, Apr. 2008, p. 694106, doi: 10.1117/12.782783.

[116] M. Kaczmarek and M. Borwanski, "Resolution enhancement of thermal images in active dynamic thermography sequences," in *Proceedings of the 2012 International Conference on Quantitative InfraRed Thermography*, 2012, no. September, doi: 10.21611/qirt.2012.274.

[117] C. S. G. Gerald Mwangi, Paul Fieguth, "Thermography Spatial Resolution Enhancement By Non-Rigid Registration With Visible Imagery," *Image Process. (ICIP), 2015 Int. Conf. IEEE*, pp. 2542–2546, 2015.

[118] D. Keren, S. Peleg, and R. Brada, "Image sequence enhancement using sub-pixel displacements," in *Proceedings CVPR '88: The Computer Society Conference on Computer Vision and Pattern Recognition*, 1988, no. 3, pp. 742–746, doi: 10.1109/CVPR.1988.196317.

[119] T. Q. Pham, L. J. van Vliet, and K. Schutte, "Robust Fusion of Irregularly Sampled Data Using Adaptive Normalized Convolution," *EURASIP J. Adv. Signal Process.*, vol. 2006, no. 1, p. 083268, Dec. 2006, doi: 10.1155/ASP/2006/83268.

[120] H. Knutsson and C.-F. Westin, "Normalized and differential convolution," in *Proceedings of IEEE Conference on Computer Vision and Pattern*

Recognition, Jan. 1995, vol. 22, no. 1, pp. 515–523, doi: 10.1109/CVPR.1993.341081.

[121] S. Azam, F. Tuz Zohra, and M. M. Islam, “A State-of-the-art Review on Wavelet Based Image Resolution Enhancement Techniques: Performance Evaluation Criteria and Issues,” *Int. J. Image, Graph. Signal Process.*, vol. 6, no. 9, pp. 35–46, Aug. 2014, doi: 10.5815/ijigsp.2014.09.05.

[122] Z. Wang, A. C. Bovik, H. R. Sheikh, and E. P. Simoncelli, “Image Quality Assessment: From Error Visibility to Structural Similarity,” *IEEE Trans. Image Process.*, vol. 13, no. 4, pp. 600–612, Apr. 2004, doi: 10.1109/TIP.2003.819861.

[123] A. Mittal, R. Soundararajan, and A. C. Bovik, “Making a ‘Completely Blind’ Image Quality Analyzer,” *IEEE Signal Process. Lett.*, vol. 20, no. 3, pp. 209–212, Mar. 2013, doi: 10.1109/LSP.2012.2227726.

[124] D. Y. Tsai, Y. Lee, and E. Matsuyama, “Information entropy measure for evaluation of image quality,” *J. Digit. Imaging*, vol. 21, no. 3, pp. 338–347, 2008, doi: 10.1007/s10278-007-9044-5.

[125] C. Pei, H. Liu, J. Qiu, T. Liu, and Z. Chen, “Progress on the ultrasonic testing and laser thermography techniques for NDT of tokamak plasma-facing components,” *Theor. Appl. Mech. Lett.*, vol. 9, no. 3, pp. 180–187, May 2019, doi: 10.1016/j.taml.2019.03.011.

[126] A. Sophian, G. Y. Tian, D. Taylor, and J. Rudlin, “Electromagnetic and eddy current NDT: A review,” *Insight Non-Destructive Test. Cond. Monit.*, vol. 43, no. 5, pp. 302–306, 2001.

[127] S. K. Lau, D. P. Almond, and J. M. Milne, “A quantitative analysis of pulsed video thermography,” *NDT E Int.*, vol. 24, no. 4, pp. 195–202, 1991, doi: 10.1016/0963-8695(91)90267-7.

[128] D. L. Balageas, J.-M. Roche, F.-H. Leroy, W.-M. Liu, and A. M. Gorbach, “The thermographic signal reconstruction method: A powerful tool for the enhancement of transient thermographic images,” *Biocybern. Biomed.*

Eng., vol. 35, no. 1, pp. 1–9, 2015, doi: 10.1016/j.bbe.2014.07.002.

[129] Y. Zhao, S. Addepalli, A. Sirikham, and R. Roy, “A confidence map based damage assessment approach using pulsed thermographic inspection,” *NDT E Int.*, vol. 93, no. September 2017, pp. 86–97, Jan. 2018, doi: 10.1016/j.ndteint.2017.10.001.

[130] B. Wang, S. Zhong, T.-L. Lee, K. S. Fancey, and J. Mi, “Non-destructive testing and evaluation of composite materials/structures: A state-of-the-art review,” *Adv. Mech. Eng.*, vol. 12, no. 4, pp. 1–28, Apr. 2020, doi: 10.1177/1687814020913761.

[131] M. F. Beemer and S. M. Shepard, “Aspect ratio considerations for flat bottom hole defects in active thermography,” *Quant. Infrared Thermogr. J.*, vol. 15, no. 1, pp. 1–16, Jan. 2018, doi: 10.1080/17686733.2017.1328642.

[132] G. Silipigni *et al.*, “Optimization of the pulse-compression technique applied to the infrared thermography nondestructive evaluation,” *NDT E Int.*, vol. 87, no. August 2016, pp. 100–110, 2017, doi: 10.1016/j.ndteint.2017.01.011.

[133] X. C. Sun and S. R. Hallett, “Barely visible impact damage in scaled composite laminates: Experiments and numerical simulations,” *Int. J. Impact Eng.*, vol. 109, pp. 178–195, Nov. 2017, doi: 10.1016/j.ijimpeng.2017.06.008.